ABSTRACT

The hydrophilization of polydimethylsiloxane (PDMS) using poly(vinyl alcohol) (PVOH) thin films has been studied to utilize hydrophilic materials in PDMS-based micro- and nanomanufactured devices more effectively. Previous studies have determined that PVOH spontaneously adsorbs from aqueous solution onto hydrophobic substrates due to the hydrophobic effect. Following spontaneous adsorption, PVOH thin films are stabilized via crystallization driven by hydrogen bonding.

PVOH thin films can also be prepared via adsorptive spin coating on flat substrates. We have found that the PVOH-PDMS system varies from the well-established Meyerhofer model, which predicts film thickness from spin rate, solution viscosity (polymer concentration), and other variables. We proposed a new model to describe film thickness (h) from spin coating, which includes polymer-substrate interactions (spontaneous adsorption) and polymer-polymer interactions (e.g., crystallization and the hydrophobic effect). We hypothesized that these two types of interactions form the h_1 and h_2 thicknesses of the multilayered spin-coated PVOH-PDMS thin films. However, recent evidence has shown that the structure of polymer thin films is even more complex and nuanced.

In this study, we continue to elucidate the complex structure and dynamics of PVOH-PDMS thin films via static adsorption, adsorptive spin coating, and water annealing experiments. We use PDMS polymers of various molecular weights (MWs) ($PDMS^{340}$, MW = 340 Da; $PDMS^{2k}$, MW = 2 kDa; $PDMS^{9k}$, MW = 9.430 kDa; $PDMS^{49k}$, MW = 49.350 kDa) since the PDMS polymers vary in hydrophobicity and mobility. We also study two different PVOH polymers ($PVOH^{88\%H}$, MW = 85-124 kDa, 87-89% hydrolyzed; $PVOH^{99\%H}$, MW = 89-98 kDa, 99+% hydrolyzed) since the PVOH polymers vary in hydrophobicity and crystallinity. We vary the time before water annealing (0 h vs. 24 h) to determine the stability of partially dry vs. completely dry films. We characterize film thickness, wettability, and morphology to identify changes in the PVOH thin film layers.

We can separate the spontaneously-adsorbed h_1 layer into sublayers: a tightly-bound h_1 layer and a loosely-bound h_1 layer. The tightly-bound h_1 layer is first formed when PVOH adsorbs onto the PDMS substrate and is resistant to desorption in water. We found evidence of this layer on almost all of the PVOH-PDMS systems in this study. The only exception was the $PVOH^{99\%H}$-$PDMS^{340}$ system, in which the hydrophobicity of the substrate and the polymer were insufficient to drive spontaneous adsorption. The loosely-bound h_1 layer is formed on top of the tightly-bound h_1 layer and is desorbed during water annealing. We found evidence of this layer on $PDMS^{9k}$ substrates alone. While a hydrophobic substrate is generally sufficient to form a tightly-bound PVOH h_1 layer, it is insufficient at forming a loosely-bound h_1 layer.

AN INVESTIGATION OF THE STABILITY AND STRUCTURE OF POLY(VINYL ALCOHOL) THIN FILMS ON POLYDIMETHYLSILOXANE

Julia Griffin

A thesis presented to the faculty of Mount Holyoke College in partial fulfillment of the requirements for the degree of Bachelor of Arts with Honors

Department of Chemistry

South Hadley, Massachusetts

May 2023

This thesis was prepared under the direction of Dr. Wei Chen

for 8 credits of independent study

ACKNOWLEDGMENTS

I am beyond grateful to so many people who have aided me in this project and throughout my college years. When I first started college, I could not have envisioned this being my present reality: being a part of such a wonderful, welcoming, intellectually-curious research group, contributing to Professor Chen's research, and joining a strong network of Mount Holyoke alums who continue to pursue knowledge and uplift others after their time here.

I first want to express my gratitude to Professor Wei Chen for her consistent mentorship, her passion for teaching, and her vast depth of knowledge that she willingly shares with her students. I am grateful that she invited me to join her lab and has kept pushing me to take on new challenges.

I am grateful to Dr. Himali Jayathilake for her insightful feedback on my projects and presentations over the years, her support, and her kindness. Her searing questions have shown me how to identify areas in need of improvement in order to conduct more robust research.

I want to thank Professor Amy Camp for serving on my thesis committee. I truly appreciate her willingness to give her time and feedback on my thesis.

I also want to acknowledge my mentor, Echo Jiang, for sharing her patience and knowledge with me during her last year at Mount Holyoke College. I can now grasp the enormity of doing graduate school applications, in-person research, thesis writing, and mentoring all at once. I am so grateful for her dedication to training me in the midst of the COVID-19 pandemic and all of her aforementioned responsibilities.

To my former and current lab mates–Echo Jiang, Maggie Minett, Katie Kolozsvari, Anya Chinniah, Carlie Poworoznek, Nancy Jiang, Carolina Alvarez, Eliza Butler, Isabel Xu, Mackenzie Windus, Sophie Lee, Mamie Mulder, Gracie Wilkinson, and Wenqi Tsou–thank you for pushing me to be a better researcher and a better person. I am especially grateful to Nancy for conducting some of these experiments with me, and to Sophie for optimizing, documenting, and sharing the updated fractal analysis protocol with the group.

To my parents, partner, and friends: thank you so much for your support–I am grateful for your feedback and encouragement.

TABLE OF CONTENTS

LIST OF FIGURES AND TABLES

I. INTRODUCTION

1.1 Polymer thin film overview

Thin films (films with thicknesses of 100 nm or less) are employed to modify the surface properties of objects without altering their bulk properties. They are ubiquitous in electronics, adhesives, lubricants, paints, optical and dielectric coatings, and other applications.[1] Thin films allow us to design materials with specific properties that do not exist naturally in the bulk materials, and thus expand their possible applications. Thin films also enable green chemistry practices since the material required to form a thin film is significantly less than the mass of a bulk object.

Polymer thin film structure and properties can vary significantly from the bulk polymer's structure and properties as a result of the film thickness approaching molecular dimensions.[2-6] For example, the glass transition temperature tends to change[7] and the Debye-Waller factor, which describes thermal motion, tends to decrease.[8-9] These and other changes in material properties result in thin film stability and dynamics that vary from the bulk.

Thin films can be continuous or discontinuous, and either type of film can be beneficial, depending on the intended application. Extensive literature has been published on the use of continuous polymer thin films to manufacture flexible solar cells that can be integrated in everyday items, such as clothing and building materials.[10-13] On the other hand, discontinuous polymer thin films are used to pattern surfaces in studies of cell responses,[14] protein and nucleic acid structure and activity,[15] and regenerative medicine.[16] Controlled patterning of polymer films is also instrumental in high-density data storage[17] and microcontact printing.[18-19]

1.2 Stability of polymer thin films

1.2.1 Film stability regimes

Thin films can be categorized as stable, metastable, or unstable, according to whether or not they are continuous and the conditions under which they are continuous or discontinuous.[20] The three thin film stability regimes are represented on an effective interface potential vs. film thickness graph shown in Figure 1. The effective interface potential is the excess free energy required to bring two interfaces together to a certain distance (thickness) from an infinite distance. The effective interface potential as a function of the initial film thickness is represented as $\phi(h)$. In Figure 1, curve 1 corresponds to a stable scenario, curve 2 corresponds to an unstable scenario, and curve 3 corresponds to an metastable scenario. Curve 1 represents a stable scenario since the global minimum occurs at infinity, meaning film thinning is not energetically favorable. Curve 2 is unstable since the global minimum occurs at a finite value of h. Curve 3 corresponds to a metastable scenario, where the films are stable when the initial thickness is greater than that at the local maximum, and unstable when the initial thickness is less than that at the local maximum.

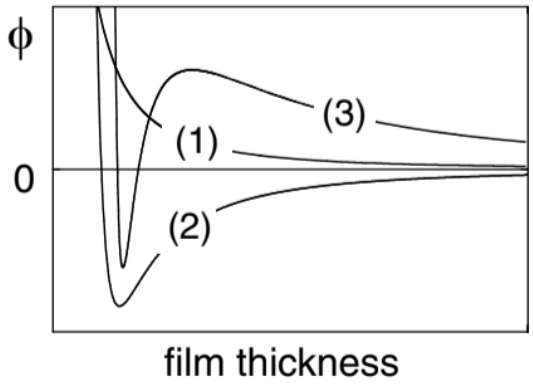

Figure 1. Effective interface potential ϕ vs. film thickness h.[20]

1.2.2 Dewetting mechanisms

Unstable and metastable films are prone to dewetting, a spontaneous phenomenon during which holes form in thin films. Three main dewetting mechanisms (Figure 2) produce three distinctive dewetting morphologies in thin films (Figure 3). Spinodal dewetting occurs when capillary waves in the liquid-air interface are spontaneously amplified to a height that is greater than the film thickness.[20] Since the amplitude of a specific wavelength will grow the fastest, spinodal dewetting results in evenly-distributed holes of the same size. Spinodal dewetting can occur only when the effective interface potential curve is concave down $\phi''(h) < 0$ in metastable and unstable scenarios (Figure 1). Homogeneous or thermal nucleation occurs when there is sufficient thermal energy to overcome the energy barrier around the $\phi''(h)$ sign change, resulting in a decrease in film thickness. Since thermal nucleation takes place over an extended period, the holes that form vary in size. Heterogeneous nucleation occurs when substrate defects or contaminants nucleate holes. The holes formed via heterogeneous nucleation generally appear larger than holes formed via spinodal dewetting and thermal nucleation. Heterogeneously-nucleated holes in a thin film appear equal in size since they are formed close in time to one another. Heterogeneous nucleation can occur at any $\phi''(h)$ sign in stable, metastable, and unstable scenarios.

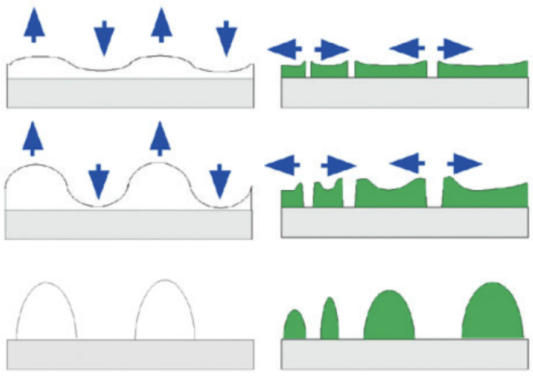

Figure 2. Schematic representations of spinodal dewetting (left) and thermal nucleation (right) over time.[21]

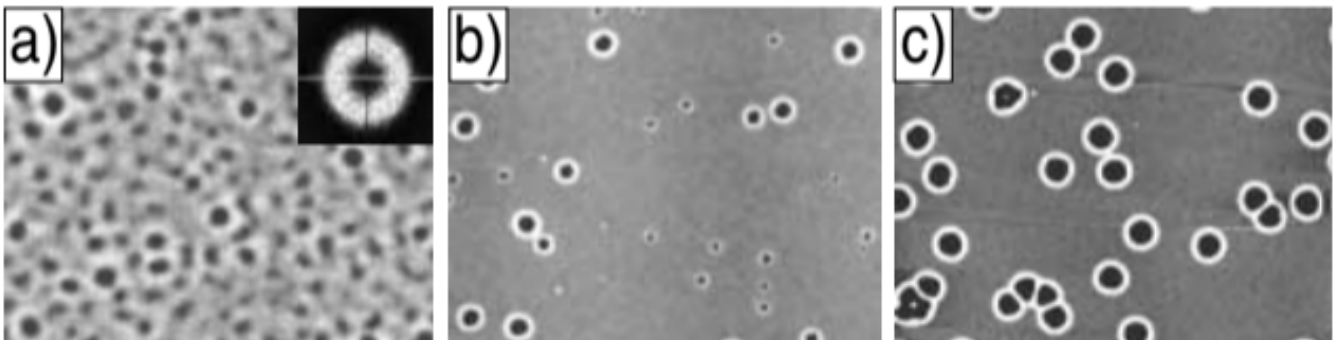

Figure 3. Three dewetting morphologies that are characteristic of (a) spinodal dewetting, (b) thermal nucleation, and (c) heterogeneous nucleation.[20]

1.2.3 Contact angle and spreading coefficient

Film wetting and dewetting have been extensively studied.[1-5, 20-28] The wettability of a substrate is demonstrated by the equilibrium contact angle formed between the solid-liquid interface and the liquid-vapor interface (Figure 4). This static contact angle θ_S, characteristic for each system involving a solid (s), liquid (l), and vapor (v) phase, was first described by Young in 1805:[29]

$$\gamma_{SV} = \gamma_{SL} + \gamma_{LV} \cos \theta_S \quad (1)$$

where γ represents surface tension (surface energy per unit area), SL represents the solid-liquid interface, SV represents the solid-vapor interface, and LV represents the liquid-vapor interface.

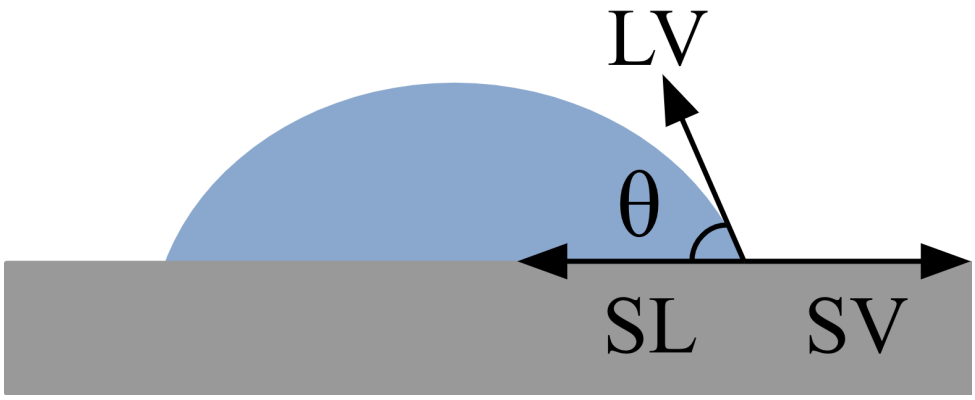

Figure 4. Contact angle formed between solid-liquid and liquid-vapor interfaces.

The wetting of a substrate can be complete or incomplete, and the wetting regime can be simplified via the spreading coefficient S:[28]

$$S = \gamma_{SV} - (\gamma_{SL} + \gamma_{LV}) \quad (2)$$

When S is positive, the static contact angle θ_S between the SL and LV interfaces is 0°, the SV surface tension is greater than the sum of the SL and LV surface tensions, and the liquid spreads completely over the substrate (Figure 5). When S is negative, the liquid does not spread entirely over the substrate, and θ_S is non-zero. When there is incomplete wetting, $0° < \theta_S < 90°$ indicates a mostly wetting regime, while $90° < \theta_S < 180°$ indicates a mostly nonwetting regime. Lastly, θ_S equal to 180° indicates that there is nonwetting or complete dewetting.

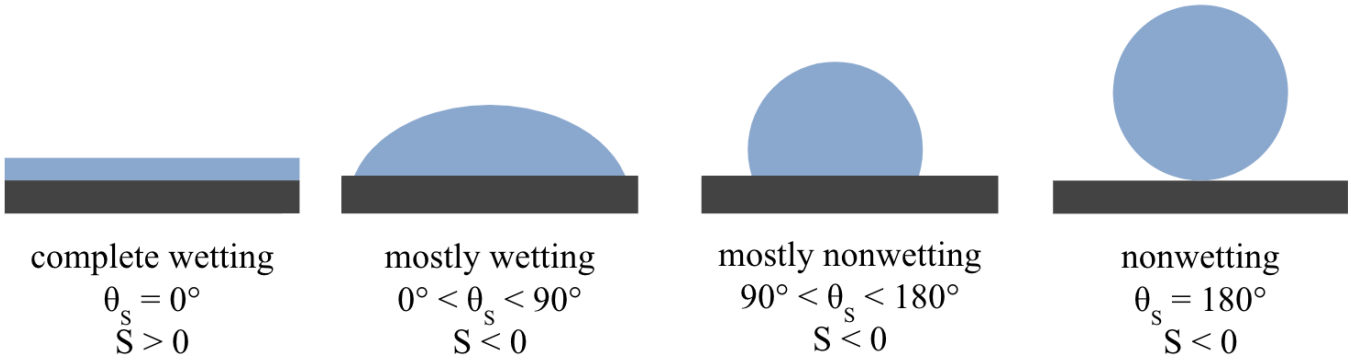

Figure 5. Various wetting regimes and static contact angles as functions of surface tensions.

While Young's equation describes the equilibrium static contact angle, this contact angle is rarely observed in practice. This deviation can be explained by Young's equation only accounting for the horizontal forces, as well as physical and chemical heterogeneities in the interfaces. Physical heterogeneities in the form of substrate roughness can be accounted for by using Wenzel's equation:[30]

$$\cos \theta_{actual} = r \cos \theta_S \quad (3)$$

where the roughness factor r is the ratio between the actual surface area and the surface area of a smooth surface with the same dimensions. As roughness increases, θ_{actual} increases when $\theta_S > 90°$, and θ_{actual} decreases when $\theta_S < 90°$.

Chemical heterogeneities in substrates can be accounted for by improved contact angle models and/or by dynamic contact angles. Improved static contact angle models have been proposed by Cassie and Israelachvili,[31-32] and continue to be studied and updated.[33] The Cassie equation applies to substrates with chemically heterogeneous (possessing distinct surface chemical groups) patches on the order of macrodomains, and the Israelachvili equation applies to substrates with chemically heterogeneous patches on the order of molecules or atoms. On the other hand, dynamic contact angles (advancing and receding) can be used to demonstrate the maximum and minimum contact angles for a given system.[34]

The spreading coefficient has implications for the film stability regime and dewetting mechanism in completely apolar and completely polar systems.[23] Films are stable when a liquid completely wets a surface ($S > 0$). When a liquid partially wets a surface ($S < 0$), films can be metastable or unstable.

Once holes form due to incomplete wetting or surface defects, they can coalesce and form larger holes (Figure 6).[21] Hole growth/coalescence is driven by the reduction in surface energy as smaller droplets aggregate, reducing the overall surface area of the film. This phenomenon is also known as Ostwald ripening, and it continues until the thermodynamic equilibrium is reached or until it is halted by dampening effects, such as crystallization.[35]

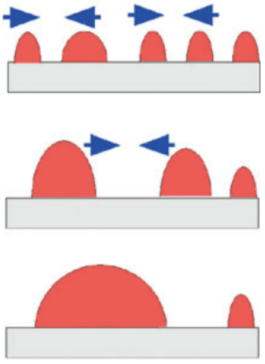

Figure 6. Schematic representation of aggregation/hole growth over time.[21]

1.3 Polymer thin film morphologies

1.3.1 General morphologies

Dewetted polymer thin films can display a variety of morphologies, and the scale of these morphologies depends on film thickness.[24] When holes initially form, they typically possess rims due to the different rates of hole nucleation and film migration.[20, 36-38] As the holes grow and merge, ribbon morphologies are formed. Eventually, the ribbons decay into droplets due to Rayleigh instabilities. If instability is present in the rim, droplet morphology can be seen directly after hole morphology. Various factors, such as temperature, can promote or inhibit the progression from hole to droplet morphology; by controlling these variables, it is possible to obtain kinetically-trapped nonequilibrium morphologies.

1.3.2 Mesoscale morphologies

Additional mesoscale morphologies have been observed in polymer thin films, such as dendrites, fractals, and honeycomb structures.[39] These morphologies are typically born out of Rayleigh instabilities, viscous fingering, diffusion-limited aggregation, and rim instabilities, to name a few mechanisms. Fingering instability is known for producing Saffman-Taylor fingers (Figure 7), which are characterized by puckering at the edges of holes.[40] Fingering instabilities can be seen when a low-viscosity fluid (typically air) is pushed into a high-viscosity fluid

(polymer solution), resulting in failure of viscoelastic materials. They are characterized by the wavelength, or the width of the fastest moving finger at a given location and time during growth.[41] The minimum wavelength is affected by factors such as the polymer-air interfacial velocity, the interfacial tension, and the shear viscosities of the fluids.

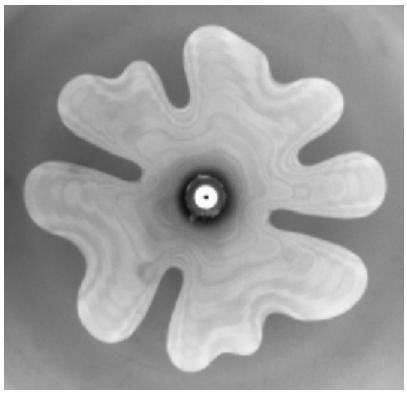

Figure 7. Dewetting morphology consisting of a hole with fingering instabilities.[42]

1.3.3 Fractals

Other common mesoscale morphologies in crystalline polymer thin films are fractals. It is widely accepted that fractals are formed via diffusion-limited aggregation, whereby small particles (polymers) irreversibly aggregate at a speed which is limited by their diffusion.[43-44] Fractals are shapes that possess self-similar features over multiple scales. They are typically continuous but irregularly shaped.

There are numerous ways to characterize fractals. Fractal dimension D describes how a fractal fills a given space and represents the structure's complexity; the D value is a measure of the increase in detail as the resolution increases.[43-45] In our study, binarized images of fractals formed by polymers are analyzed via the box-counting method. In this method, grids are overlaid on the images; boxes containing fractals are counted and used to calculate the D value:[43]

$$D = \lim_{r \to 0} \frac{log\, N(r)}{log\, (1/r)} \quad (4)$$

where r is the reduction coefficient and N(r) is the number of boxes containing fractals for each grid size. In our study, D values range from 1 to 2, where 1 corresponds to a solid line (1 dimension), and 2 corresponds to a completely-filled surface (2 dimensions).

Fractal dimension alone is insufficient to describe the shapes of fractals.[44-46] In Figure 8, both objects possess the same D value but appear very different from each other. Therefore, fractal lacunarity L is also required to meaningfully characterize fractals. Examples of objects with various L values are shown in Figure 9.

The L value can be thought of as the degree of structural variance within an object. We can calculate the lacunarity of a binarized image from the pixel distribution:[46]

$$\lambda = (\frac{\sigma}{\mu})^2 \quad (5)$$

In this equation, λ is the lacunarity when using a grid of a particular box size, σ is the standard deviation of pixels per box and μ is the mean number of pixels per box. The final lacunarity value is the mean λ value from all grid positions and orientations.

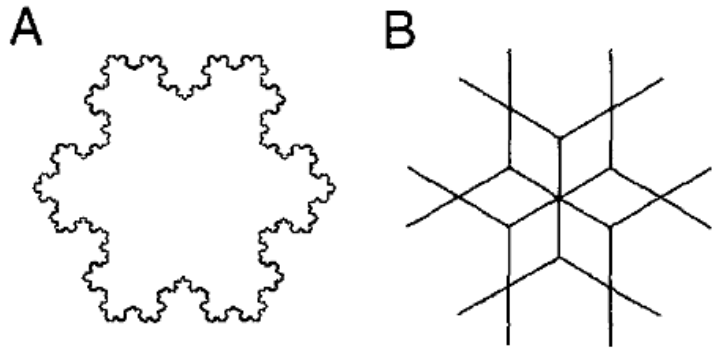

Figure 8. Two images with equal fractal dimension D values.[44]

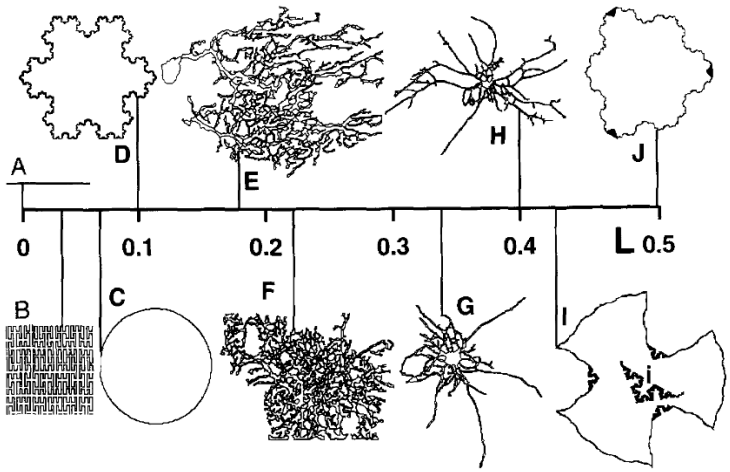

Figure 9. Images with a variety of fractal lacunarity L values.[44]

1.4 Polymer system of interest

1.4.1 System overview

The polymer system used in this research is shown in Figure 10: polydimethylsiloxane (PDMS) polymers serve as our substrate, silicon wafers serve as our solid support, and poly(vinyl alcohol) serves as the polymer thin film. Silicon wafers contain thin surface layers of silica as well as surface silanol groups, which give silicon wafers high surface energy and render their surfaces superhydrophilic.[47] Water completely wets the surface of silicon wafers ($\theta = 0°$). Silicon wafers are also atomically-smooth, allowing us to image PDMS substrates and PVOH thin films using atomic-force microscopy.

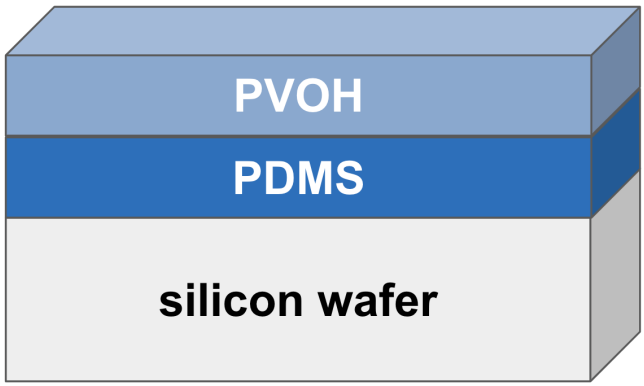

Figure 10. Silicon-supported PVOH-PDMS system used in this study.

1.4.2 Polydimethylsiloxane (PDMS)

Polydimethylsiloxane (PDMS) is a hydrophobic polymer that is used in many applications due to its unique properties. The average water contact angle is about 104.5°.[48] PDMS is optically clear, nontoxic, and highly flexible.[49] It is gas-permeable and resistant to most chemicals under 200 °C. Many of these properties originate from the structure of PDMS (Figure 11), which grants PDMS high flexibility and low surface tension compared to linear carbon-based polymers with similar structures. Due to its unique flexibility, it has a low glass-transition temperature of -125 ℃.[50] PDMS covalently bonds to silicon wafer through acid-catalyzed silanolysis (Figure 12, left) or by hydrolysis of a Si-O bond, followed by condensation with a surface silanol (Figure 12, right). In this research, PDMS polymers of various molecular weights are used to study the effects of substrate hydrophobicity and mobility on PVOH thin film stability.

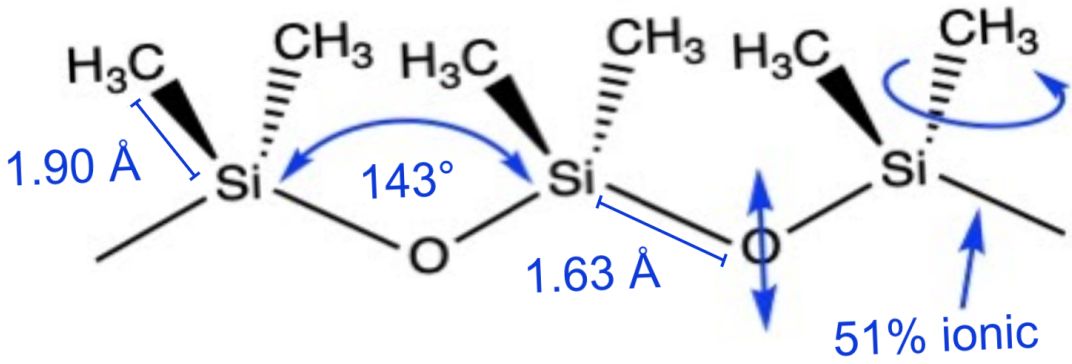

Figure 11. Polydimethylsiloxane structure.

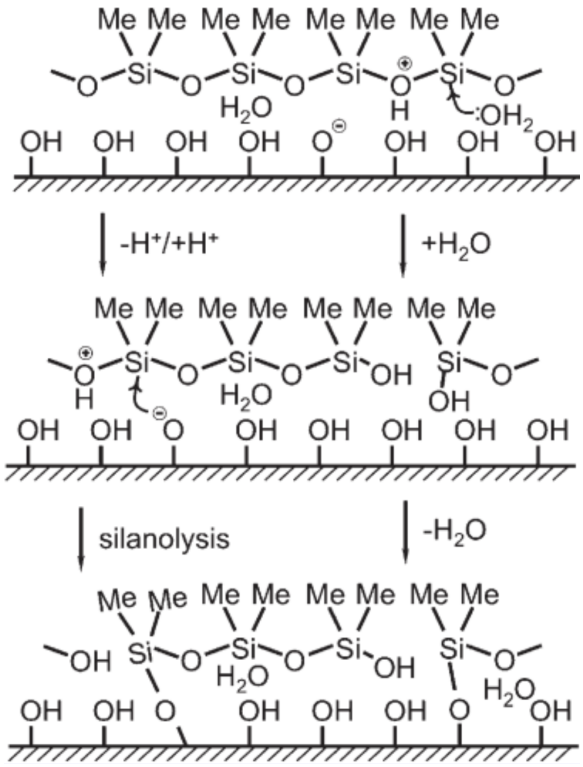

Figure 12. Polydimethylsiloxane bonded to silicon wafer through two different mechanisms.[50]

1.4.3 Poly(vinyl alcohol) (PVOH)

Poly(vinyl alcohol) (PVOH) is a water-soluble, non-toxic, and amphiphilic polymer. It is atatic yet semicrystalline.[51] PVOH is prepared from the hydrolysis of the acetate groups in poly(vinyl acetate) (PVA), shown in Figure 13. The PVOH degree of hydrophobicity and crystallinity can be controlled by the ratio of acetate groups to hydroxyl groups, where a greater ratio of acetate groups to hydroxyl groups results in a more hydrophobic, less crystalline polymer. This is due to the hydroxyl groups imparting greater hydrophilicity and more extensive intramolecular and intermolecular hydrogen bonding compared to the acetate groups. For bulk PVOH films prepared by hydrolyzing 99% of the PVA acetate groups, the advancing and receding water contact angles are 63° and 17°.[52]

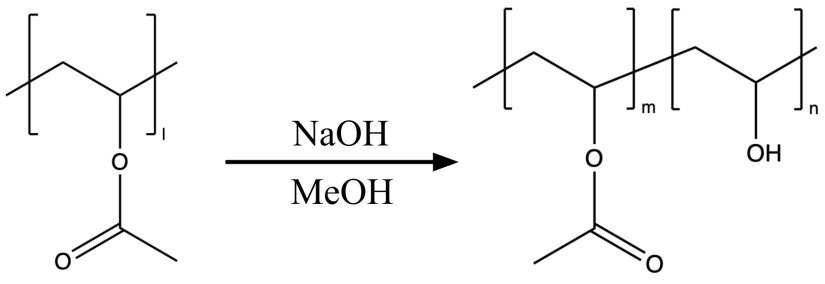

polyvinyl acetate (PVA) poly(vinyl alcohol) (PVOH)

Figure 13. Preparation of poly(vinyl alcohol) from the hydrolysis of poly(vinyl acetate).

1.5 Preparing PVOH thin films

Polymer thin films can be prepared using a variety of methods, including static adsorption and adsorptive spin coating. PVOH is the polymer of interest in this study since there are few literature reports on hydrophilic polymer thin films due to the challenging nature of the destabilizing polar interactions during solvent evaporation.[53] Despite these challenges, understanding and employing aqueous, nontoxic solutions to form hydrophilic polymer thin films are crucial to further this area of research, expand their applicability, and limit the toxicity of materials.

1.5.1 Static adsorption

One method that is used to hydrophilize hydrophobic surfaces is through the spontaneous adsorption of poly(vinyl alcohol) (PVOH) from aqueous solution.[52, 54-57] The adsorption occurs in two steps: physisorption due to the hydrophobic effect then crystallization at the liquid-solid interface.[55]

PVOH adsorption generally occurs within minutes,[52, 54] and the pseudoequilibrium PVOH thickness is dependent on the solution concentration.[52, 54, 56, 57-58] Rearrangement of PVOH films has been observed in PVOH solutions within a few seconds of adsorption,[58] and desorption of PVOH has been reported under different conditions.[59]

1.5.2 Polymer conformations

Common conformations in which polymer chains can adsorb onto a surface are train, loop, and tail conformations (Figure 14).[60] The conformation in which a polymer adsorbs, along with the surrounding chemical environment, can affect the chemical groups at the surface of the resulting thin film.

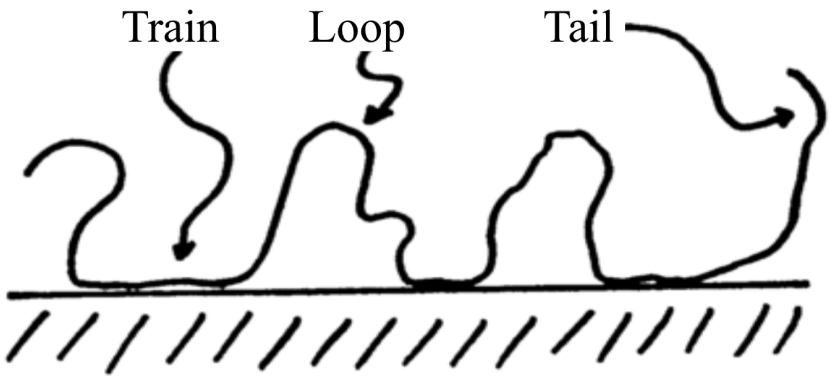

Figure 14. Conformations of adsorbed polymer chains.[60]

1.5.3 Adsorptive spin coating

Adsorptive spin coating is another method by which PVOH thin films can be used to hydrophilize hydrophobic surfaces. The steps to spin coating consist of deposition of aqueous PVOH solution, spin-up, spin-off, and solvent evaporation.[61-62] Between deposition and spin-up, we allow PVOH to adsorb spontaneously onto the hydrophobic substrate for 1 min.[63] Recently, our group proposed a new spin coating model[48] to address inconsistencies between the predictions made by the Meyerhofer model[62] and the results from our experiments. This new model accounts for the spontaneous adsorption of polymer onto a substrate, as well as the intermolecular interactions between polymers, such as crystallization.

1.6 Objective

In this study, we continue to investigate the stability and dynamics of PVOH thin films on hydrophobic PDMS substrates via static adsorption and spin coating. We also investigate the

stability of PVOH-PDMS thin films to water. We study two PVOH polymers with different degrees of hydrolysis and various PDMS molecular weights since substrate molecular weight and mobility have been shown to affect the adsorption and rearrangement of macromolecules.[64-65] Our results give additional insight to the multilayered structure of PVOH-PDMS thin films, ultimately assisting in the optimization of PVOH coatings for advanced and everyday applications.

II. MATERIALS AND METHODS

Materials

Silicon wafers (<100> oriented; P/B doped; 1-10 Ω·cm resistivity; 475-575 μm thick) were purchased from International Wafer Service. Trimethylsiloxy terminated polydimethylsiloxane polymers ($PDMS^{340}$, MW = 340 Da; $PDMS^{2k}$, MW = 2 kDa; $PDMS^{9k}$, MW = 9.430 kDa; $PDMS^{49k}$, MW = 49.350 kDa) were purchased from Gelest, Inc. Poly(vinyl alcohol) polymers ($PVOH^{88\%H}$, MW = 85-124 kDa, 87-89% hydrolyzed; $PVOH^{99\%H}$, MW = 89-98 kDa, 99+% hydrolyzed) were purchased from Sigma-Aldrich. Toluene (HPLC Grade) was purchased from Pharmco. Ethanol (ACS Grade) was purchased from Pharmco-Aaper. Water was purified using a Millipore Milli-Q Biocel System (resistivity ≥ 18.2 MΩ·cm) obtained from Millipore Corp. Oxygen gas (99.999%) was purchased from Airgas®. Nitrogen gas (99.998%) was purchased from Ivey Industries, Inc. All reagents were used without further purification. Glassware was cleaned in a base bath (potassium hydroxide in isopropyl alcohol and water), rinsed with deionized water, and stored in an oven at 110 °C until use.

Instrumentation

Silicon wafers were cleaned in a PDC-001 Harrick plasma cleaner. The hydrodynamic diameters of the PVOH chains in aqueous solution were measured using a Malvern Zetasizer Nano-ZS. PVOH thin films were spin-coated using a Laurell WS-650MZ-23NPPB spin coater. Nanoscopic PVOH thin film topography was captured using a Veeco Dimension 3100 atomic force microscope (AFM) with a silicon tip operating in tapping mode. Microscopic PVOH thin film morphology was imaged using an Olympus BX51 optical microscope in reflective dark field

mode. Thicknesses of surface layers were measured using a Gaertner Scientific LSE Stokes ellipsometer with a 70° incident angle and a He−Ne laser (λ = 632.8 nm) light source. The following refractive indices were used to calculate the surface layer thicknesses: air, $n_0 = 1$; silicon oxide and polymer layers, $n_1 = 1.46$; silicon substrate, $n_s = 3.85$, and $k_s = -0.02$. Advancing (θ_A) and receding (θ_R) water contact angles were obtained by adding and withdrawing water using a Gilmont syringe and a 24-gauge flat-tipped needle, and were digitally-measured using a Ramé-Hart telescopic goniometer.

Number of measurements on PDMS^{340}, PDMS^{2k}, and PDMS^{49k}

Each of the reported thickness values is an average of three readings at different locations per sample from 1 to 6 samples per batch from 1 to 8 different batches, for a total of 6 to 48 measurements. Each of the reported dynamic contact angle values is an average of four readings at different locations per sample from 1 to 4 samples per batch from 1 to 5 different batches, for a total of 4 to 36 measurements. Each AFM image included is chosen from 1 to 9 images per batch from 1 to 3 batches to determine the most representative morphology. Each optical microscope image included is chosen from 3 to 14 images per batch from 1 to 4 batches.

Number of measurements on PDMS^{9k}

Each of the reported thickness values is an average of three readings at different locations per sample from 2 to 3 samples per batch from 1 to 2 different batches, for a total of 6 to 15 measurements. Each of the reported dynamic contact angle values is an average of four readings at different locations per sample from 2 samples, for a total of 8 measurements. Each optical microscope image included is chosen from 3 to 4 images per batchfrom 1 to 2 batches.

Preparing silicon wafers

Silicon wafers were diced into 1.4 cm × 1.4 cm squares, rinsed thoroughly with deionized water, dried with compressed air, and further dried in an oven at 110 °C for 30 min. The silicon wafers were allowed to cool before being cleaned with oxygen plasma at ~300 mTorr for 15 min at high power (30 W). Surface charges were allowed to neutralize for 15 min prior to further treatment.

Fabricating PDMS substrates

PDMS was covalently attached to silicon wafer by dispensing 100 μL of PDMS onto a clean silicon wafer in a 20 mL glass scintillation vial and heating the capped vial at 100 °C for 24 h. After the reaction, each substrate was rinsed with toluene (3×), ethanol (3×), and Milli-Q water (3×). The substrates were dried under a nitrogen gas stream and desiccated overnight using $CaSO_4$.

Preparing PVOH solutions

PVOH crystals were dissolved in Milli-Q water by heating at 88-92 °C with stirring for 3 h in clean polypropylene bottles. The PVOH solutions were allowed to equilibrate for at least 3 days before characterization with dynamic light scattering.

1-min static adsorption of PVOH on PDMS

450 μL of PVOH solution was allowed to adsorb for 1 min onto a PDMS substrate. The $PDMS^{340}$ and $PDMS^{2k}$ samples were rinsed with Milli-Q water using a wash bottle (3×) while the $PDMS^{9k}$ and $PDMS^{49k}$ samples were rinsed (1×) with 1 mL of Milli-Q water. All samples were dried under a nitrogen gas stream and desiccated overnight using $CaSO_4$.

10-min immersive adsorption of PVOH on PDMS

PDMS substrates were placed in separate wells in a well plate. 3.4 mL PVOH solution was poured into each well to fully submerge the PDMS substrates. After 10 min, each sample was removed from solution, rinsed with Milli-Q water (3×), and dried under a nitrogen gas stream. The samples were desiccated overnight using $CaSO_4$.

Adsorptive spin coating of PVOH$^{0.1\ wt\%}$ on PDMS

After allowing 450 μL of PVOH$^{0.1\ wt\%}$ solution to adsorb onto each PDMS substrate for 1 min, the samples were spin-coated for 1 min at 900, 1400, 2200, 3500, 4800, or 6000 rpm under nitrogen gas. After spin coating, the visibly wet samples were allowed to dry while lying flat inside of a fume hood. All samples were desiccated overnight using $CaSO_4$.

Water annealing of PDMS-PVOH thin films

After PDMS-PVOH thin film fabrication via static adsorption or adsorptive spin coating, the samples were immersed in 125 Milli-Q water for 1 h in a custom-made glass holder placed horizontally in a 180 mL 70 x 50 mm crystallization dish. Immediately-annealed films were immersed in water directly after fabrication (omitting drying under a nitrogen gas stream). Delayed-annealed films were immersed in water 24 h after fabrication (followed by drying and overnight desiccation). After 1-h immersion in water, each sample was dried under a nitrogen gas stream and desiccated overnight using $CaSO_4$. Optical images were taken in the same locations on the samples before and after delayed-annealing.

PVOH fractal analysis

Optical images of PVOH films obtained at 500× magnification were analyzed. Adobe Photoshop 2023 was used to fill in images of PVOH$^{99\%H}$ fractals using the Brush, Magic Wand, and Fill tools. Fractal dimension (D) and lacunarity (L) values were determined through D_B Box

Counting by the FracLac plugin in ImageJ. PVOH percent coverage was determined through area analysis in ImageJ.

III. RESULTS AND DISCUSSION

3.1 Substrates (controls)

Silicon wafer, PDMS^{340}, PDMS^{2k}, PDMS^{9k}, and PDMS^{49k} were characterized prior to interaction with PVOH solution. As the molecular weight (MW) of the PDMS substrates increased, the thickness and hydrophobicity increased (Figures 15 and 16), as demonstrated by the increasing advancing contact angles (θ_A). While there were significant increases in PDMS thickness as the MW increased, the contact angles (CAs) for PDMS^{2k}, PDMS^{9k}, and PDMS^{49k} were similar, indicating that substrate mobility was the primary variable that differentiated the PDMS substrates.

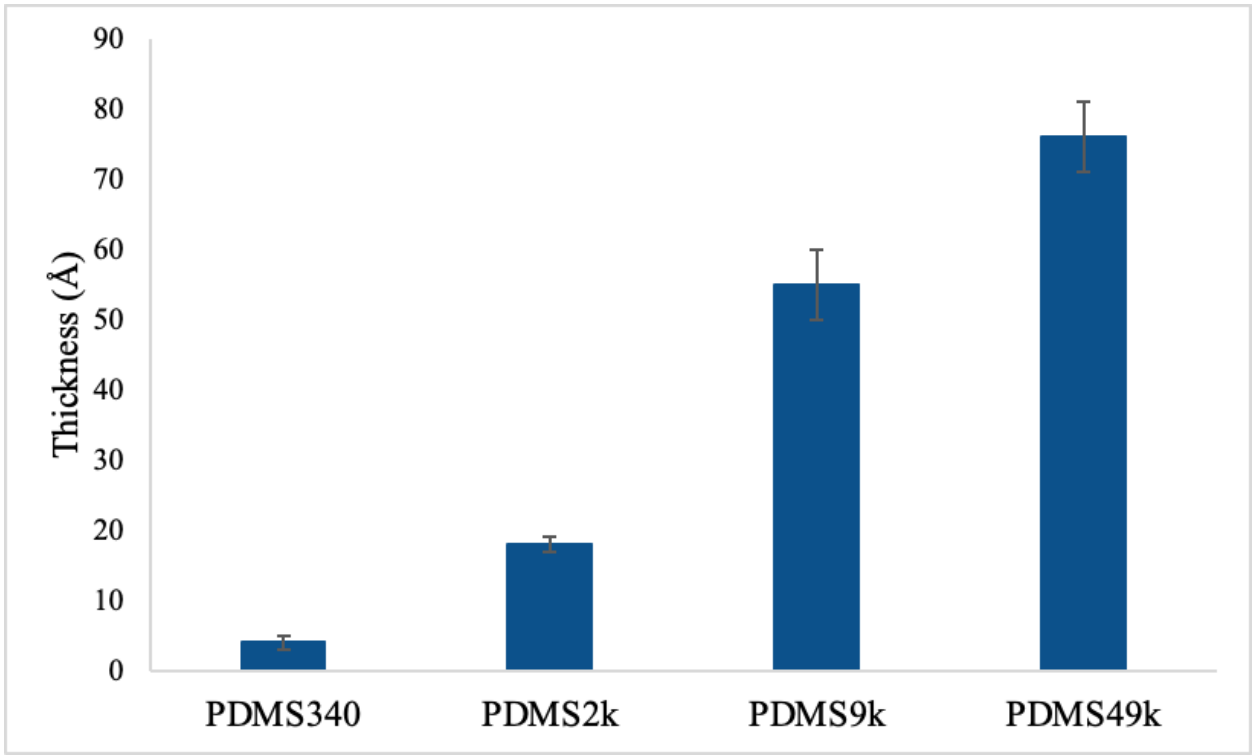

Figure 15. Thicknesses of PDMS substrates.

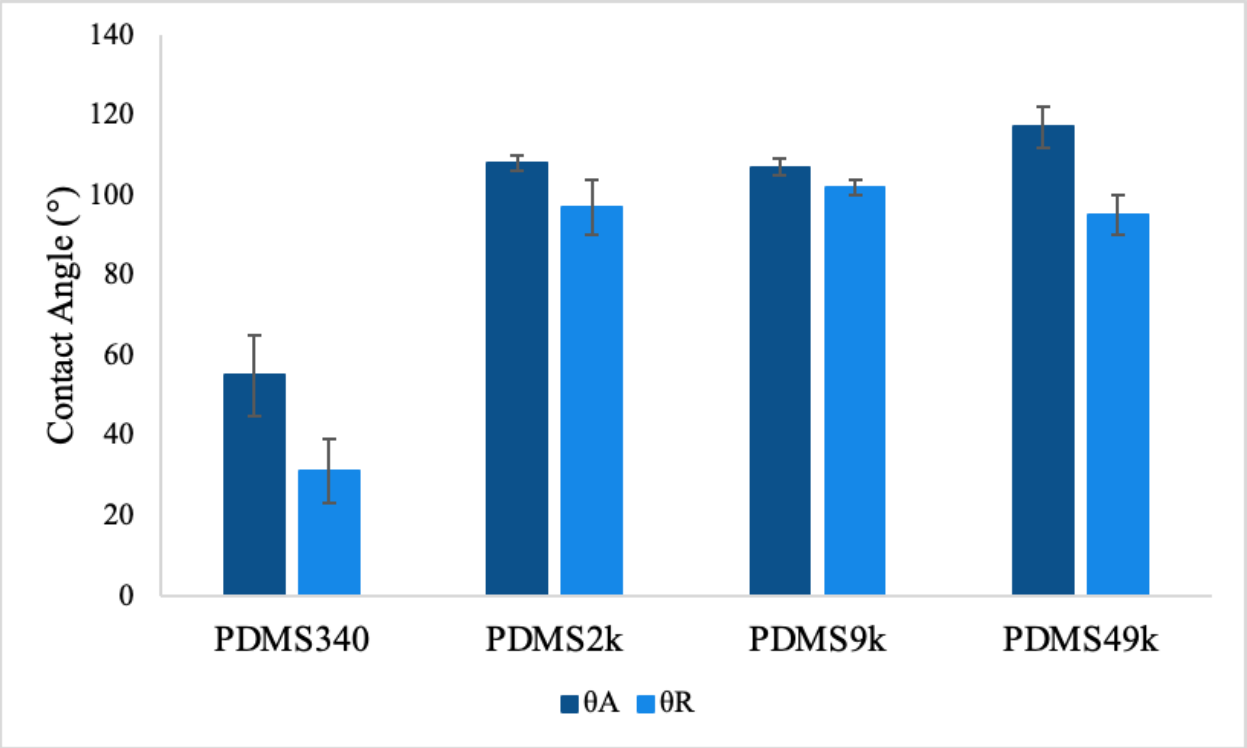

Figure 16. Contact angles of PDMS substrates.[48]

The PDMS substrate roughness increased as the MW increased (Table 1). The relatively high RMS roughness value of silicon wafer can be attributed to the visible contamination as a result of the high surface energy. The difference in RMS roughness was the greatest between PDMS^{2k} and PDMS^{9k}, which can be attributed to the increased heterogeneity in the attached PDMS chain lengths as the MW increases. Based on the AFM images, section analyses, and RMS roughness values of the substrates, PDMS^{340} most closely resembled silicon wafer in nanoscopic topography, while PDMS^{9k} and PDMS^{49k} closely resembled one another.

Table 1. AFM images, section analyses, and RMS roughness values of substrates (AFM image size: 1.25 µm × 5 µm; height scale: 10 nm).

Silicon wafer	$PDMS^{340}$	$PDMS^{2k}$	$PDMS^{9k}$	$PDMS^{49k}$
			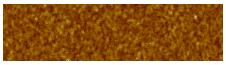	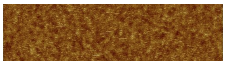
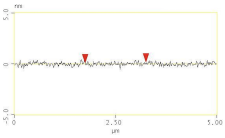	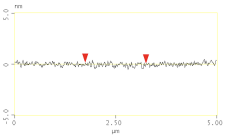	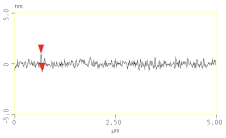	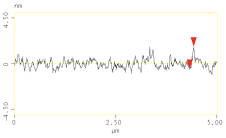	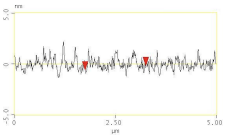
0.119 nm	0.087 nm	0.116 nm	0.234 nm	0.265 nm

The optical images show that the PDMS substrates were microscopically featureless, except for some patches of light that appeared to be randomly-distributed (Table 2). These patches of light were likely contaminants due to their scale and scarcity, and should be disregarded in subsequent optical images.

Table 2. Optical images of PDMS substrates (500× magnification).

$PDMS^{340}$	$PDMS^{2k}$	$PDMS^{9k}$	$PDMS^{49k}$
		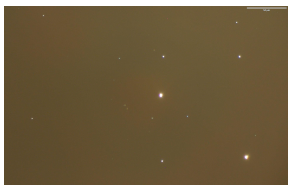	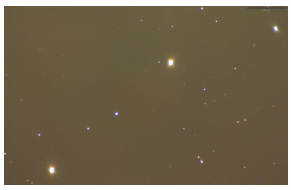

3.2 Static adsorption

3.2.1 Effect of time, [PVOH], and % hydrolysis

Following the static adsorption of PVOH onto $PDMS^{340}$ and $PDMS^{2k}$, the PVOH thin film thickness appeared to be independent of time and PVOH concentration ([PVOH]) (Figure 17), contrary to previous studies.[52, 54, 56, 57-58] The inconsistency between the results might be due to differences in substrates or PVOH solutions used in these studies. The PVOH film thickness increased with decreasing % hydrolysis and increasing PDMS MW, consistent with the hydrophobic effect acting as the driving force for spontaneous adsorption onto PDMS.

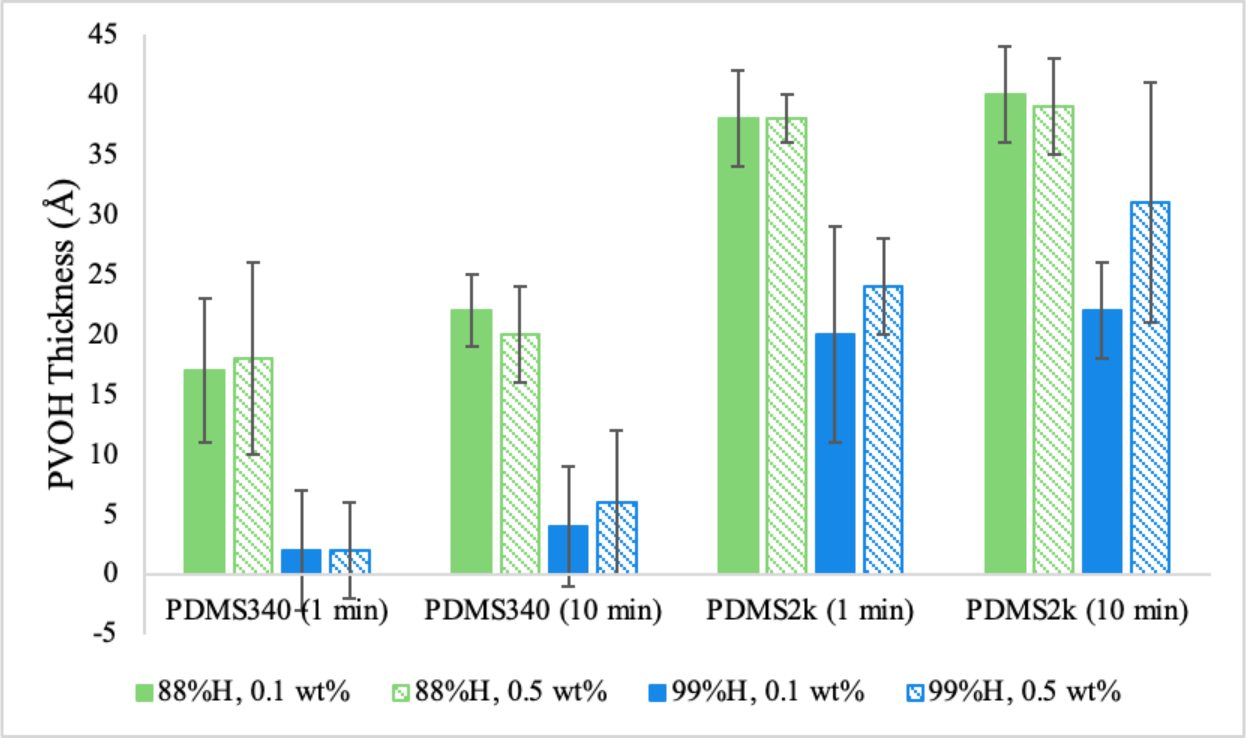

Figure 17. Thicknesses of PVOH-PDMS films after static adsorption for 1 or 10 min.

The θ_A of the adsorbed PVOH films on $PDMS^{340}$ and $PDMS^{2k}$ was also independent of time and [PVOH] (Figure 18). The θ_A was greater for $PVOH^{88\%H}$ films than $PVOH^{99\%H}$ films since $PVOH^{88\%H}$ contains relatively fewer hydroxyl groups and relatively more acetate groups. The θ_A of the $PVOH^{99\%H}$-$PDMS^{340}$ films was approximately equal to the θ_A of the $PDMS^{340}$ substrates, while the θ_A of the $PVOH^{88\%H}$-$PDMS^{340}$ films was higher. The θ_As of the $PVOH^{88\%H}$-$PDMS^{2k}$ and $PVOH^{99\%H}$-$PDMS^{2k}$ films were lower than the θ_A of the $PDMS^{2k}$ substrates. While PVOH can hydrophilize hydrophobic materials, including $PDMS^{2k}$, $PDMS^{340}$ substrates are equally as hydrophilic or more hydrophilic than PVOH and are not easily hydrophilized by PVOH. The receding contact angles (θ_R) show similar hydrophilicity across the different adsorption times, % hydrolysis, concentrations, and substrates (Appendix; Figure 51), indicating that similar kinds and amounts of hydrophilic chemical groups from PVOH and silicon wafer were exposed at the surface of the films.

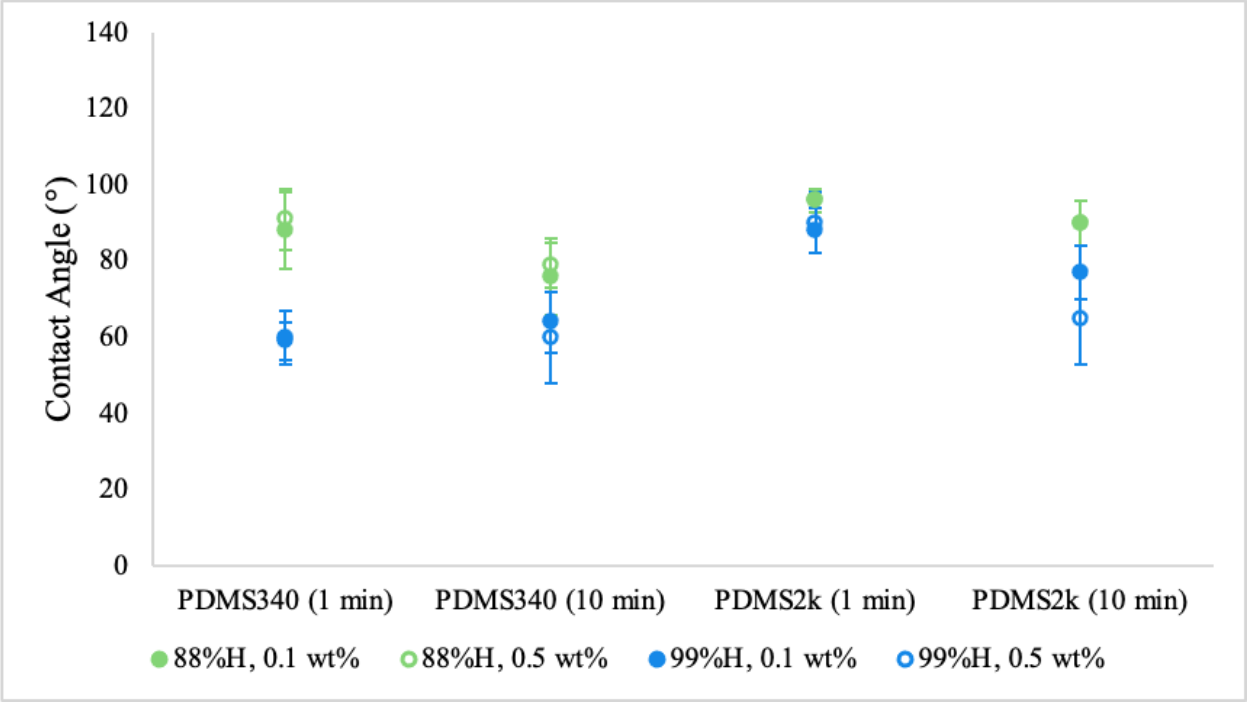

Figure 18. Advancing contact angles of PVOH-PDMS films after static adsorption for 1 or 10 min.

The AFM images of the adsorbed PVOH-PDMS^{340} films show that the nanoscopic morphology depended on the % hydrolysis and was independent of time and [PVOH] (Table 3). The PVOH$^{88\%H}$-PDMS^{340} films were significantly rougher than the PVOH$^{99\%H}$-PDMS^{340} films and the PDMS^{340} substrates (Table 1) and appeared to have undergone spinodal dewetting, evidenced by evenly-distributed holes across the films. Due to the increased contamination, the PVOH$^{99\%H}$-PDMS^{340} films were slightly rougher than the PDMS^{340} substrates. Disregarding the contaminants, the PVOH$^{99\%H}$-PDMS^{340} film morphology was very similar to that of the PDMS^{340} substrate. The negligible thickness of the PVOH$^{99\%H}$-PDMS^{340} films (Figure 17), the negligible change in contact angles after the adsorption of PVOH$^{99\%H}$ (Figures 16 and 18), and the similar morphology after the adsorption of PVOH$^{99\%H}$ suggest that PDMS^{340} lacks the necessary hydrophobic driving force for spontaneous PVOH$^{99\%H}$ adsorption.

Table 3. AFM images, section analyses, and RMS roughness values of PVOH-PDMS^{340} thin films after static adsorption for 1 or 10 min (AFM image size: 1.25 µm × 5 µm; height scale: 10 nm).

	PVOH$^{88\%H,\ 0.1\ wt\%}$	PVOH$^{88\%H,\ 0.5\ wt\%}$	PVOH$^{99\%H,\ 0.1\ wt\%}$	PVOH$^{99\%H,\ 0.5\ wt\%}$
1 min	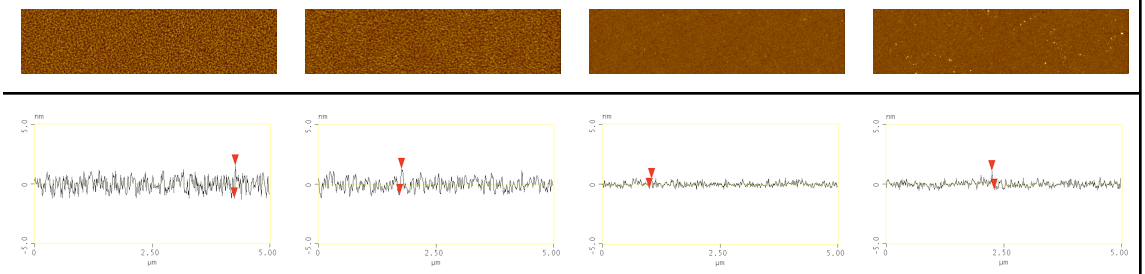			
	0.283 nm	0.232 nm	0.095 nm	0.113 nm
10 min	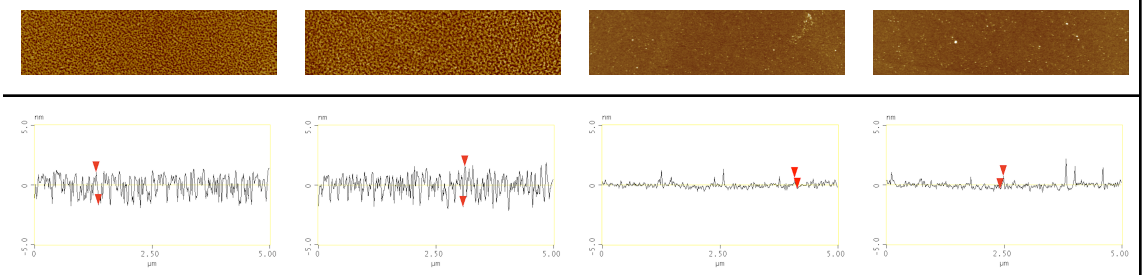			
	0.360 nm	0.404 nm	0.123 nm	0.130 nm

The AFM images of the adsorbed PVOH-PDMS^{2k} films all display significant dewetting (Table 4). Similar to the PVOH$^{88\%H}$-PDMS^{340} films, the PVOH$^{88\%H}$-PDMS^{2k} films contained evenly-distributed holes characteristic of spinodal dewetting. Also similar to the PVOH-PDMS^{340} films, the PVOH$^{88\%H}$-PDMS^{2k} films were rougher than the PVOH$^{99\%H}$-PDMS^{2k} films since the PVOH$^{88\%H}$-PDMS^{2k} film thickness was greater than the PVOH$^{99\%H}$-PDMS^{2k} film thickness.

Table 4. AFM images, section analyses, and RMS roughness values of PVOH-PDMS^{2k} thin films after static adsorption for 1 or 10 min (AFM image size: 1.25 µm × 5 µm; height scale: 10 nm).

	PVOH$^{88\%H,\ 0.1\ wt\%}$	PVOH$^{88\%H,\ 0.5\ wt\%}$	PVOH$^{99\%H,\ 0.1\ wt\%}$	PVOH$^{99\%H,\ 0.5\ wt\%}$
1 min	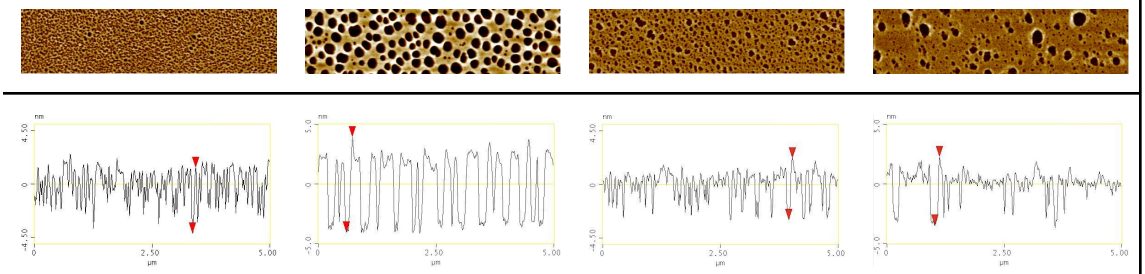			
	0.606 nm	1.256 nm	0.557 nm	0.544 nm
10 min	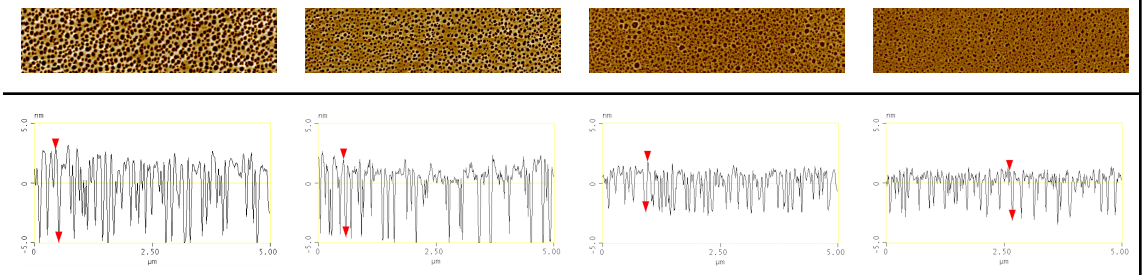			
	1.064 nm	0.979 nm	0.523 nm	0.444 nm

3.2.2 Effect of substrate

Since thickness, advancing contact angle, and morphology appeared to be independent of adsorption time and [PVOH], subsequent static adsorption experiments were conducted with only PVOH$^{0.1\ wt\%}$ for 1 min. Following the static adsorption of PVOH$^{0.1\ wt\%}$ onto PDMS^{340}, PDMS^{2k}, PDMS^{9k}, and PDMS^{49k} for 1 min, the PVOH film thickness appeared to depend on both the substrate and the % hydrolysis (Figure 19). Generally, the PVOH$^{88\%H,\ 0.1\ wt\%}$ films were thicker than the PVOH$^{99\%H,\ 0.1\ wt\%}$ films, as seen previously in section 3.2.1.

The PVOH thickness increased from PDMS^{340} to PDMS^{2k}, but decreased from PDMS^{2k} to PDMS^{49k} (Figure 19), following the hydrophobicity and substrate mobility trends. The hydrophobicity noticeably increases from PDMS^{340} to PDMS^{2k}, but remains fairly constant for PDMS^{2k}, PDMS^{9k}, and PDMS^{49k} (Figure 16). While the hydrophobicity is constant from PDMS^{2k}

to PDMS^{49k}, the MW continues to increase, resulting in longer polymer chains and greater substrate mobility. Similar to other studies,[63] substrate mobility destabilizes PVOH thin films, leading to thinning and less stable films. Substrate hydrophobicity and mobility appear to oppose each other in their effects on PVOH thickness, resulting in increasing PVOH film thickness as the PDMS MW (hydrophobicity) increases and as the substrate mobility decreases.

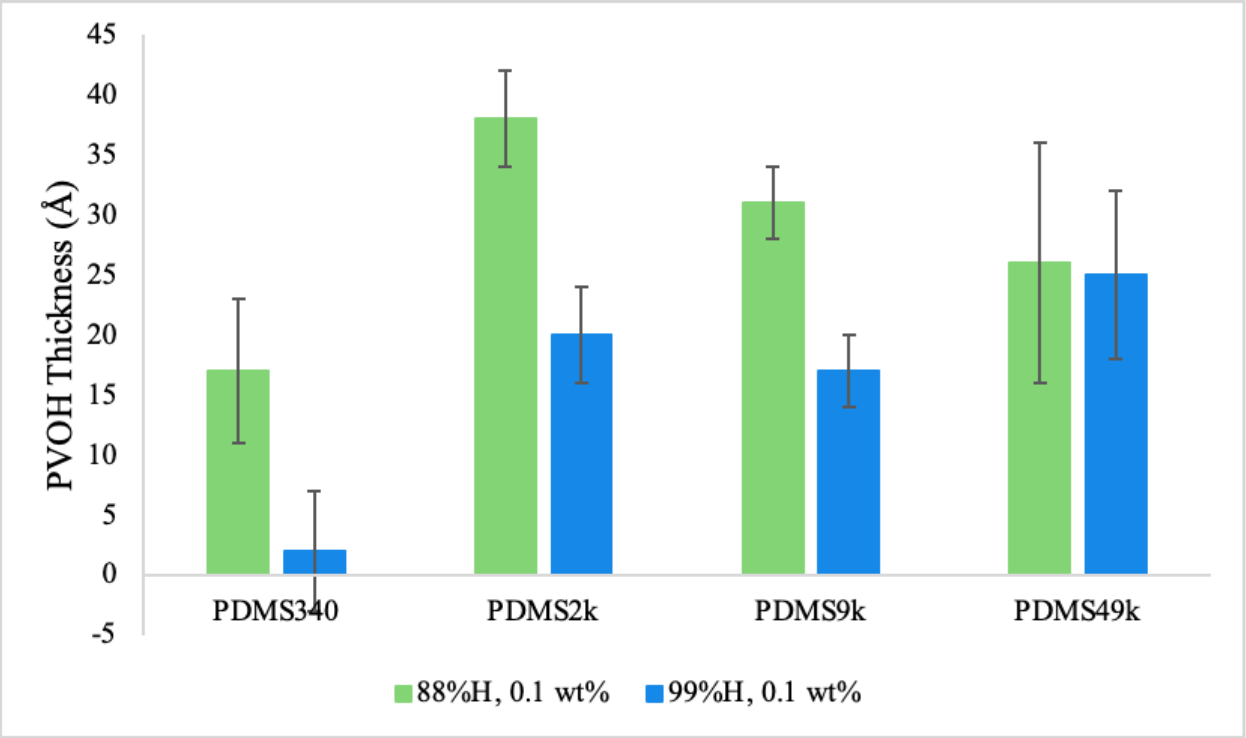

Figure 19. Thicknesses of PVOH-PDMS films after static adsorption for 1 min on various substrates.

Following the static adsorption of PVOH$^{0.1\ wt\%}$ onto PDMS^{340}, PDMS^{2k}, PDMS^{9k}, and PDMS^{49k} for 1 min, the θ_A increased with PDMS MW (Figure 20). The CAs of the PVOH films were generally independent of the % hydrolysis, except on PDMS^{340} due to the lack of discernible PVOH$^{99\%H,\ 0.1\ wt\%}$-PDMS^{340} film. The adsorption of PVOH$^{0.1\ wt\%}$ onto PDMS^{2k} resulted in a slight decrease in θ_A and a significant decrease in θ_R due to a significant amount of adsorbed PVOH film with continuity in between that of the low molecular weight and high molecular weight substrates. The adsorption of PVOH$^{0.1\ wt\%}$ onto PDMS^{9k} and PDMS^{49k} resulted in no

change in θ_A due to extensive dewetting and substrate exposure, but a significant decrease in θ_R due to the presence of the hydrophilic groups in PVOH.

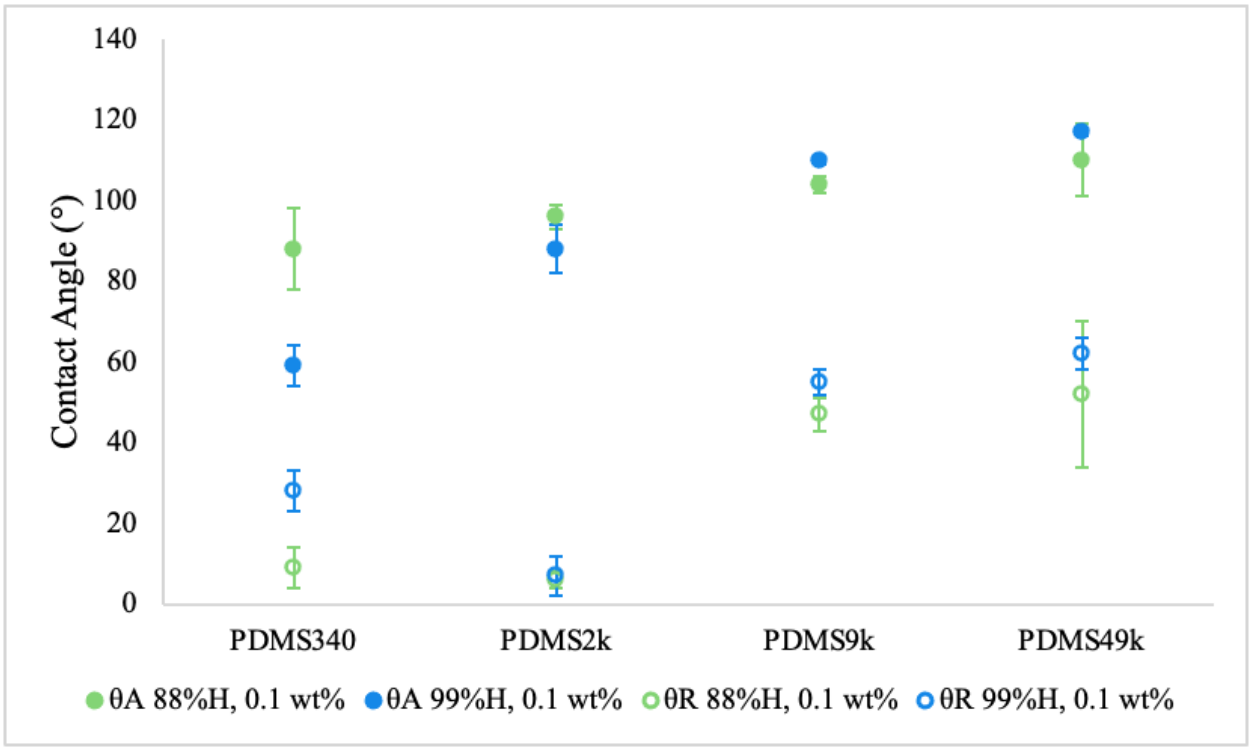

Figure 20. Contact angles of PVOH-PDMS films after static adsorption for 1 min on various substrates.

3.3 Water annealing following static adsorption

3.3.1 Effect of substrate

After annealing the PVOH$^{0.1\ wt\%}$-PDMS thin films in water for 1 h immediately following 1 min of static adsorption, the PVOH film thicknesses showed similar trends as the PDMS substrates before annealing: the PVOH film thickness was the least on PDMS^{340} and the greatest on PDMS^{2k} (Figure 21). The PVOH film thickness was within standard deviation before (Figure 19) and after (Figure 21) water annealing on PDMS^{340}, PDMS^{2k}, and PDMS^{49k} for each respective substrate and % hydrolysis. These results indicate that the PVOH films were composed of tightly-bound PVOH only. While the PVOH$^{99\%H,\ 0.1\ wt\%}$-PDMS^{9k} film thickness was within standard deviation before and after water annealing, the PVOH$^{88\%H,\ 0.1\ wt\%}$-PDMS^{9k} film

thickness decreased slightly after water annealing. However, the annealing experiments on PDMS^{9k} were performed once, so replicates are required to verify this result.

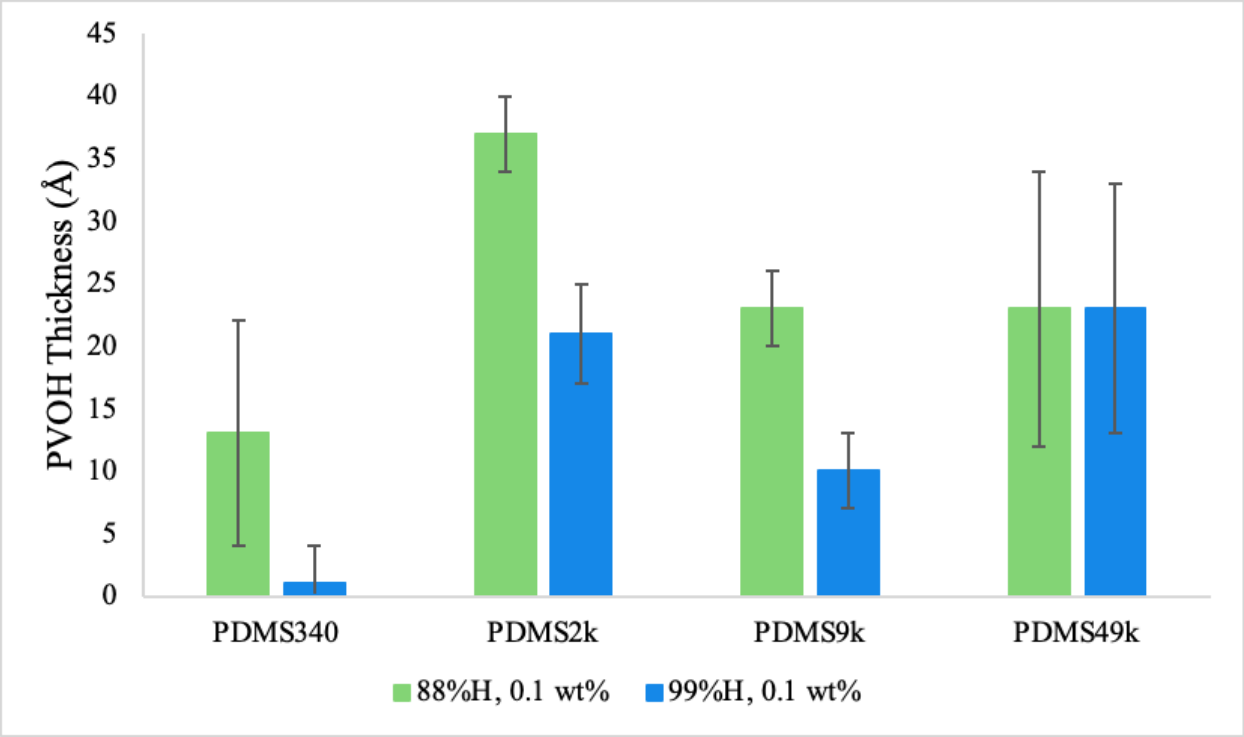

Figure 21. Thicknesses of PVOH-PDMS films after static adsorption for 1 min and water annealing after 0 h.

After annealing the PVOH$^{0.1\ wt\%}$-PDMS thin films in water for 1 h immediately following 1 min of static adsorption, the PVOH$^{0.1\ wt\%}$-PDMS CAs were very similar to those before annealing (Figures 20 and 22). The θ_A still increased with increasing PDMS MW, and the greatest difference between the CAs of the PVOH$^{88\%H}$ and PVOH$^{99\%H}$ films occurred on PDMS^{340} (Figure 22). Both the θ_A and θ_R of PVOH$^{99\%H,\ 0.1\ wt\%}$-PDMS^{340} decreased slightly after annealing, which can be attributed to the absorption of water or the removal of hydrophobic dust particles after annealing.

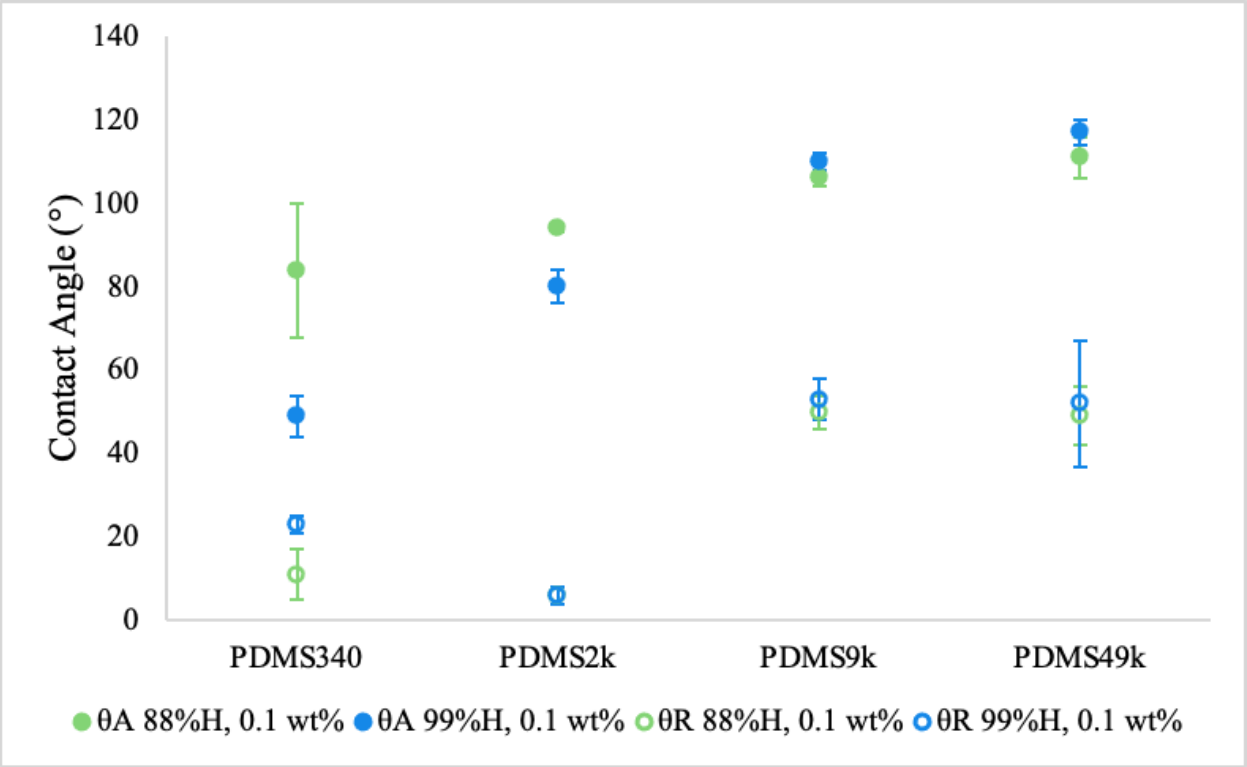

Figure 22. Contact angles of PVOH-PDMS films after static adsorption for 1 min and water annealing after 0 h.

The AFM images of the annealed PVOH-PDMS^{340} films (Table 5) show similar morphologies as the adsorbed films (Table 3). The annealed PVOH$^{88\%H}$ films appear to have undergone spinodal dewetting, while the annealed PVOH$^{99\%H}$ films appear similar in morphology to the adsorbed PVOH$^{99\%H}$ films and the PDMS^{340} substrate (Table 1). The RMS roughness values were also similar before and after annealing.

Table 5. AFM images, section analyses, and RMS roughness values of PVOH-PDMS^{340} thin films after static adsorption for 1 min and water annealing after 0 h (AFM image size: 1.25 µm × 5 µm; height scale: 10 nm).

PVOH$^{88\%H,\ 0.1\ wt\%}$	PVOH$^{88\%H,\ 0.5\ wt\%}$	PVOH$^{99\%H,\ 0.1\ wt\%}$	PVOH$^{99\%H,\ 0.5\ wt\%}$
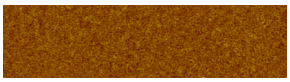	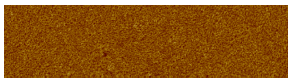	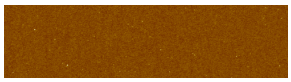	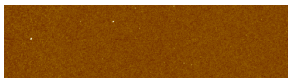
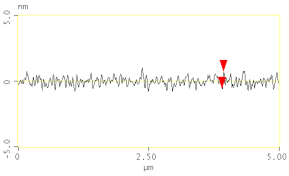	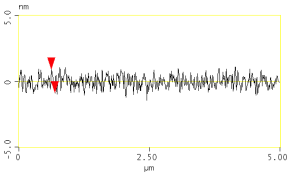	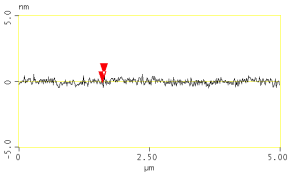	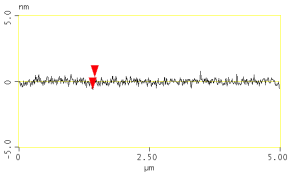
0.164 nm	0.264 nm	0.094 nm	0.104 nm

The AFM images of the annealed PVOH-PDMS^{2k} films (Table 6) also show similar morphologies as the adsorbed films (Table 4). All of the annealed films appear to have undergone spinodal dewetting. The PVOH$^{99\%H}$-PDMS^{2k} films were generally less rough than the PVOH$^{88\%H}$-PDMS^{2k} films, in agreement with previous trends in the roughness values of the adsorbed films.

Table 6. AFM images, section analyses, and RMS roughness values of PVOH-PDMS^{2k} thin films after static adsorption for 1 min and water annealing after 0 h (AFM image size: 1.25 µm × 5 µm; height scale: 10 nm).

PVOH$^{88\%H,\ 0.1\ wt\%}$	PVOH$^{88\%H,\ 0.5\ wt\%}$	PVOH$^{99\%H,\ 0.1\ wt\%}$	PVOH$^{99\%H,\ 0.5\ wt\%}$
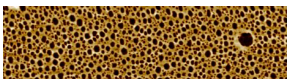	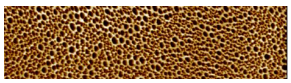	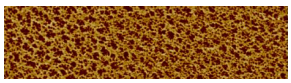	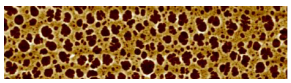
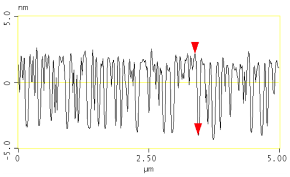	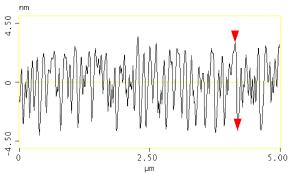	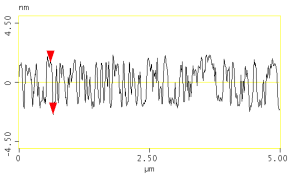	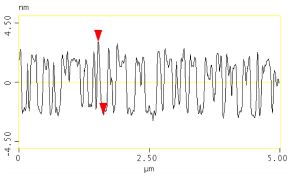
0.904 nm	0.839 nm	0.563 nm	0.834 nmn

The optical images of the adsorbed and annealed PVOH$^{0.1\ wt\%}$-PDMS^{340} films (Table 7a) appear similar to the optical image of the PDMS^{340} substrate (Table 2), indicating that the PVOH

-PDMS^{340} film feature sizes are not large enough to be detected via optical microscopy. However, the PVOH film feature sizes are large enough to image via optical microscopy on PDMS^{2k}, PDMS^{9k}, and PDMS^{49k} (Tables 7b-7d).

Table 7a. Optical images of PVOH-PDMS^{340} thin films after static adsorption for 1 min and water annealing after 0 h (500× magnification).

Substrate	Treatment	[PVOH] (wt%)	PVOH$^{88\%H}$	PVOH$^{99\%H}$
PDMS^{340}	Adsorbed	0.1		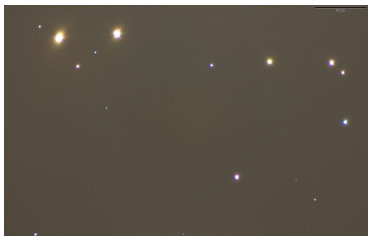
	Annealed			

The adsorbed PVOH$^{88\%H,\ 0.1\ wt\%}$-PDMS^{2k} morphology consists of droplet-like fractals, while the adsorbed PVOH$^{99\%H,\ 0.1\ wt\%}$-PDMS^{2k} morphology consists of branch-like fractals (Table 7b). The fractals did not appear in the annealed PVOH$^{88\%H,\ 0.1\ wt\%}$-PDMS^{2k} optical image, but did appear in the annealed PVOH$^{99\%H,\ 0.1\ wt\%}$-PDMS^{2k} optical image, along with the growth of smaller fractals. While the optical images of the adsorbed and annealed PVOH-PDMS^{2k} films were not taken on the same sample, these trends indicate that the PVOH$^{0.1\ wt\%}$-PDMS^{2k} films rearrange and redistribute polymer from the fractals to the bare substrate after annealing, resulting in PVOH$^{88\%H,\ 0.1\ wt\%}$-PDMS^{2k} film feature sizes that are too small to image via optical microscopy.

Table 7b. Optical images of PVOH-PDMS^{2k} thin films after static adsorption for 1 min and water annealing after 0 h (500× magnification).

Substrate	Treatment	[PVOH] (wt%)	PVOH$^{88\%H}$	PVOH$^{99\%H}$
PDMS^{2k}	Adsorbed	0.1	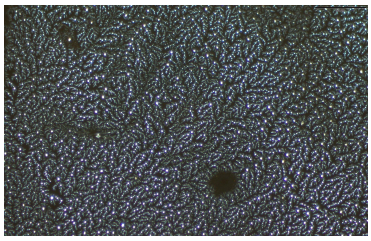	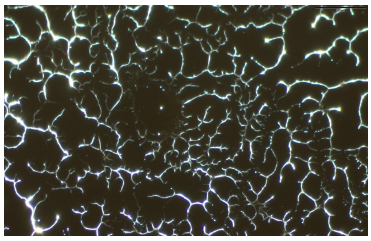
	Annealed		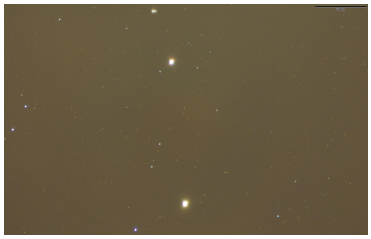	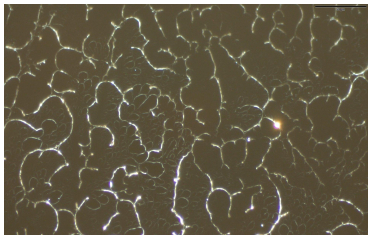

The optical images of the adsorbed and annealed PVOH on PDMS^{9k} (Table 7c) and PDMS^{49k} (Table 7d) also show droplet-like PVOH$^{88\%H}$ fractals and branch-like PVOH$^{99\%H}$ fractals. The morphologies appear similar on PDMS^{9k} and PDMS^{49k}, but are slightly larger on the PDMS^{49k} substrates due to the higher MW and greater substrate mobility. The film morphology appears independent of [PVOH] on PDMS^{49k} (Table 7d). After annealing, the PVOH$^{88\%H}$ droplets appear smaller and more numerous on PDMS^{9k} (Table 7c). The PVOH$^{99\%H}$ branches appear more irregular in width after annealing on both PDMS^{9k} and PDMS^{49k}. These changes after annealing suggest that some PVOH$^{99\%H}$ polymer chains from the existing branches dissociate and form new branches. This also suggests that the strength by which PVOH$^{99\%H}$ branches adhere to the substrate can vary.

Table 7c. Optical images of PVOH-PDMS^{9k} thin films after static adsorption for 1 min and water annealing after 0 h (500× magnification).

Substrate	Treatment	[PVOH] (wt%)	PVOH$^{88\%H}$	PVOH$^{99\%H}$
PDMS^{9k}	Adsorbed	0.1	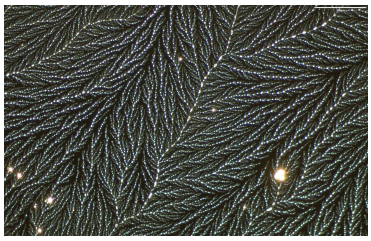	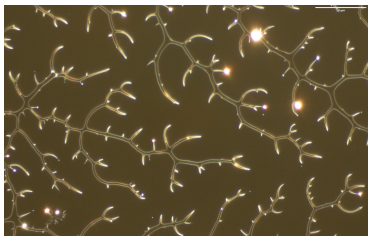
	Annealed		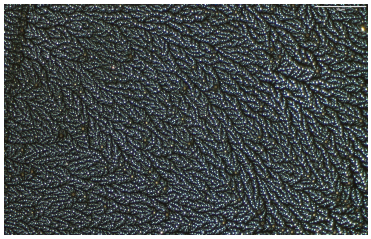	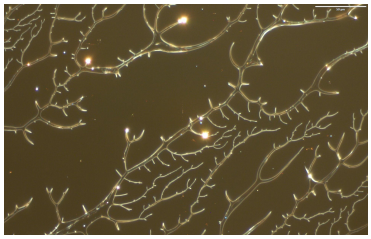

Table 7d. Optical images of PVOH-PDMS^{49k} thin films after static adsorption for 1 min and water annealing after 0 h (500× magnification).

Substrate	Treatment	[PVOH] (wt%)	PVOH$^{88\%H}$	PVOH$^{99\%H}$
PDMS^{49k}	Adsorbed	0.1	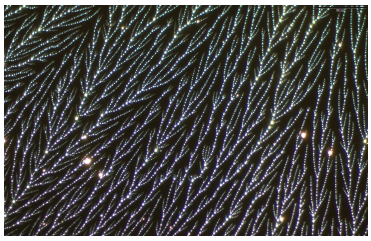	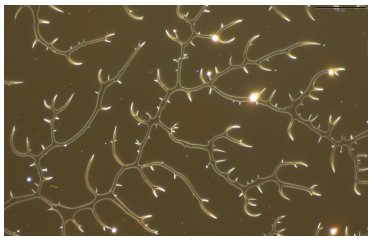
		0.5	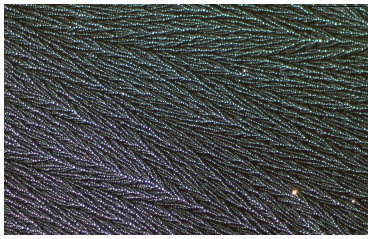	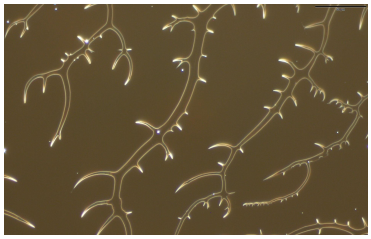
	Annealed	0.1	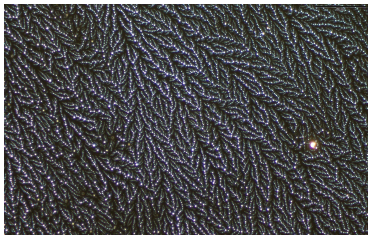	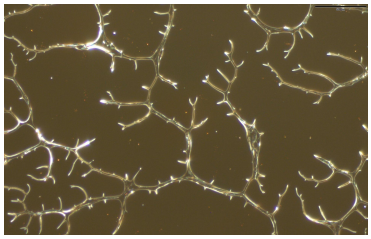
		0.5	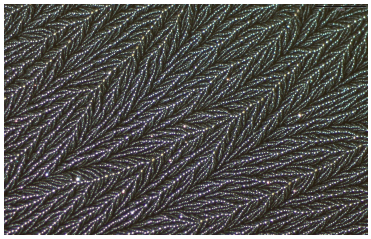	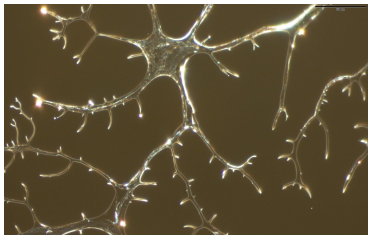

3.3.2 Effect of time before annealing

The PVOH$^{0.1\ wt\%}$-PDMS^{9k} films were annealed in water 0 h after ("immediate-annealing") or 24 h after ("delayed-annealing") 1 min of static adsorption in order to determine the effect of time before annealing on thickness, wettability, and morphology. All optical images of the delayed-annealed films were taken in the same location as before annealing. The PVOH$^{88\%H,\ 0.1\ wt\%}$-PDMS^{9k} film thickness was the same after immediate-annealing and delayed-annealing

(Figure 23), and was slightly less than the adsorbed PVOH$^{88\%H,\ 0.1\ wt\%}$-PDMS^{9k} film thickness. The delayed-annealed PVOH$^{99\%H,\ 0.1\ wt\%}$-PDMS^{9k} film thickness was equal to the adsorbed thickness and was greater than the immediately-annealed thickness since PVOH$^{99\%H}$ films are more hydrophilic and crystalline than PVOH$^{88\%H}$ films. The results can also be attributed to the greater crystallinity of PVOH$^{99\%H}$ compared to PVOH$^{88\%H}$, resulting in greater stability when the PVOH$^{99\%H}$ films are allowed to dry and crystallize more thoroughly.

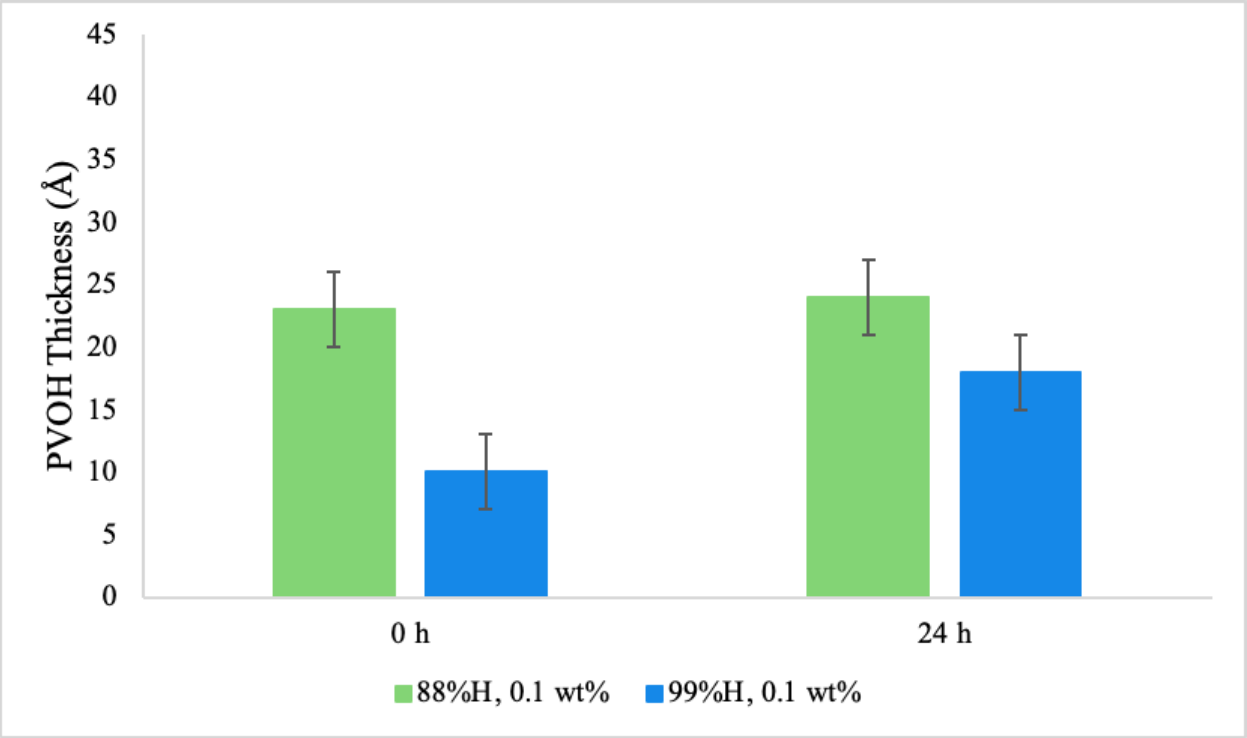

Figure 23. Thicknesses of PVOH-PDMS^{9k} films after static adsorption for 1 min and water annealing after 0 or 24 h.

The contact angles of the annealed PVOH$^{0.1\ wt\%}$-PDMS^{9k} films were the same across the different % hydrolysis and times before annealing (Figure 24).

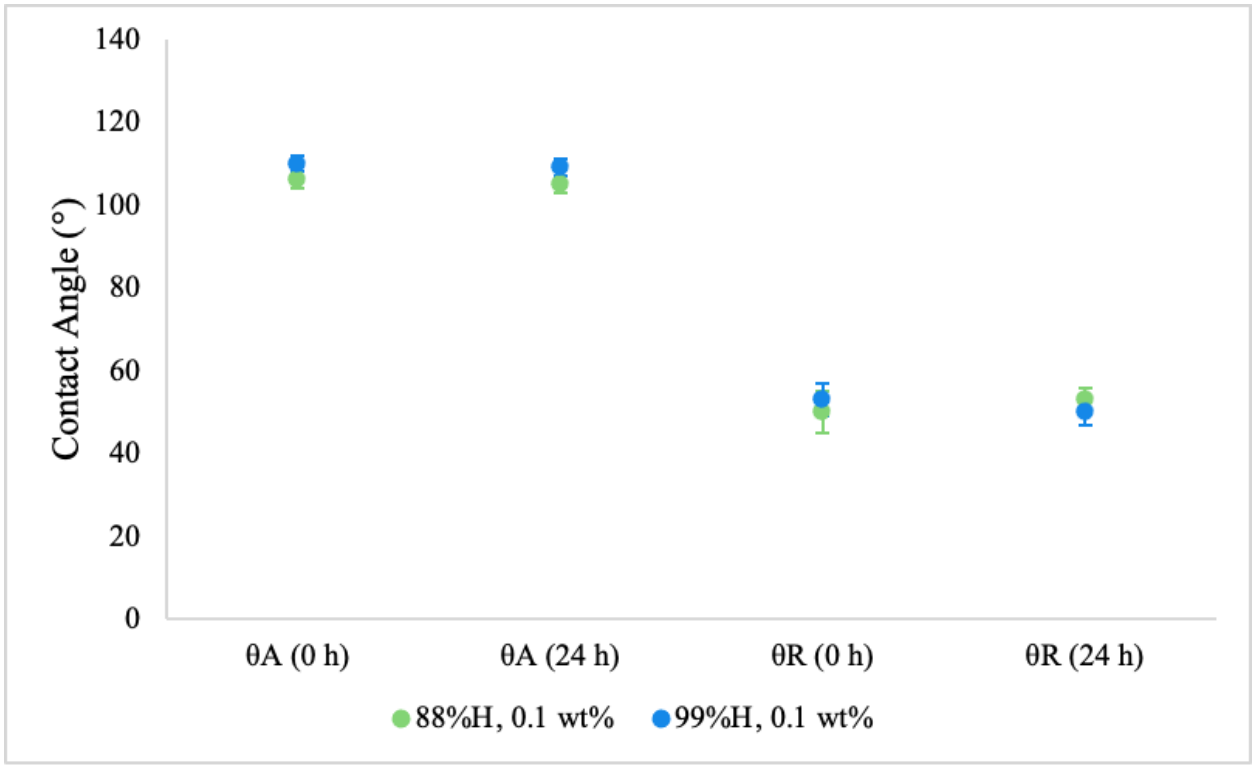

Figure 24. Contact angles of PVOH-PDMS^{9k} films after static adsorption for 1 min and water annealing after 0 or 24 h.

The optical images of the PVOH$^{88\%H,\ 0.1\ wt\%}$-PDMS^{9k} films show that the PVOH$^{88\%H,\ 0.1\ wt\%}$ fractals became similarly homogeneous in size and distribution after immediate-annealing and delayed-annealing (Table 8). On the other hand, the changes in size and distribution of the immediately-annealed and the delayed-annealed PVOH$^{99\%H,\ 0.1\ wt\%}$ fractals differed; the immediately-annealed fractals appeared more even in size but less even in distribution compared to the delayed-annealed fractals. While the images of the adsorbed and immediately-annealed films were captured on different samples, the time before annealing appears to influence the thickness and morphology of the adsorbed PVOH$^{88\%H,\ 0.1\ wt\%}$-PDMS^{9k} films differently than the PVOH$^{99\%H,\ 0.1\ wt\%}$-PDMS^{9k} films, which can be attributed to the differences in the degree of crystallinity of the two polymers.

Table 8. Optical images of PVOH-PDMS^{9k} thin films after static adsorption for 1 min and water annealing after 0 or 24 h (500× magnification).

Treatment	[PVOH] (wt%)	PVOH$^{88\%H}$	PVOH$^{99\%H}$
Adsorbed	0.1	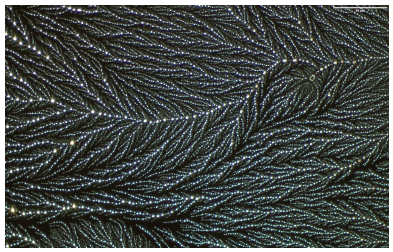	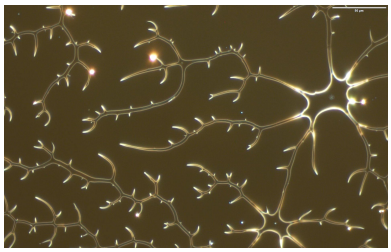
0 h-later annealed	0.1	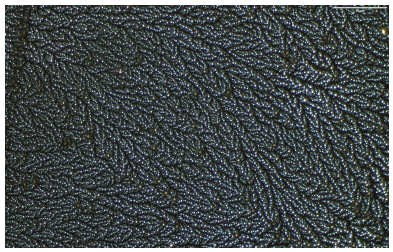	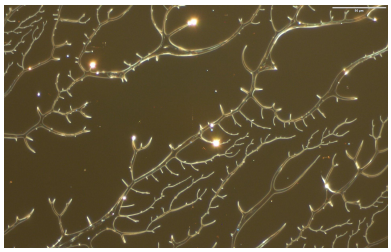
24 h-later annealed	0.1	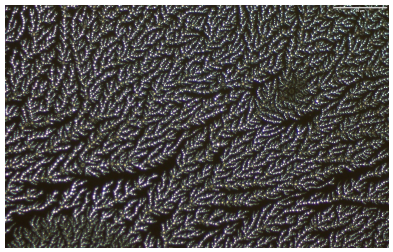	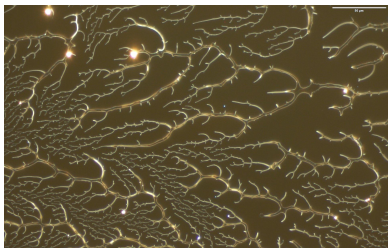

3.4 Fractal analysis following static adsorption and water annealing

3.4.1 Effect of time before annealing

The morphologies of the adsorbed, immediately-annealed, and the delayed-annealed PVOH$^{0.1\ wt\%}$-PDMS^{9k} films were analyzed by determining the % PVOH surface coverage, the fractal dimension D values, and the fractal lacunarity L values. The % surface coverage was independent of the % hydrolysis, but slightly depended on the film treatment (Figure 25). The % surface coverage of the adsorbed films was equal to that of the delayed-annealed films, and was slightly greater than that of the immediately-annealed films.

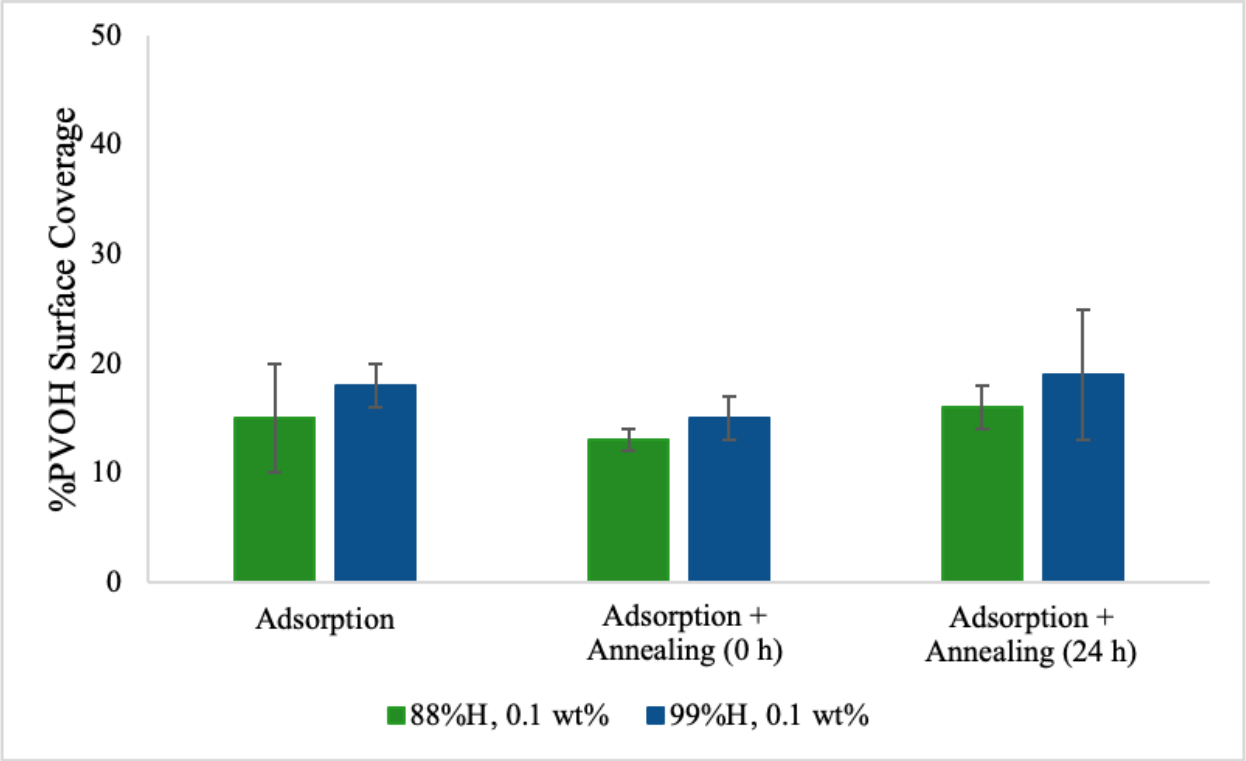

Figure 25. % PVOH surface coverage on PDMS^{9k} after static adsorption for 1 min and water annealing after 0 or 24 h.

The D values of the PVOH$^{88\%H,\ 0.1\ wt\%}$-PDMS^{9k} films were equal across the different treatments (Figure 26). The D value of the delayed-annealed PVOH$^{99\%H,\ 0.1\ wt\%}$-PDMS^{9k} film was slightly greater than the D values of the adsorbed and immediately-annealed PVOH$^{99\%H,\ 0.1\ wt\%}$-PDMS^{9k} films. This result is consistent with the delayed-annealed PVOH$^{99\%H,\ 0.1\ wt\%}$-PDMS^{9k} fractals displaying the greatest complexity out of all three treatments (Table 8).

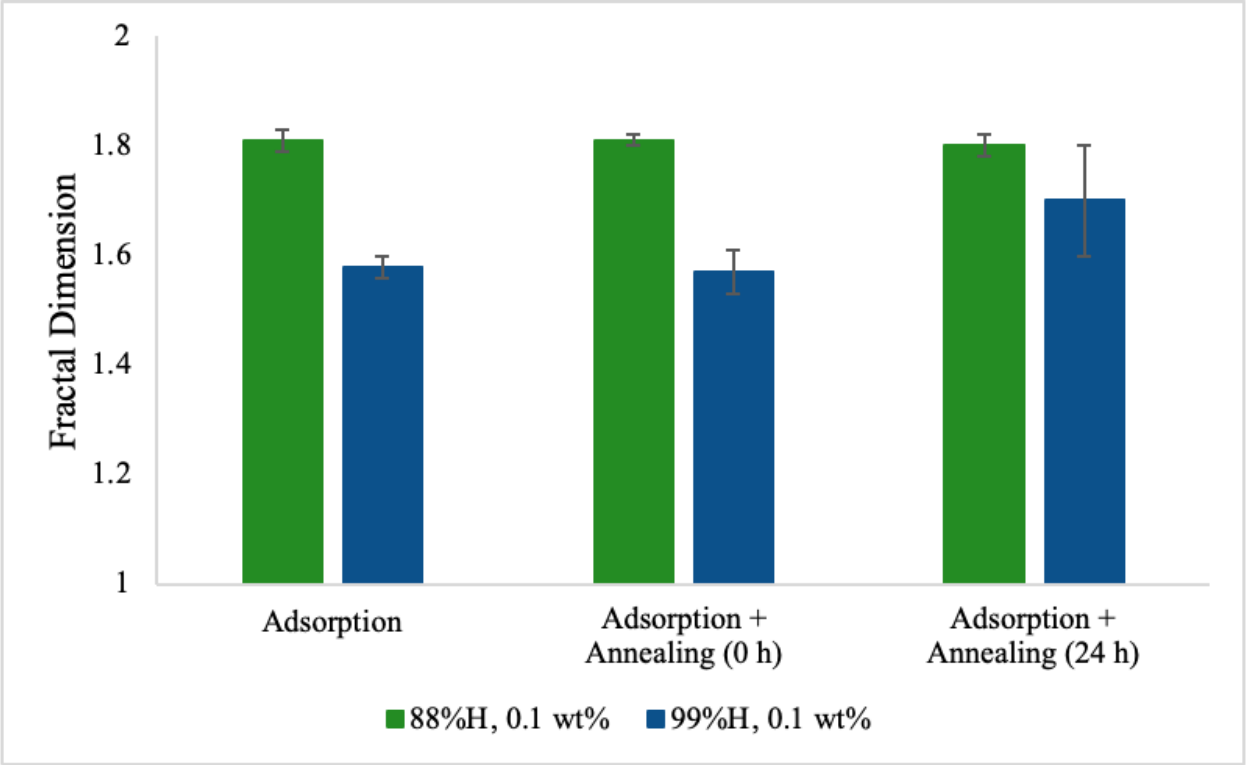

Figure 26. Fractal dimension D of PVOH-PDMS^{9k} films after static adsorption for 1 min and water annealing after 0 or 24 h.

Similar to the D values, the L values of the PVOH$^{88\%H,\ 0.1\ wt\%}$-PDMS^{9k} films were also equal across the different treatments (Figure 27). The L value of the delayed-annealed PVOH$^{99\%H,\ 0.1\ wt\%}$-PDMS^{9k} film was slightly less than the L values of the adsorbed and immediately-annealed PVOH$^{99\%H,\ 0.1\ wt\%}$-PDMS^{9k} films. This result is also consistent with the optical image of the delayed-annealed PVOH$^{99\%H,\ 0.1\ wt\%}$-PDMS^{9k} film appearing more homogenous than the adsorbed and the immediately-annealed PVOH$^{99\%H,\ 0.1\ wt\%}$-PDMS^{9k} films (Table 8).

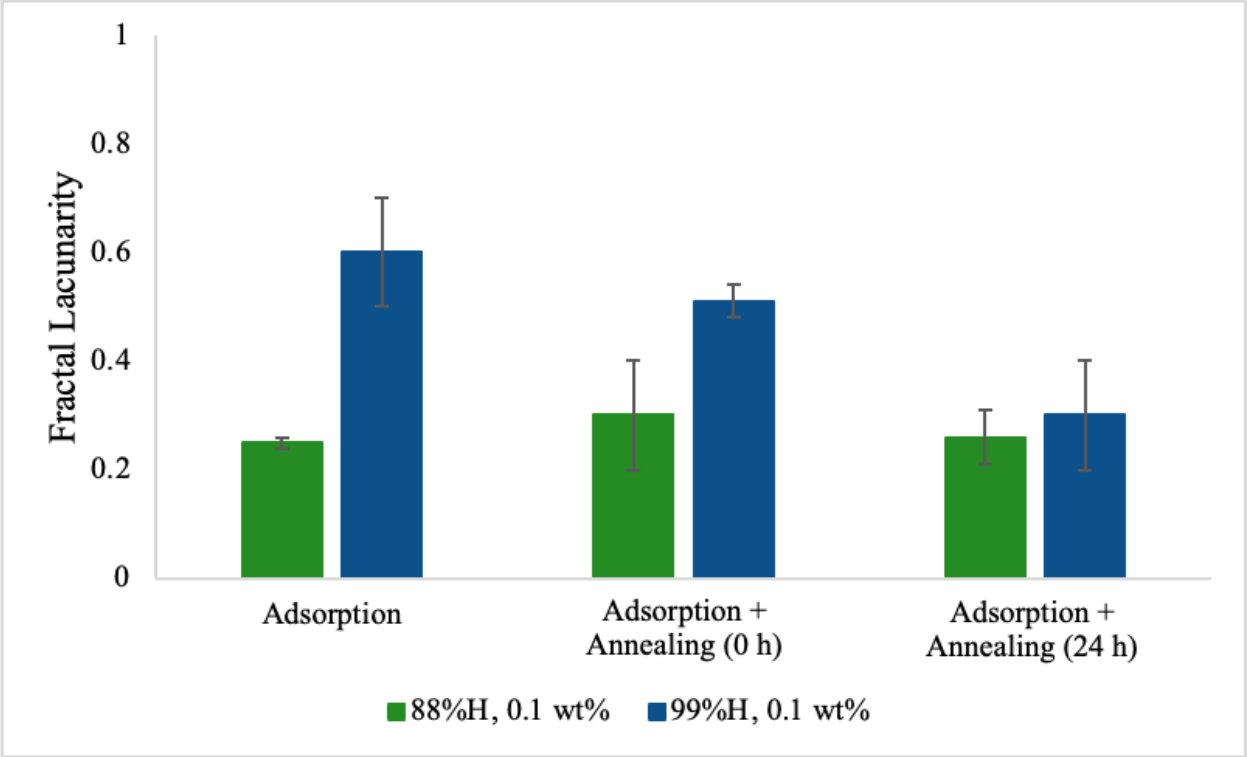

Figure 27. Fractal lacunarity L of PVOH-PDMS^{9k} films after static adsorption for 1 min and water annealing after 0 or 24 h.

3.4.2 Effect of % hydrolysis and [PVOH]

The morphologies of the adsorbed and immediately-annealed PVOH-PDMS^{49k} films were also analyzed. The % PVOH surface coverage increased slightly with the [PVOH] and the % hydrolysis (Figure 28). Generally, the % PVOH surface coverage was independent of treatment. While these results are opposite from those on PDMS^{9k} substrates (Figure 25), this suggests that PVOH$^{0.1\ wt\%}$-PDMS^{49k} films are more stable to immediate annealing than PVOH$^{0.1\ wt\%}$-PDMS^{9k} films due to a more significant loosely-bound h_1 PVOH layer on PDMS^{9k} substrates compared to PDMS^{49k}.

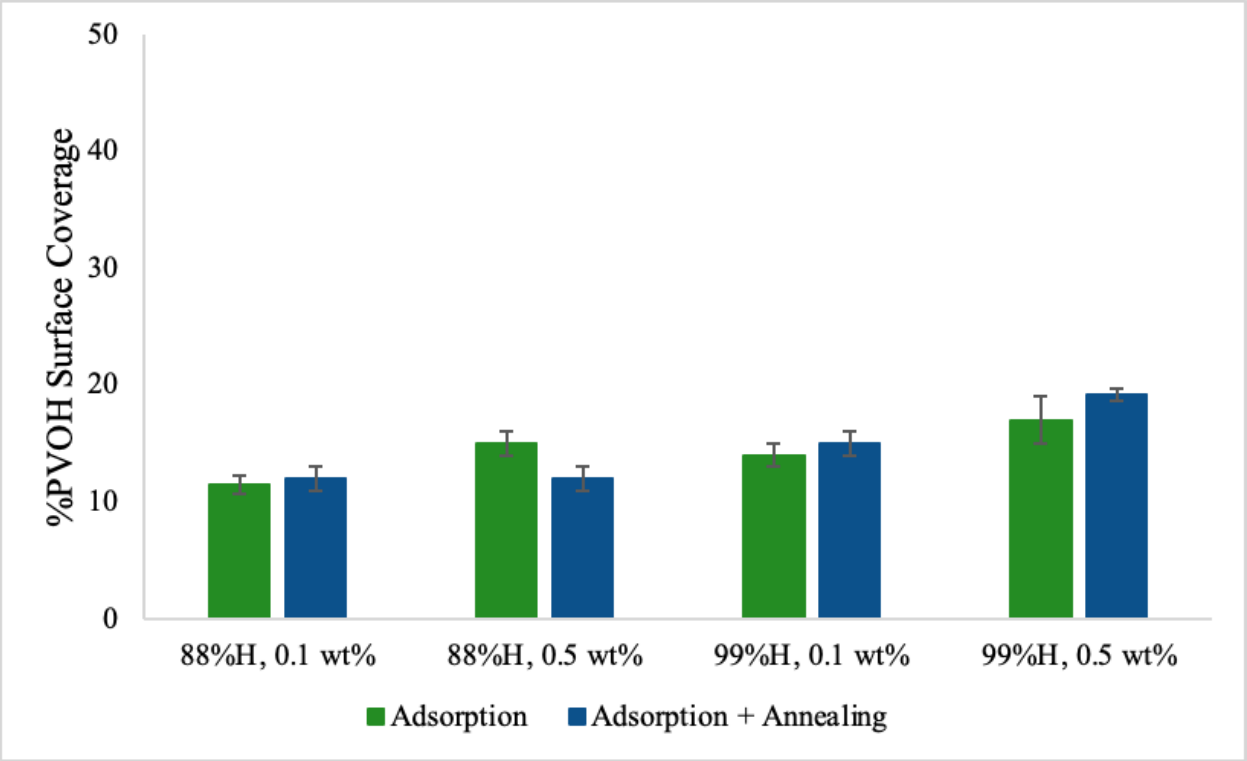

Figure 28. % PVOH surface coverage on PDMS^{49k} after static adsorption for 1 min and water annealing after 0 h.

The D values of the PVOH-PDMS^{49k} films generally appeared independent of treatment and [PVOH] (Figure 29). The PVOH$^{88\%H}$-PDMS^{49k} films had greater D values than the PVOH$^{99\%H}$-PDMS^{49k} films as a result of the greater morphological complexity (Table 7d).

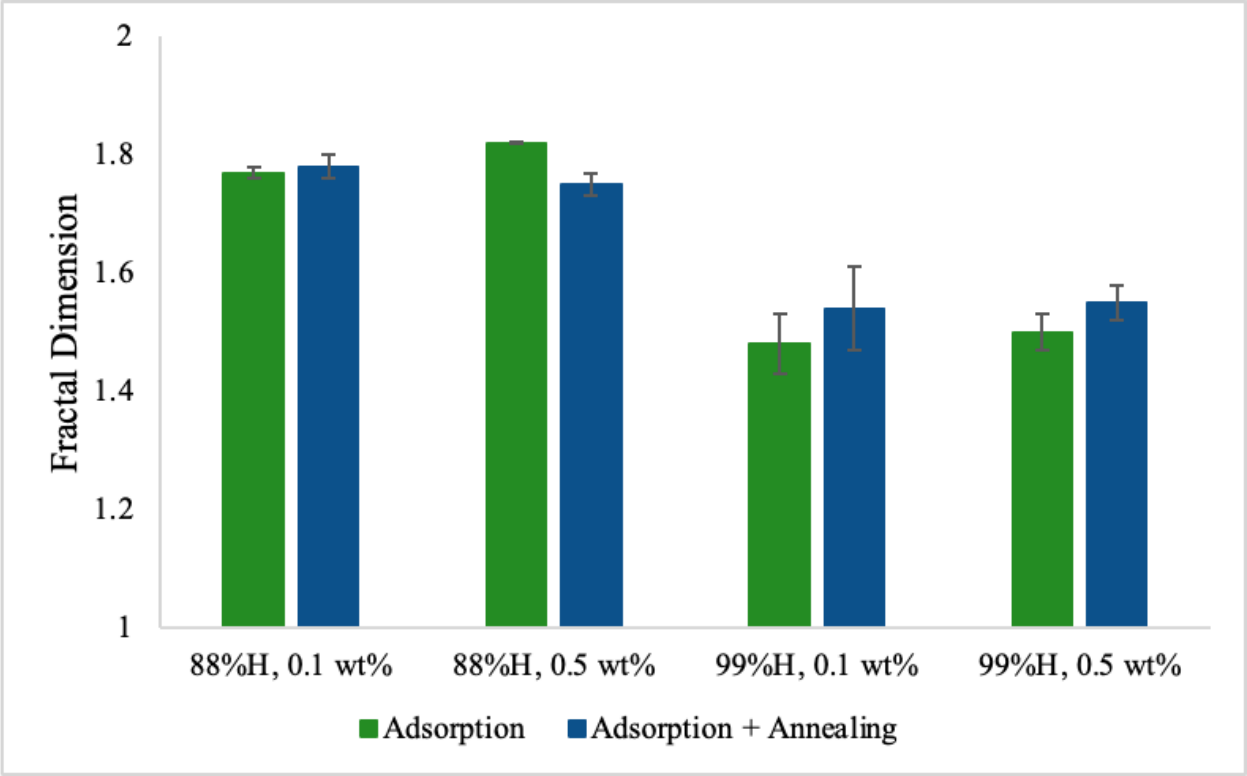

Figure 29. Fractal dimension D of PVOH-PDMS^{49k} films after static adsorption for 1 min and water annealing after 0 h.

The L values of the PVOH-PDMS^{49k} films also appeared generally independent of treatment and the [PVOH] and dependent on the % hydrolysis (Figure 30). There was a slight decrease in the L value of the adsorbed PVOH$^{88\%H,\ 0.5\ wt\%}$-PDMS^{49k} films compared to the adsorbed PVOH$^{88\%H,\ 0.1\ wt\%}$-PDMS^{49k} films, corresponding with a slight increase in the D value (Figure 29). These changes were also accompanied by decreased droplet size (Table 7d). These data suggest that morphological differences between the adsorbed PVOH$^{88\%H,\ 0.1\ wt\%}$-PDMS^{49k} and PVOH$^{88\%H,\ 0.5\ wt\%}$-PDMS^{49k} films were due to the higher [PVOH] providing a stronger driving force for adsorption. However, these small morphological differences were negligible following water annealing and polymer rearrangement.

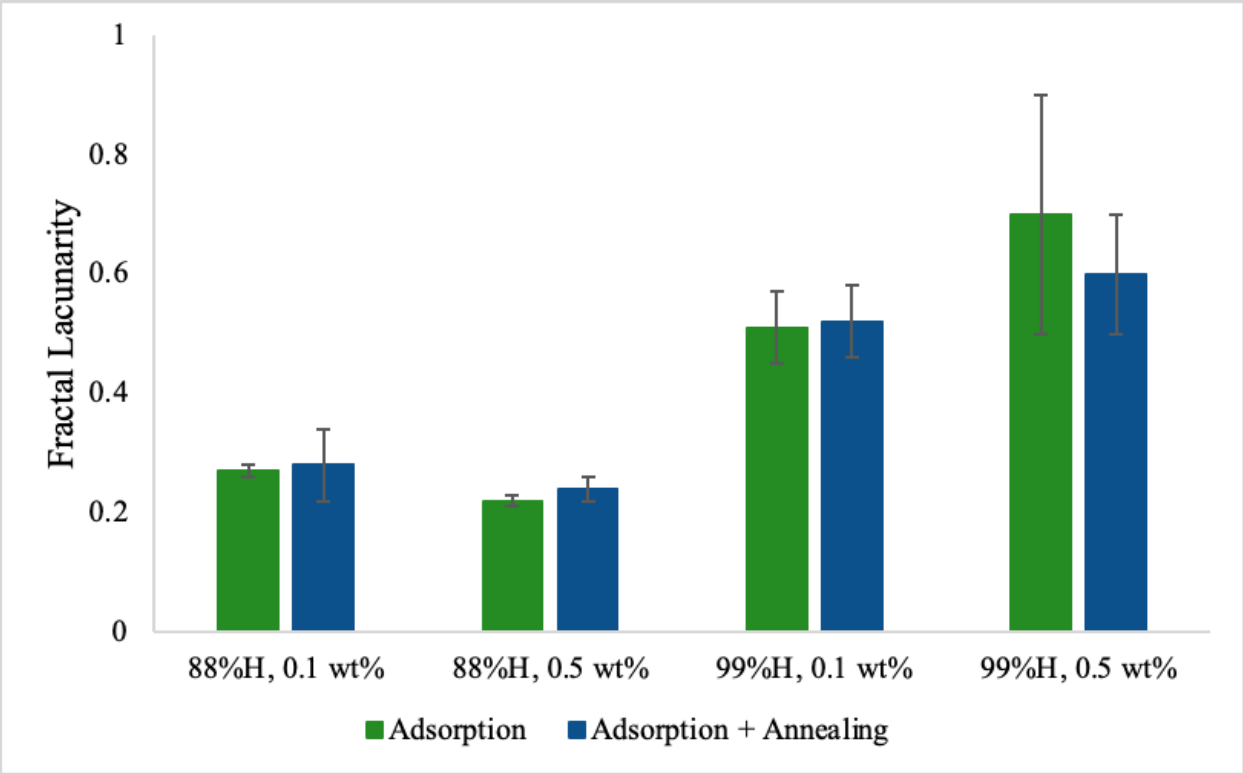

Figure 30. Fractal lacunarity L of PVOH-PDMS^{49k} films after static adsorption for 1 min and water annealing after 0 h.

3.5 Spin coating

3.5.1 PDMS^{9k} Substrate

The thicknesses and CAs of the spin-coated PVOH$^{88\%H,\ 0.1\ wt\%}$-PDMS^{9k} and PVOH$^{99\%H,\ 0.1\ wt\%}$-PDMS^{9k} films were independent of % hydrolysis and spin rate (Figures 31 and 32), indicating that the films contained extremely dewetted morphologies and no additional deposition during spin.

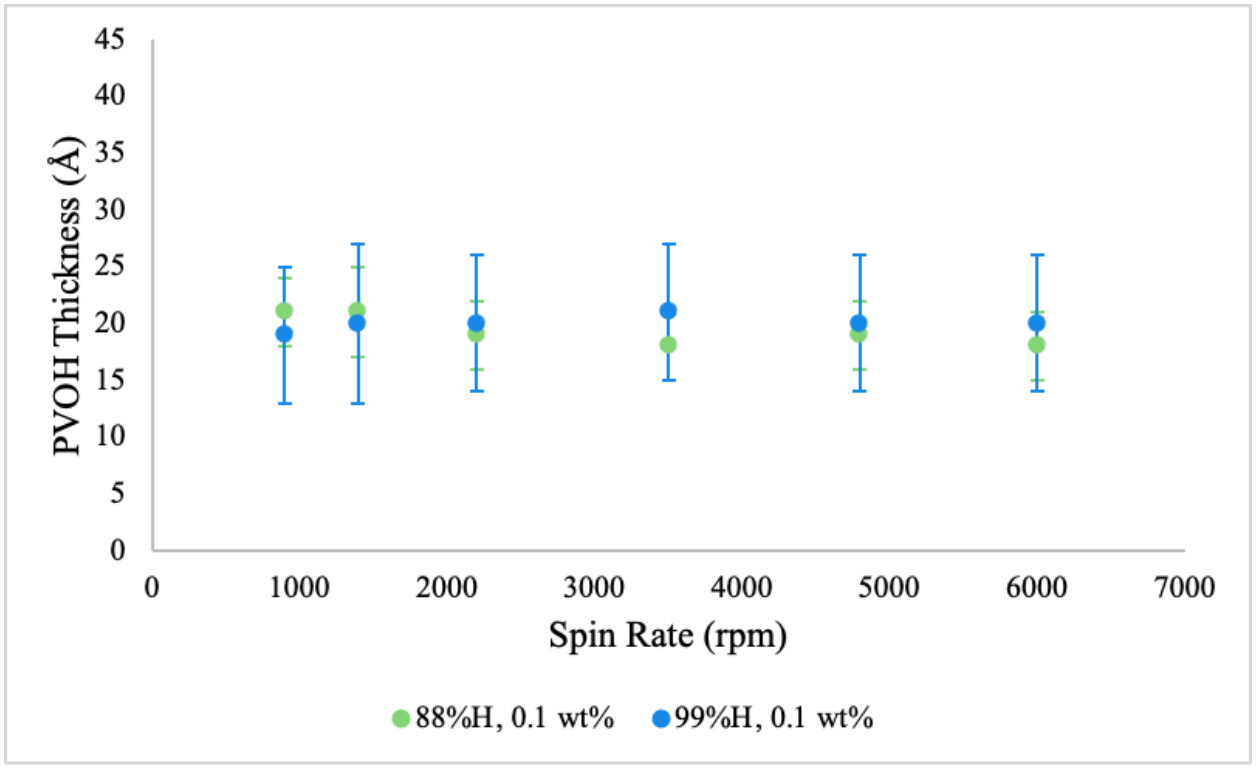

Figure 31. Thicknesses of PVOH-PDMS^{9k} films after spin coating.

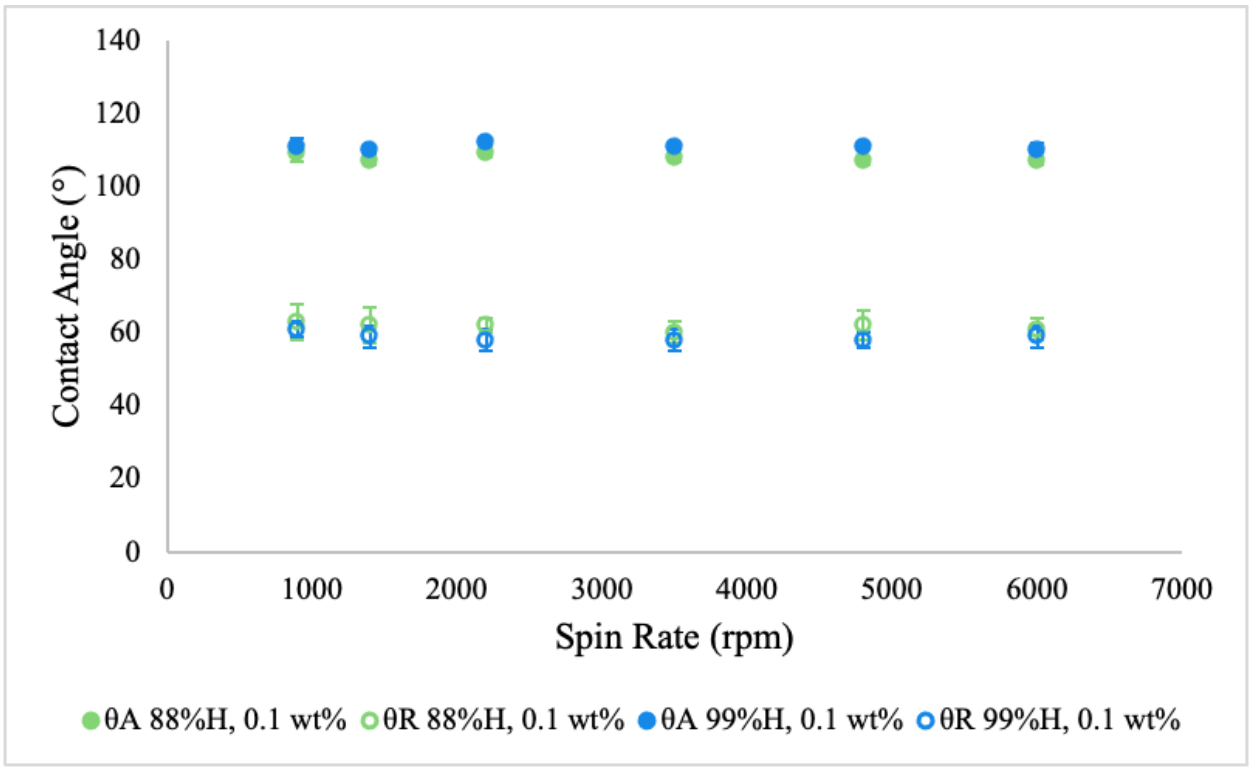

Figure 32. Contact angles of PVOH-PDMS^{9k} films after spin coating.

The optical images of the PVOH$^{0.1\ wt\%}$-PDMS^{9k} films prepared by spin coating at 900 rpm and 6000 rpm (Table 9) show extreme dewetting similar to the adsorbed PVOH$^{0.1\ wt\%}$-PDMS^{9k} films (Tables 7c). This result, combined with the independence of film thickness from spin rate, indicates that PVOH-PDMS^{9k} is an unstable system, which is consistent with previous postulations.[48] Additional optical images of the spin-coated PVOH$^{0.1\ wt\%}$-PDMS^{9k} films prepared at the intermediate spin rates are provided in Tables 16a and 16b in the Appendix.

The optical images of the spin-coated PVOH$^{0.1\ wt\%}$-PDMS^{9k} films show a small dependance of morphology on spin rate and location on sample, where the fractals at the center of the 6000 rpm films were more dense than at the edge of the 6000 rpm film (Table 9). This dependence of morphology on the location of the sample was not evident in the 900 rpm films since 900 rpm is the slowest spin rate, and the films are still slightly wet after spin coating. Drying takes place over a longer period after spin coating at 900 rpm, resulting in increased uniformity in morphology.

Table 9. Optical images of PVOH-PDMS^{9k} films prepared by spin coating (500× magnification).

Spin rate (rpm)	Location on sample	PVOH$^{88\%H,\ 0.1\ wt\%}$	PVOH$^{99\%H,\ 0.1\ wt\%}$
900	Center	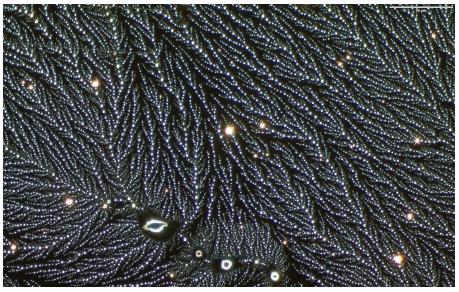	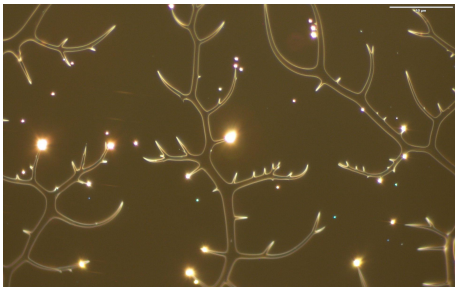
	Edge	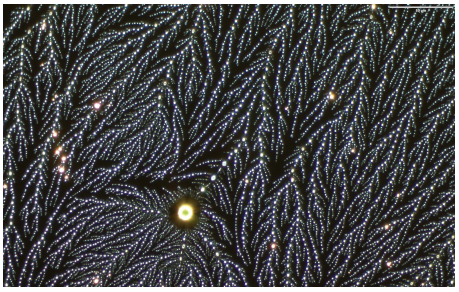	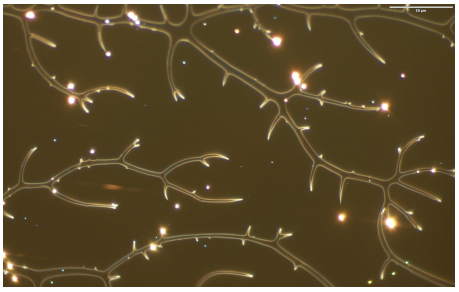
6000	Center	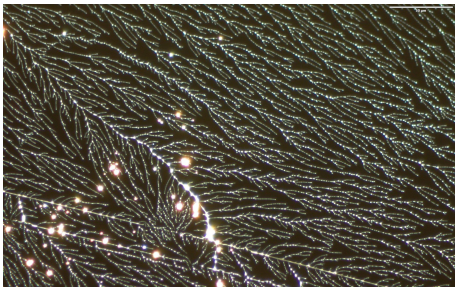	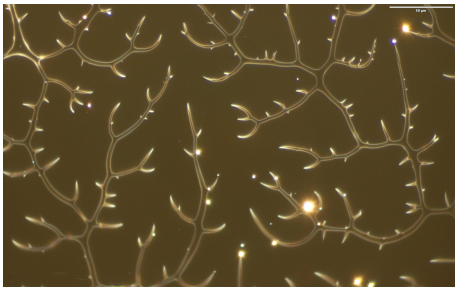
	Edge		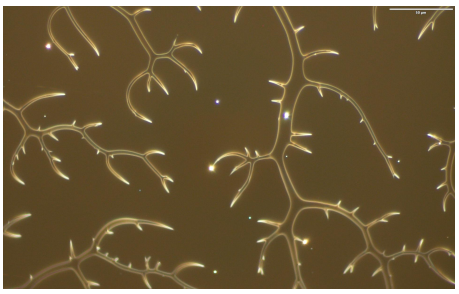

3.5.2 PDMS^{49k} Substrate

The thicknesses of the spin-coated PVOH$^{88\%H,\ 0.1\ wt\%}$-PDMS^{49k} and PVOH$^{99\%H,\ 0.1\ wt\%}$-PDMS^{49k} films were also independent of % hydrolysis and spin rate (Figure 33), consistent with

previous observations that the PVOH-PDMS^{49k} system is unstable.[48] The high standard deviations in thickness can be attributed to the extreme dewetting and more numerous replicates compared to the spin-coated PVOH-PDMS^{9k} experiments. The thicknesses of the spin-coated PVOH$^{0.1\ wt\%}$-PDMS^{9k} (Figure 31) and PVOH$^{0.1\ wt\%}$-PDMS^{49k} films (Figure 33) were all approximately 20 Å, which is within standard deviation of the adsorbed and delayed-annealed PVOH$^{99\%H,\ 0.1\ wt\%}$-PDMS^{9k} films, the adsorbed and immediately-annealed PVOH$^{88\%H,\ 0.1\ wt\%}$-PDMS^{9k} films, and the adsorbed and the immediately-annealed PVOH$^{0.1\ wt\%}$-PDMS^{49k} films (Figures 21 and 23). The thickness data suggest that the spin-coated PVOH$^{88\%H}$-PDMS^{9k} films only contain a tightly-bound h_1 layer, while the spin-coated PVOH$^{99\%H}$-PDMS^{9k} films contain a tightly-bound and a loosely-bound h_1 layer. On the other hand, the thickness data suggest that all PVOH$^{0.1\ wt\%}$-PDMS^{49k} films only contain a tightly-bound h_1 layer.

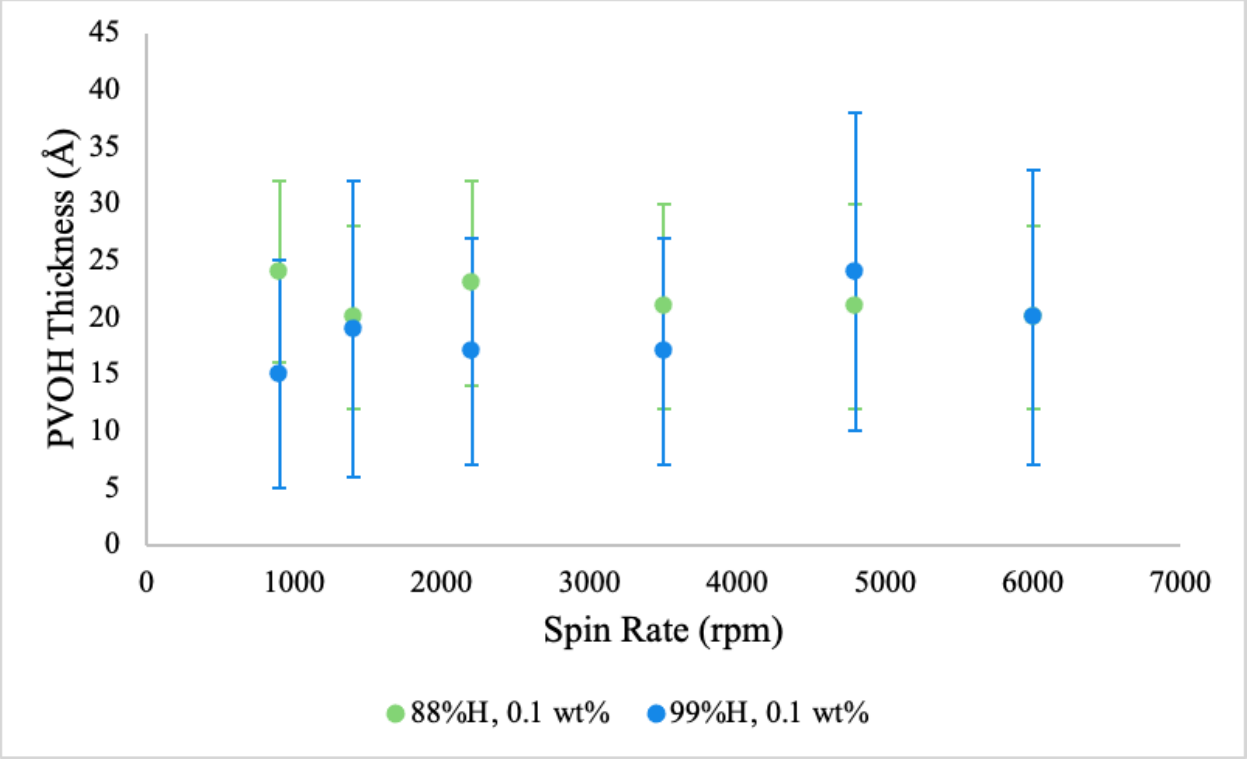

Figure 33. Thicknesses of PVOH-PDMS^{49k} films after spin coating.

The CAs of the spin-coated PVOH$^{0.1\ wt\%}$-PDMS^{49k} films were also fairly independent of spin rate, but the CAs of the PVOH$^{99\%H,\ 0.1\ wt\%}$-PDMS^{49k} films were slightly greater than the CAs of the PVOH$^{88\%H,\ 0.1\ wt\%}$-PDMS^{49k} films (Figure 34). This result could be due to a greater extent of dewetting in the PVOH$^{99\%H,\ 0.1\ wt\%}$-PDMS^{49k} films compared to PVOH$^{88\%H,\ 0.1\ wt\%}$-PDMS^{49k}, leaving more of the hydrophobic substrate exposed.

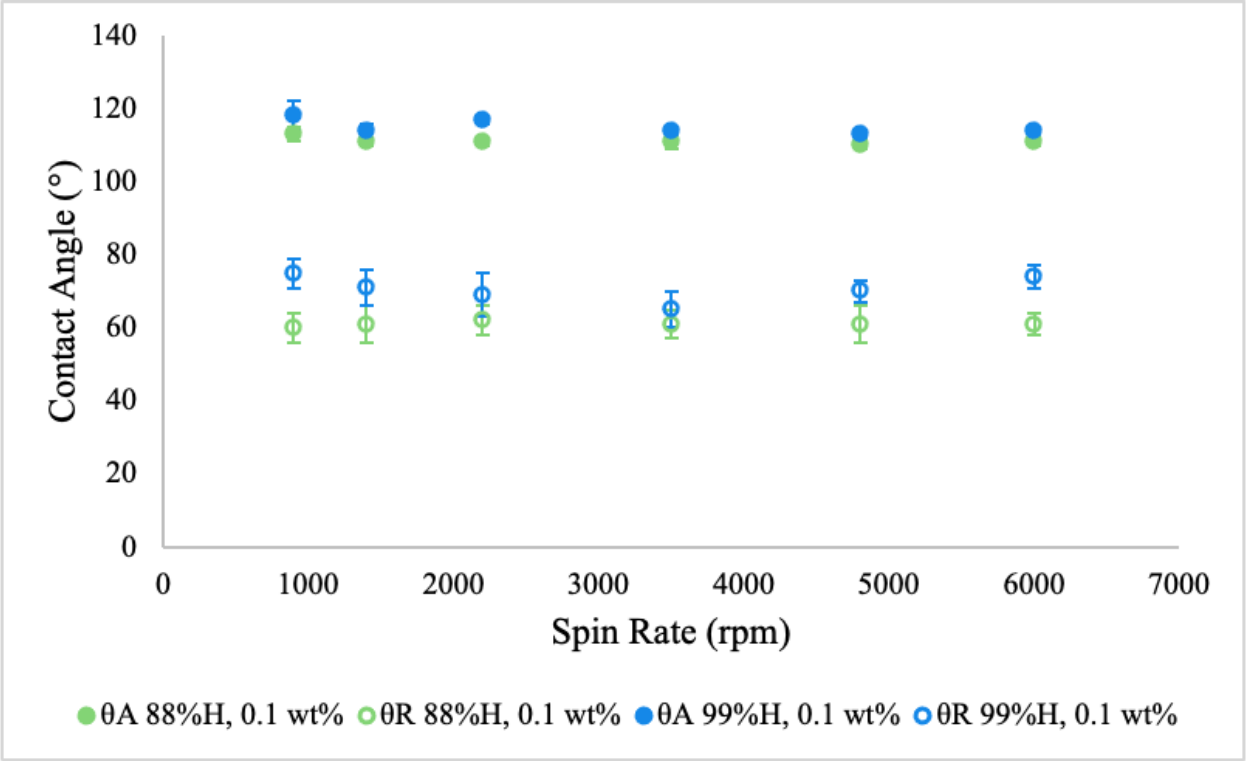

Figure 34. Contact angles of PVOH-PDMS^{49k} films after spin coating.

The AFM images also show nanoscopic morphological differences in the spin-coated PVOH$^{0.1\ wt\%}$-PDMS^{49k} films that depended on % hydrolysis and location on sample (Tables 10a and 10b). On the nanoscopic scale, the PVOH$^{88\%H,\ 0.1\ wt\%}$ films contained thin branches between droplets, and the branch width seemed to decrease toward the edge of the sample (Table 10a), most likely due to the greater centrifugal force. The PVOH$^{99\%H,\ 0.1\ wt\%}$ films contained thicker branches and did not appear to contain droplets (Table 10b). The PVOH$^{99\%H,\ 0.1\ wt\%}$ fractal width also appears to decrease toward the edge of the sample, but more images are necessary to

confirm this result. Lastly, the height of the $PVOH^{99\%H,\ 0.1\ wt\%}$ fractals was less than half of the height of the $PVOH^{88\%H,\ 0.1\ wt\%}$ droplets, indicating that the $PVOH^{88\%H}$ polymers possess a stronger tendency to aggregate vertically compared to the $PVOH^{99\%H}$ polymers. This significant difference in morphologies can be attributed to the different amounts of crystallization, where the decreased degree of $PVOH^{88\%H,\ 0.1\ wt\%}$ crystallization is just sufficient to resist Rayleigh instability and decaying into droplet morphology.

Table 10a. AFM images and section analyses of PVOH$^{88\%H,\ 0.1\ wt\%}$-PDMS^{49k} films prepared by spin coating (AFM image size: 10 µm × 10 µm; height scale: 250 nm).

Spin rate (rpm)	Location on sample	AFM image	Section analysis
900	Center	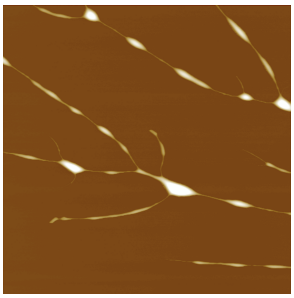	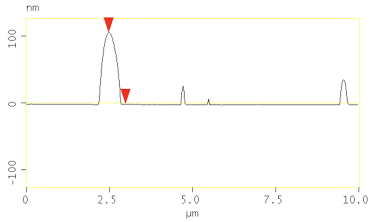
	Edge	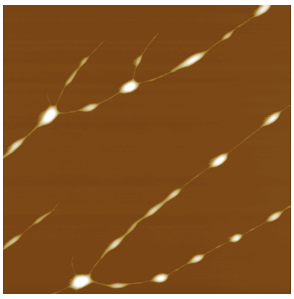	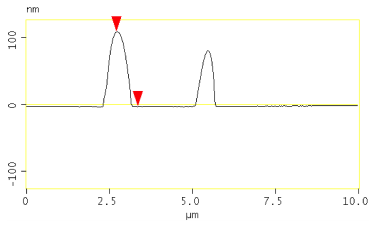
4800	Center	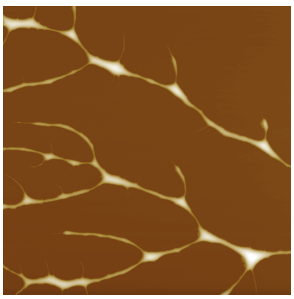	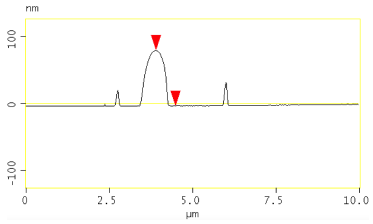
	Edge	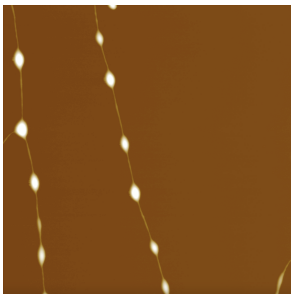	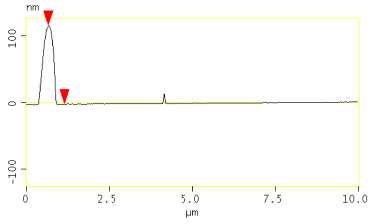

Table 10b. AFM images and section analyses of PVOH$^{99\%H,\ 0.1\ wt\%}$-PDMS^{49k} films prepared by spin coating (height scale: 250 nm).

Spin rate (rpm)	Location on sample	AFM image	Section analysis
900	Edge	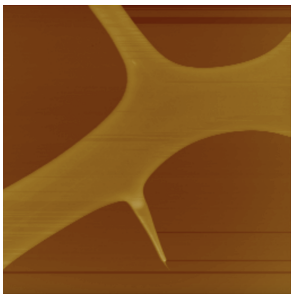 (50 μm × 50 μm)	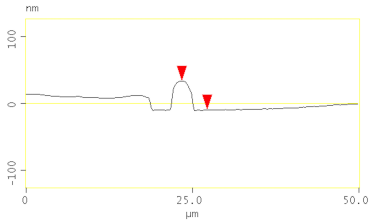
6000	Center	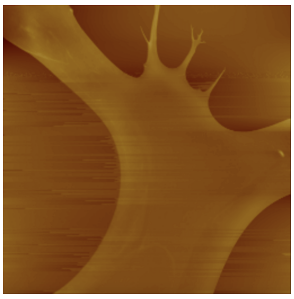 (20 μm × 20 μm)	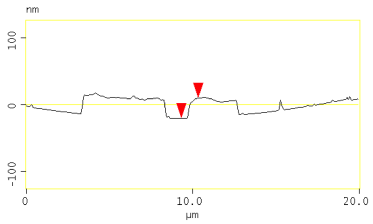
	Edge	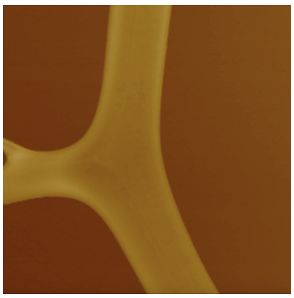 (20 μm × 20 μm)	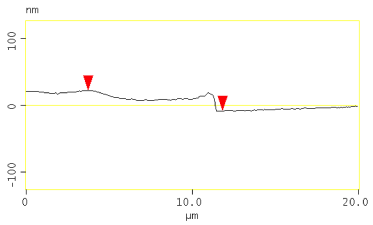

The optical images of the spin-coated PVOH$^{0.1\ wt\%}$-PDMS^{49k} films demonstrate a strong dependence of microscopic morphology on the % hydrolysis only (Table 11). Unlike the spin-coated PVOH$^{0.1\ wt\%}$-PDMS^{9k} films (Table 9), there were no perceivable differences in morphology between the different spin rates and locations on samples for the PVOH$^{0.1\ wt\%}$-PDMS^{49k} films. This can be explained by the extreme substrate mobility of PDMS^{49k} resulting in spin-coated morphologies closer to the equilibrium morphology. Additional optical

images of the spin-coated PVOH$^{0.1\ wt\%}$-PDMS^{49k} films prepared at the intermediate spin rates are provided in Tables 17a and 17b in the Appendix.

Table 11. Optical images of PVOH-PDMS^{49k} films prepared by spin coating (500× magnification).

Spin rate (rpm)	Location on sample	PVOH$^{88\%H,\ 0.1\ wt\%}$	PVOH$^{99\%H,\ 0.1\ wt\%}$
900	Center	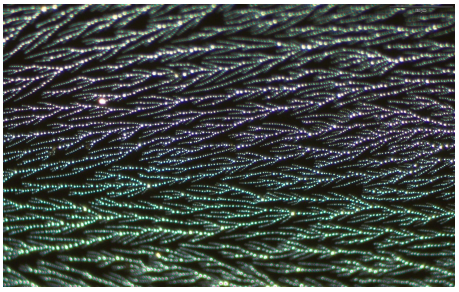	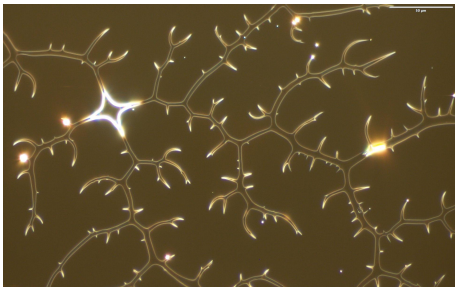
	Edge	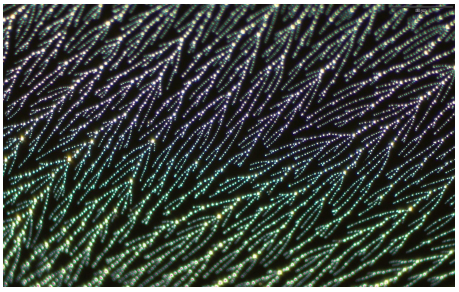	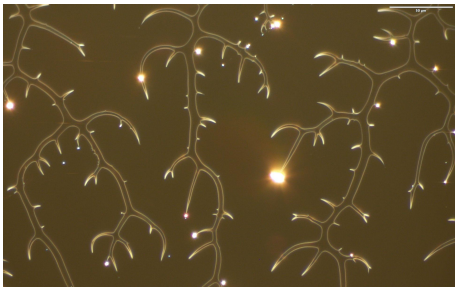
6000	Center	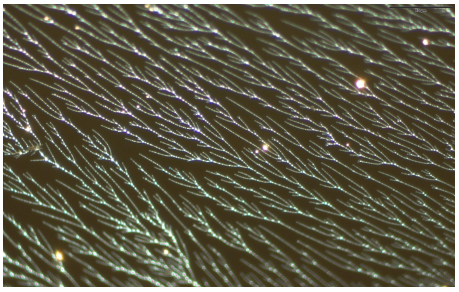	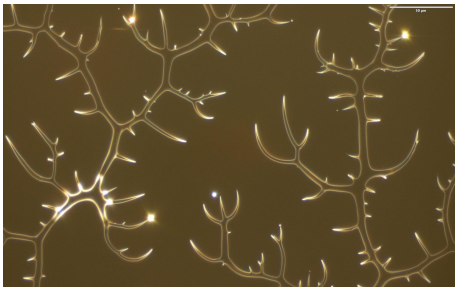
	Edge	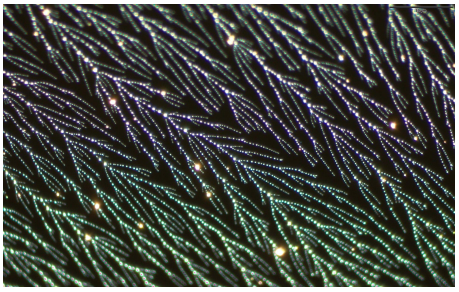	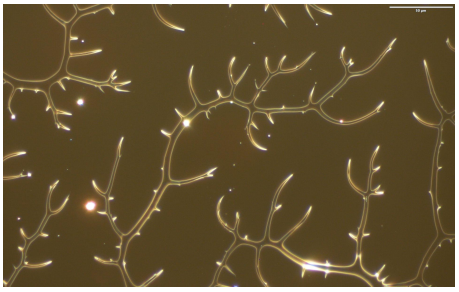

The global optical images of the spin-coated $PVOH^{0.1\ wt\%}$-$PDMS^{49k}$ films show the footprints of the initial droplets and the PVOH solution exit lines for both $PVOH^{88\%H,\ 0.1\ wt\%}$ and $PVOH^{99\%H,\ 0.1\ wt\%}$ (Tables 12a and 12b). PVOH aggregates are evident in the exit lines, and each image contains multiple exit lines. Generally, as the spin rate increases, the number of exit lines increases, and the width of the lines decreases due to the increased acceleration during spin up. Therefore, it is expected that, as the spin rate increases, morphological heterogeneity will also increase, especially at the edges of the samples. Indeed, it is evident that the "centers" and "edges" of the samples vary in morphology, as well as the exit lines and the rest of the films. Additional global optical images of the spin-coated $PVOH^{0.1\ wt\%}$-$PDMS^{49k}$ films prepared at the intermediate spin rates are provided in Tables 18a and 18b in the Appendix. The global morphology varies between samples of the same PVOH polymer and spin rate, making it difficult to reproduce global morphology accurately, resulting in high variance in thickness and CA.

Table 12a. Global optical images of PVOH$^{88\%H,\ 0.1\ wt\%}$-PDMS^{49k} films prepared by spin coating.

900 rpm	6000 rpm
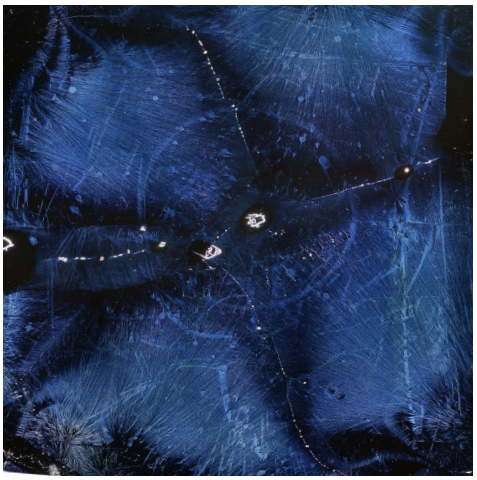 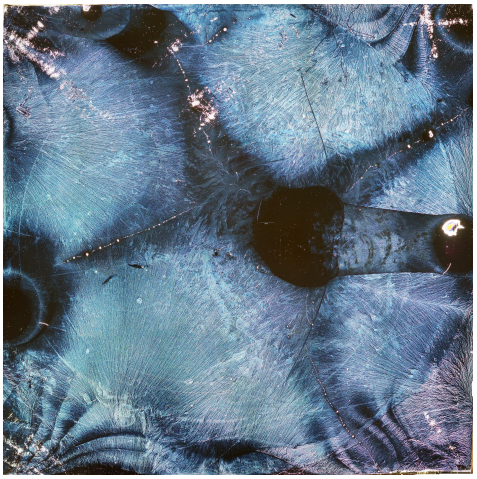	

Table 12b. Global optical images of PVOH$^{99\%H,\ 0.1\ wt\%}$-PDMS^{49k} films prepared by spin coating.

900 rpm	6000 rpm
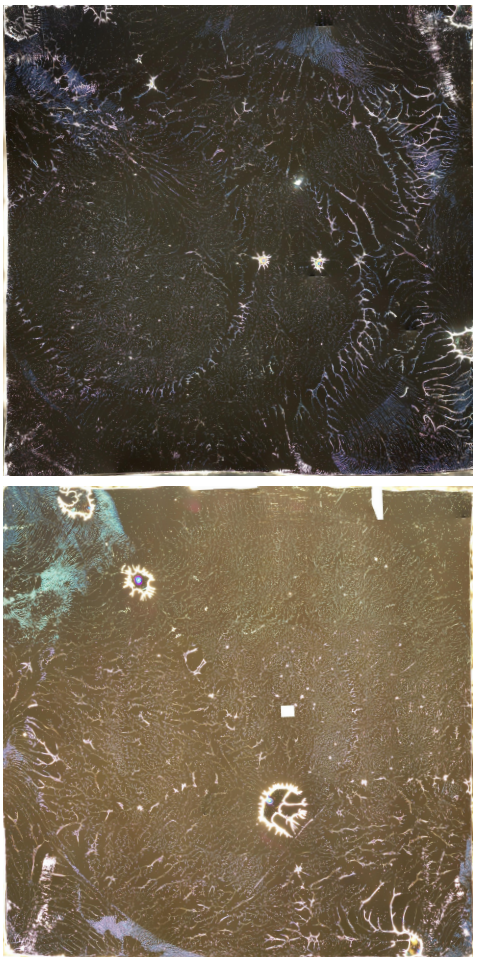	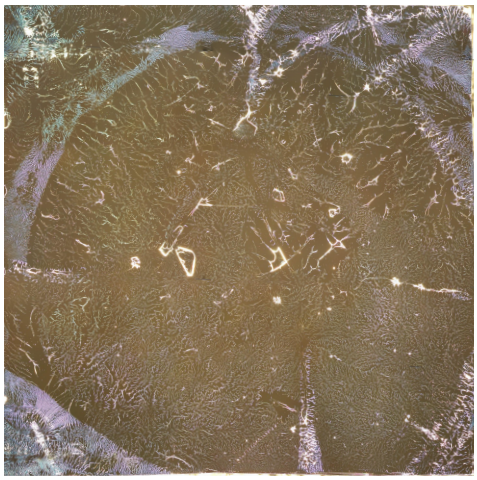

3.6 Water annealing following spin coating

3.6.1 PDMS^{9k} Substrate

The spin-coated PVOH$^{0.1\ wt\%}$-PDMS^{9k} films were annealed in water 0 h or 24 h after spin coating, and the film thicknesses were measured (Figures 35 and 36). For both % hydrolysis, the film thickness was largely independent of spin rate, as seen in section 3.5. The annealed PVOH$^{88\%H,\ 0.1\ wt\%}$-PDMS^{9k} film thickness (Figure 35) was independent of the time before annealing, but the annealed PVOH$^{99\%H,\ 0.1\ wt\%}$-PDMS^{9k} film thickness (Figure 36) had a slight dependence on the time before annealing, where the PVOH$^{99\%H,\ 0.1\ wt\%}$-PDMS^{9k} films annealed 24

h after spin coating were slightly thicker than those annealed 0 h after spin coating. The average annealed PVOH$^{88\%H,\ 0.1\ wt\%}$-PDMS^{9k} film thickness was less than the average spin-coated PVOH$^{88\%H,\ 0.1\ wt\%}$-PDMS^{9k} film thickness (Figure 31), regardless of the time before annealing. On the other hand, the average delayed-annealed PVOH$^{99\%H,\ 0.1\ wt\%}$-PDMS^{9k} film thickness was comparable to the average spin-coated PVOH$^{99\%H,\ 0.1\ wt\%}$-PDMS^{9k} film thickness (Figure 31). These results indicate that the spin-coated PVOH$^{88\%H,\ 0.1\ wt\%}$-PDMS^{9k} films contained some tightly-bound and loosely-bound h_1, and water annealing resulted in the removal of the loosely-bound h_1. The spin-coated PVOH$^{99\%H,\ 0.1\ wt\%}$-PDMS^{9k} films also contained some tightly-bound and loosely-bound h_1, and the loosely-bound h_1 was only unstable to immediate water annealing. These results are consistent with section 3.3.2, and can be attributed to the more extensive crystallization of PVOH$^{99\%H}$ resulting in greater stability.

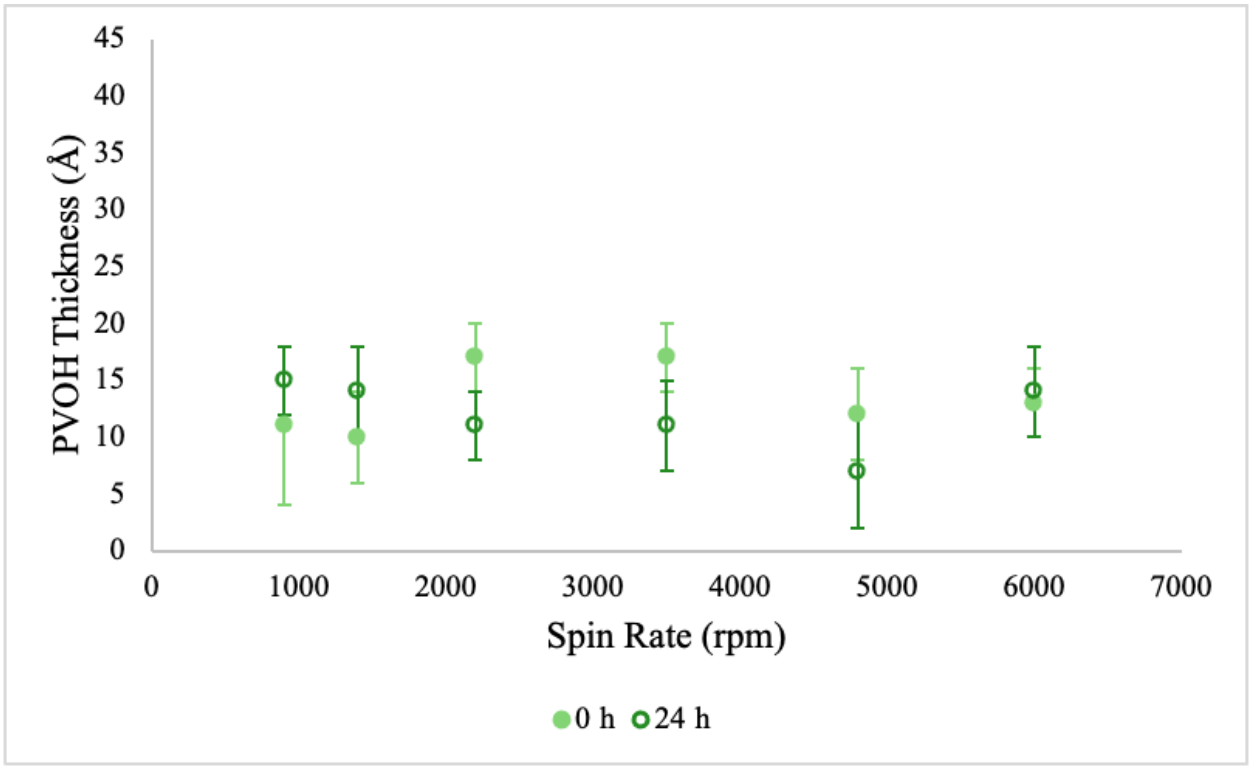

Figure 35. Thicknesses of PVOH$^{88\%H,\ 0.1\ wt\%}$-PDMS^{9k} films after spin coating and water annealing after 0 or 24 h.

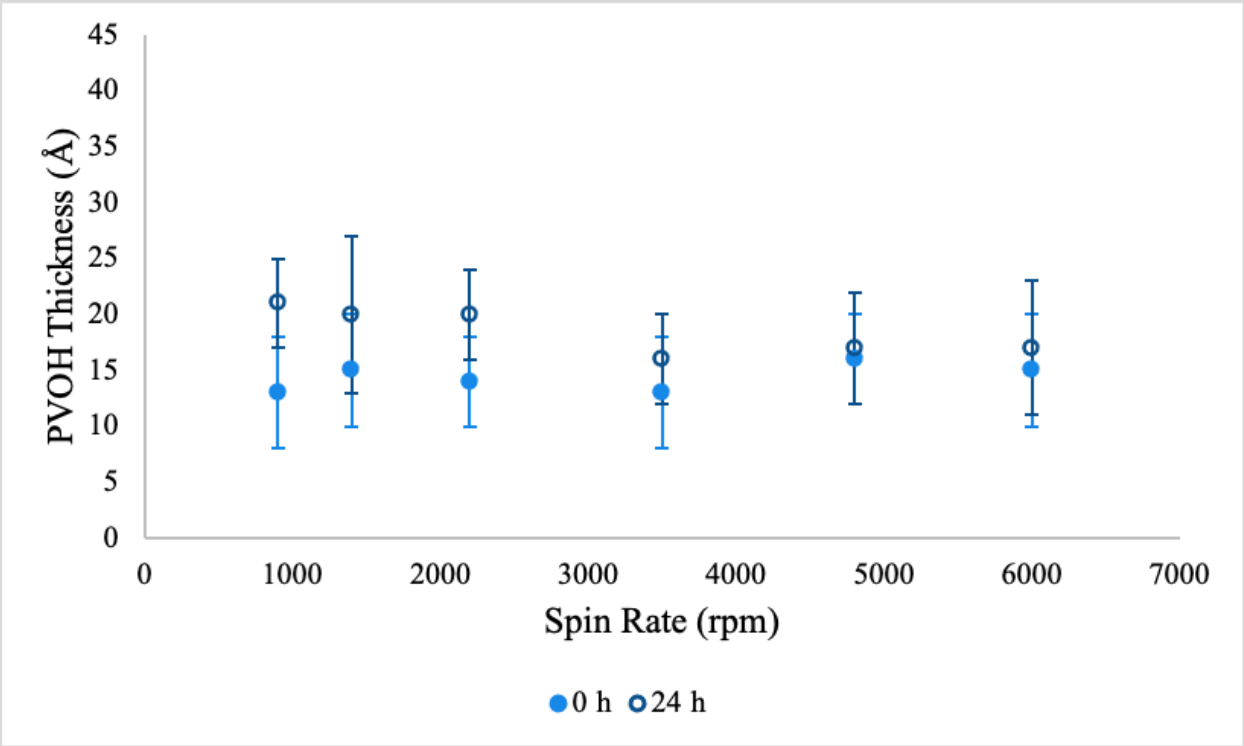

Figure 36. Thicknesses of PVOH$^{99\%H,\ 0.1\ wt\%}$-PDMS^{9k} films after spin coating and water annealing after 0 or 24 h.

The contact angles of the annealed PVOH$^{0.1\ wt\%}$-PDMS^{9k} films were equal to the spin-coated PVOH$^{0.1\ wt\%}$-PDMS^{9k} films (Figure 32), and were independent of the % hydrolysis, the spin rate, and the time before annealing (Appendix; Figures 52 and 53).

The optical images after spin coating and water annealing PVOH$^{0.1\ wt\%}$ on PDMS^{9k} show a strong dependence of microscopic morphology on the % hydrolysis and some dependence on the spin rate and the time before annealing (Tables 13a and 13b). An increase in heterogeneity in fractal size due to film rearrangement was apparent after water annealing, compared to before water annealing (Table 9). Contrary to the spin-coated film thicknesses before and after water annealing (Figures 31 and 36), the PVOH$^{99\%H,\ 0.1\ wt\%}$-PDMS^{9k} fractal heterogeneity appeared to increase with the time before annealing. While the thickness was more consistent with the spin-coated thickness, the morphology was less consistent after delayed-annealing compared to immediate-annealing. This is despite the optical images of the delayed-annealed films being

taken on the same sample and in the same location as before annealing, while the optical images of the immediately-annealed films were taken on different samples as before annealing. These results suggest that the higher plasticity of the freshly-spin-coated films allows for greater rearrangement and progress toward the equilibrium morphology. This indicates that the immediately-annealed film morphology is closer to the equilibrium morphology than the delayed-annealed morphology. Greater morphological differences between the spin-coated, immediate-annealed, and delayed-annealed films were apparent after spin coating at 6000 rpm compared to 900 rpm, most likely due to the faster drying at 6000 rpm, which amplifies the effects of kinetic entrapment.

Table 13a. Optical images of PVOH-PDMS^{9k} films after spin coating at 900 rpm and water annealing after 0 or 24 h (500× magnification).

Spin rate (rpm)	Location on sample	Time before annealing (h)	PVOH$^{88\%H,\ 0.1\ wt\%}$	PVOH$^{99\%H,\ 0.1\ wt\%}$
900	Center	0	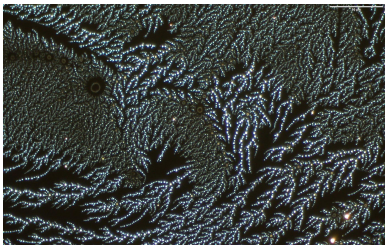	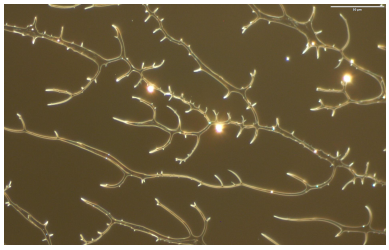
	Edge	0	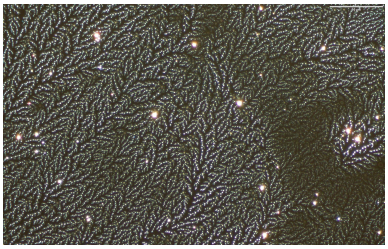	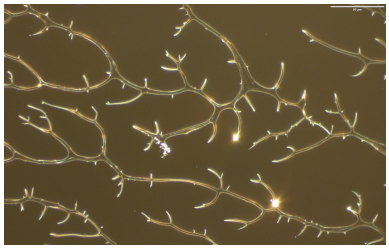
900	Center	24	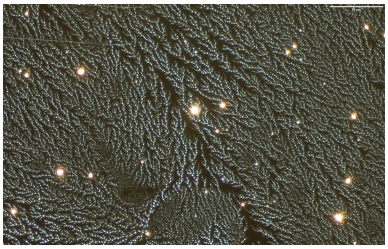	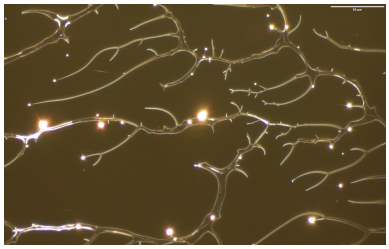
	Edge	24	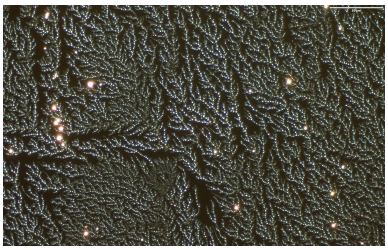	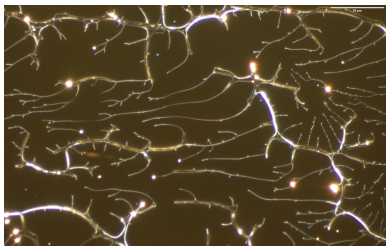

Table 13b. Optical images of PVOH-PDMS^{9k} films after spin coating at 6000 rpm and water annealing after 0 or 24 h (500× magnification).

Spin rate (rpm)	Location on sample	Time before annealing (h)	PVOH$^{88\%H,\ 0.1\ wt\%}$	PVOH$^{99\%H,\ 0.1\ wt\%}$
6000	Center	0	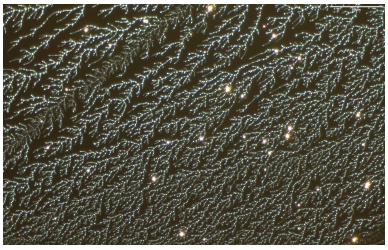	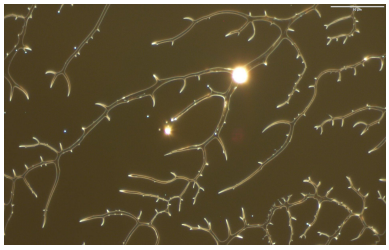
	Edge	0	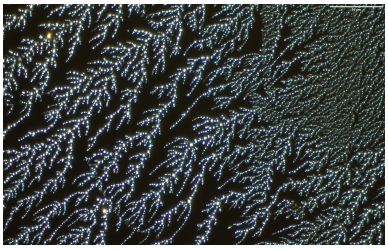	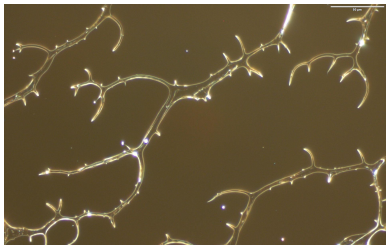
6000	Center	24	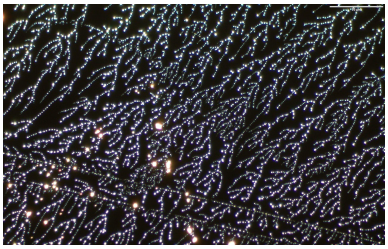	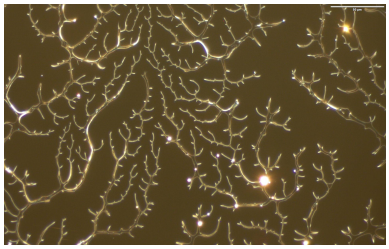
	Edge	24	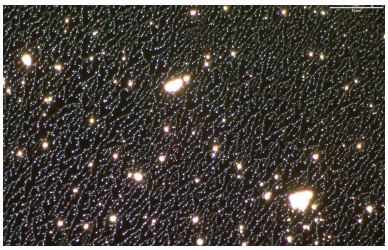	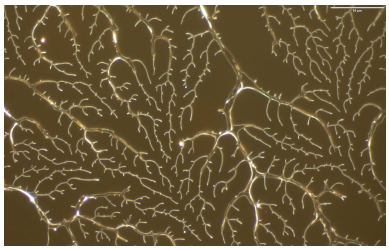

3.6.2 PDMS^{49k} Substrate

The spin-coated PVOH$^{0.1\ wt\%}$-PDMS^{49k} films were also annealed in water 0 h or 24 h after spin coating, and the film thicknesses were measured (Figures 37 and 38). The annealed

PVOH$^{0.1\ wt\%}$-PDMS^{49k} film thickness was largely independent of the spin rate, the % hydrolysis, and the time before annealing. These results differed slightly from those on PDMS^{9k} (Figures 35 and 36), and can be attributed to the high degree of mobility of the PDMS^{49k} substrate. Generally, the PVOH film thickness on PDMS^{49k} is consistent, regardless of the % hydrolysis or treatment, and this can be partially attributed to the high standard deviations in thickness arising from the extreme dewetting morphologies.

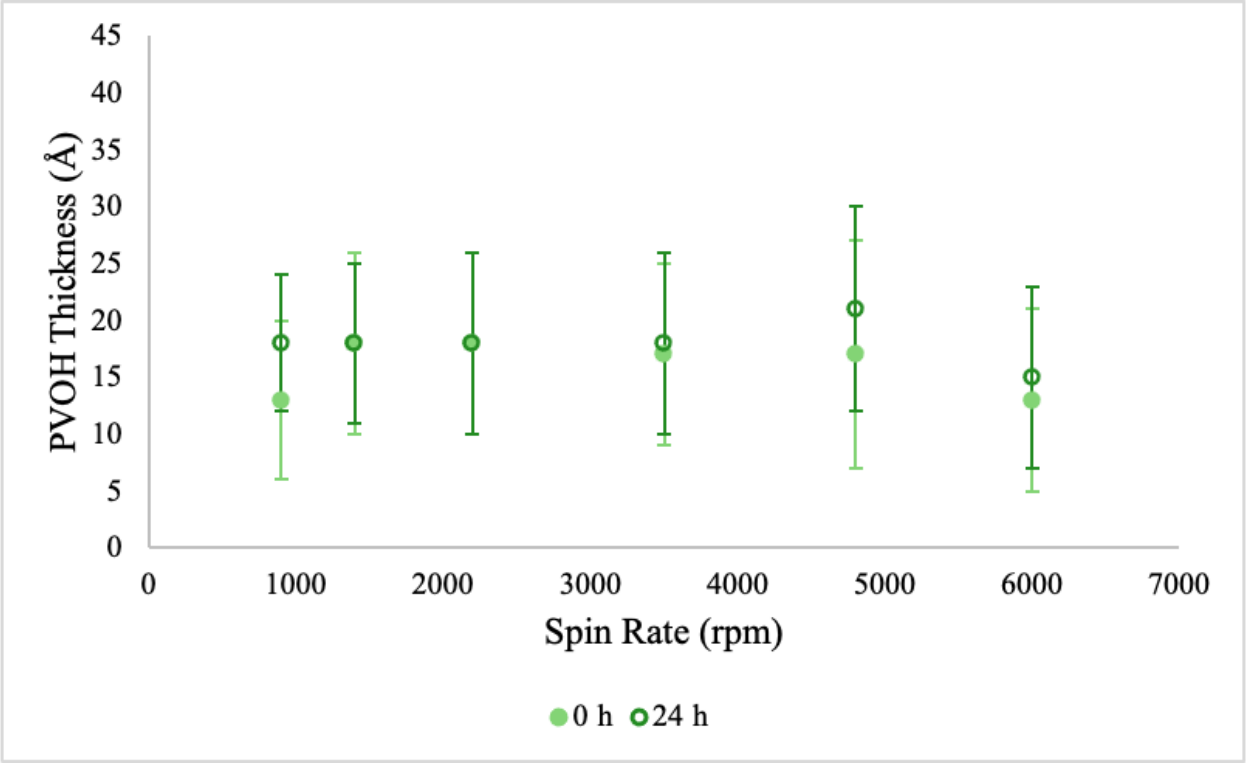

Figure 37. Thicknesses of PVOH$^{88\%H,\ 0.1\ wt\%}$-PDMS^{49k} films after spin coating and water annealing after 0 or 24 h.

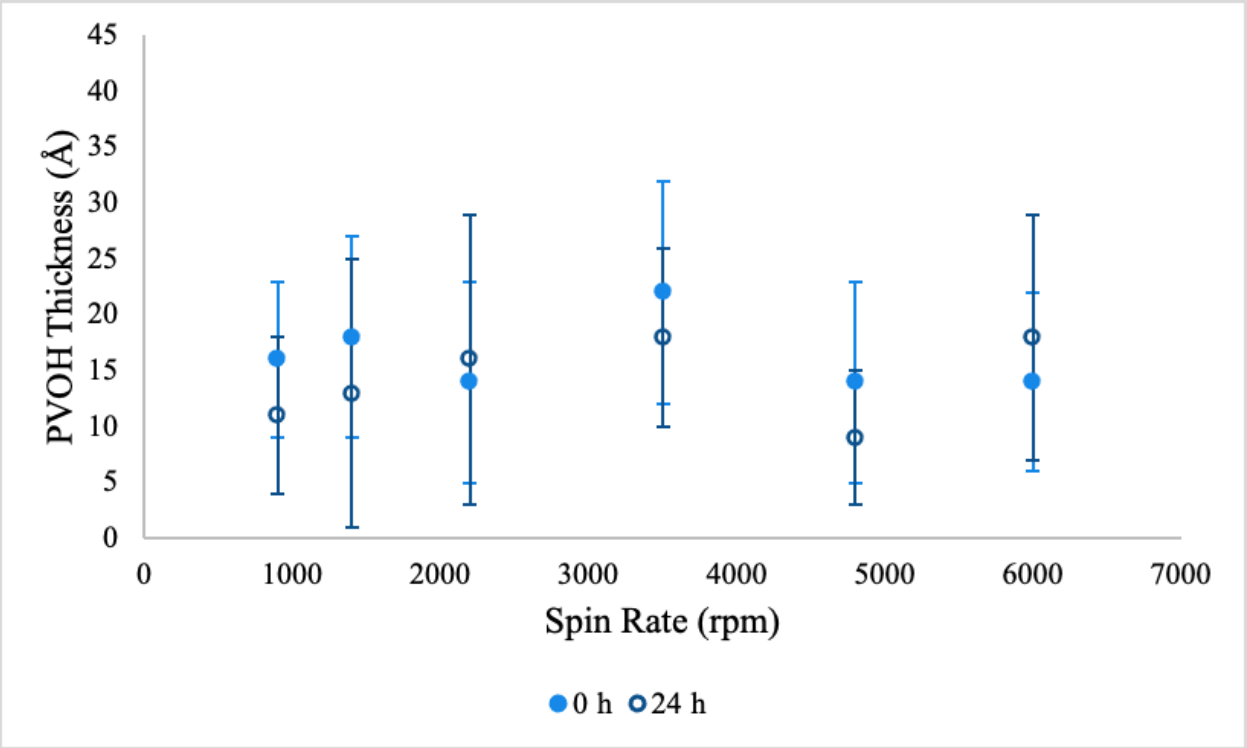

Figure 38. Thicknesses of PVOH$^{99\%H,\ 0.1\ wt\%}$-PDMS^{49k} films after spin coating and water annealing after 0 or 24 h.

The contact angles of the annealed PVOH$^{0.1\ wt\%}$-PDMS^{49k} films were equal to the spin-coated PVOH$^{0.1\ wt\%}$-PDMS^{49k} films (Figure 34), and were independent of the % hydrolysis, the spin rate, and the time before annealing (Appendix; Figures 54 and 55).

The optical images after spin coating and water annealing PVOH$^{0.1\ wt\%}$ on PDMS^{49k} show a strong dependence of microscopic morphology on the % hydrolysis and some dependence on the time before annealing (Tables 14a and 14b). The size of the PVOH$^{88\%H,\ 0.1\ wt\%}$-PDMS^{49k} fractals decreased significantly after water annealing, regardless of the time before annealing and the spin rate. Aggregation and film rearrangement were also observed in the PVOH$^{99\%H,\ 0.1\ wt\%}$-PDMS^{49k} films after water annealing. The different PVOH$^{99\%H,\ 0.1\ wt\%}$-PDMS^{49k} fractal sizes after immediate-annealing and delayed-annealing can be attributed to variance between different batches.

Table 14a. Optical images of PVOH-PDMS^{49k} films after spin coating at 900 rpm and water annealing after 0 or 24 h (500× magnification).

Spin rate (rpm)	Location on sample	Time before annealing (h)	PVOH$^{88\%H,\ 0.1\ wt\%}$	PVOH$^{99\%H,\ 0.1\ wt\%}$
900	Center	0	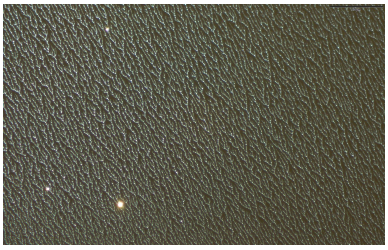	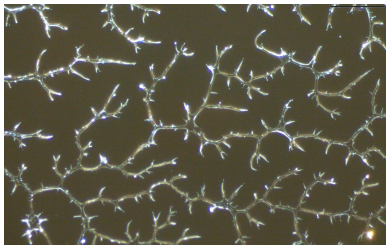
	Edge	0	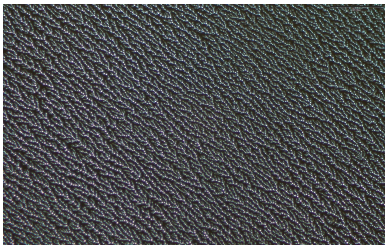	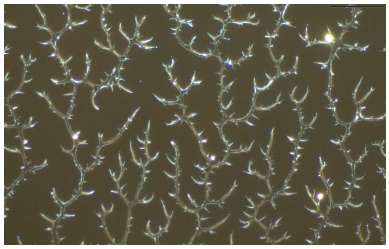
900	Center	24	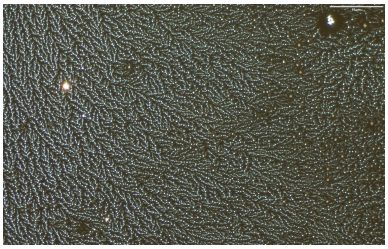	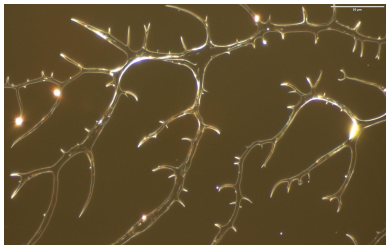
	Edge	24	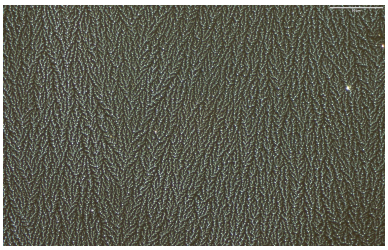	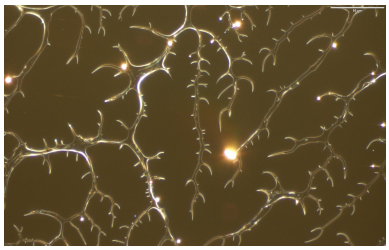

Table 14b. Optical images of PVOH-PDMS^{49k} films after spin coating at 6000 rpm and water annealing after 0 or 24 h (500× magnification).

Spin rate (rpm)	Location on sample	Time before annealing (h)	PVOH$^{88\%H,\ 0.1\ wt\%}$	PVOH$^{99\%H,\ 0.1\ wt\%}$
6000	Center	0	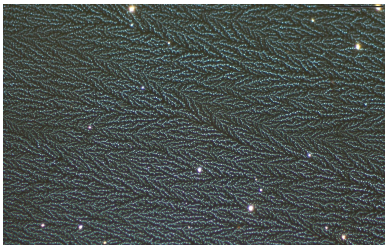	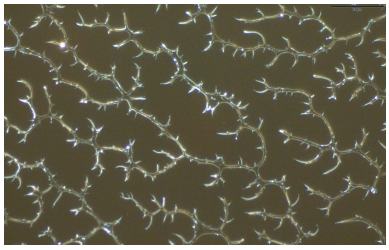
	Edge	0	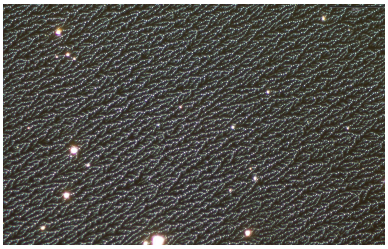	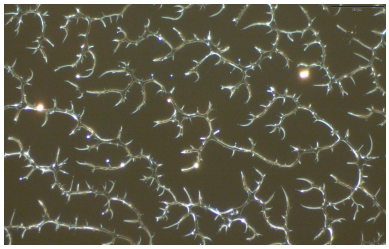
6000	Center	24	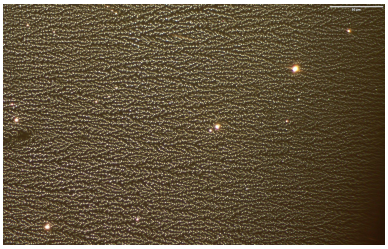	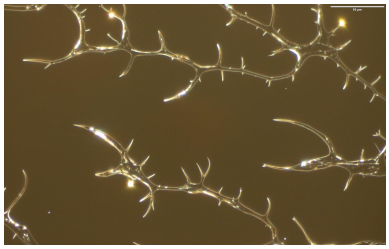
	Edge	24	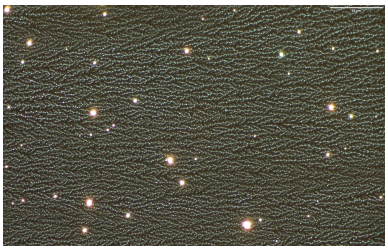	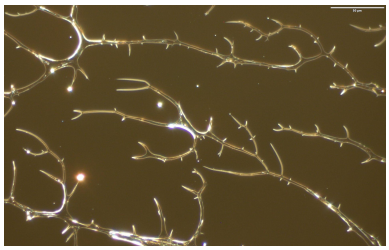

The global optical images of the PVOH$^{88\%H,\ 0.1\ wt\%}$-PDMS^{49k} films after spin coating and water annealing after 24 h were also obtained (Table 15). The exit lines, the outer ring, and the initial footprint were less pronounced after water annealing, confirming that PVOH$^{88\%H,\ 0.1\ wt\%}$ rearranges on the global/microscopic scale to distribute more evenly over a substrate after water

annealing. These results indicate that it is more thermodynamically stable for $PVOH^{88\%H,\ 0.1\ wt\%}$ films to form droplet morphology, and more thermodynamically stable for $PVOH^{99\%H,\ 0.1\ wt\%}$ films to form more extensive crystal structures via aggregation.

Table 15. Global optical images of $PVOH^{88\%H,\ 0.1\ wt\%}$-$PDMS^{49k}$ films after spin coating and water annealing after 24 h.

900 rpm	6000 rpm
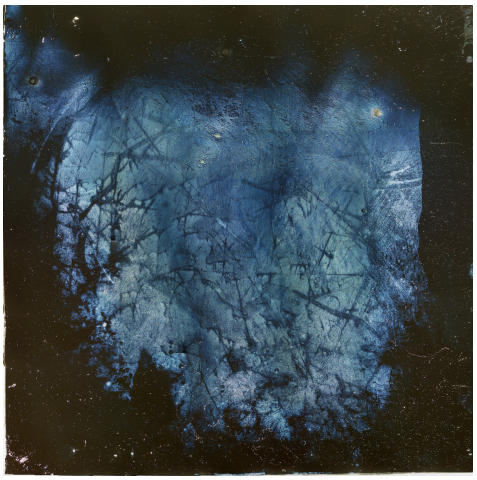	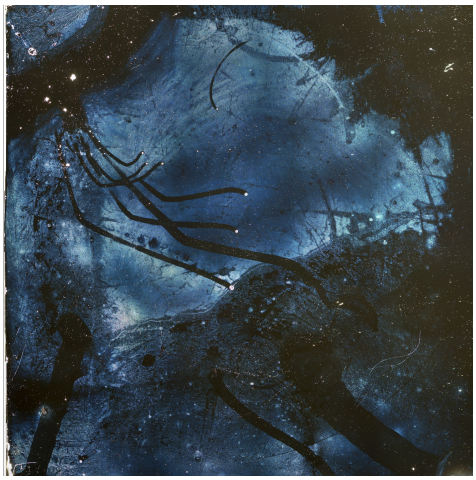

3.7 Fractal analysis following spin coating and water annealing

3.7.1 $PDMS^{9k}$ Substrate

The morphologies of the spin-coated, the immediately-annealed, and the delayed-annealed $PVOH^{0.1\ wt\%}$-$PDMS^{9k}$ films were also analyzed by determining the % PVOH surface coverage, the fractal dimension D values, and the fractal lacunarity L values. The % PVOH surface coverage was dependent on the % hydrolysis and the sample treatment (Figures 39 and 40). Generally, the $PVOH^{88\%H,\ 0.1\ wt\%}$-$PDMS^{9k}$ films covered less of the $PDMS^{9k}$ substrate than the $PVOH^{99\%H,\ 0.1\ wt\%}$-$PDMS^{9k}$ films. The % surface coverage of the $PVOH^{88\%H,\ 0.1\ wt\%}$-$PDMS^{9k}$ films was similar across the different spin rates, the location on the sample, and the treatment, but increased slightly on the immediately-annealed samples. This also

suggests that the higher plasticity of the freshly-spin-coated films allows for greater rearrangement and progress toward the equilibrium morphology.

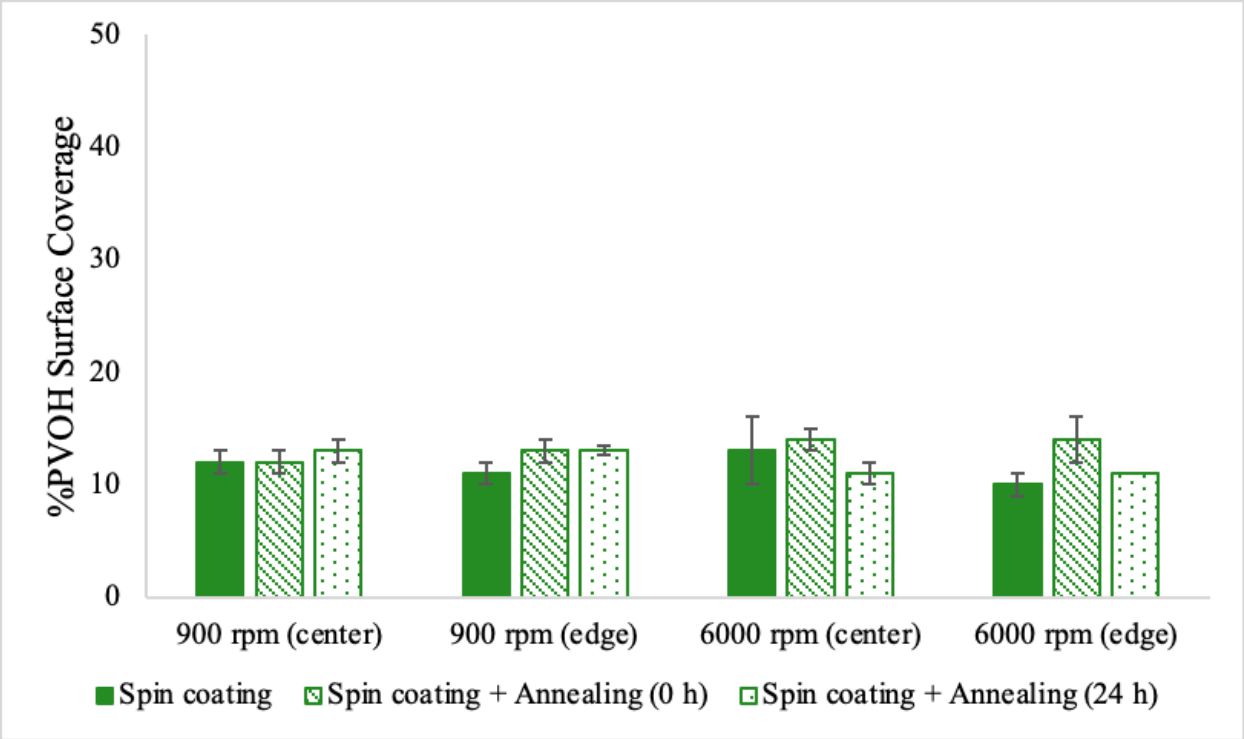

Figure 39. % PVOH$^{88\%H,\ 0.1\ wt\%}$ surface coverage on PDMS^{9k} after spin coating and water annealing after 0 or 24 h.

The % surface coverage of the PVOH$^{99\%H,\ 0.1\ wt\%}$-PDMS^{9k} films (Figure 40) showed a greater dependency on condition and spin rate than the % surface coverage of the PVOH$^{88\%H,\ 0.1\ wt\%}$-PDMS^{9k} films (Figure 39). As observed in the optical images of the PVOH$^{99\%H,\ 0.1\ wt\%}$-PDMS^{9k} films (Tables 13a and 13b), the % PVOH surface coverage increased significantly after delayed-annealing, especially after spin coating at 6000 rpm. This result coincides with the growth of smaller PVOH$^{99\%H}$ fractals formed in the delayed-aggregation process, magnified by the greater kinetic entrapment at 6000 rpm.

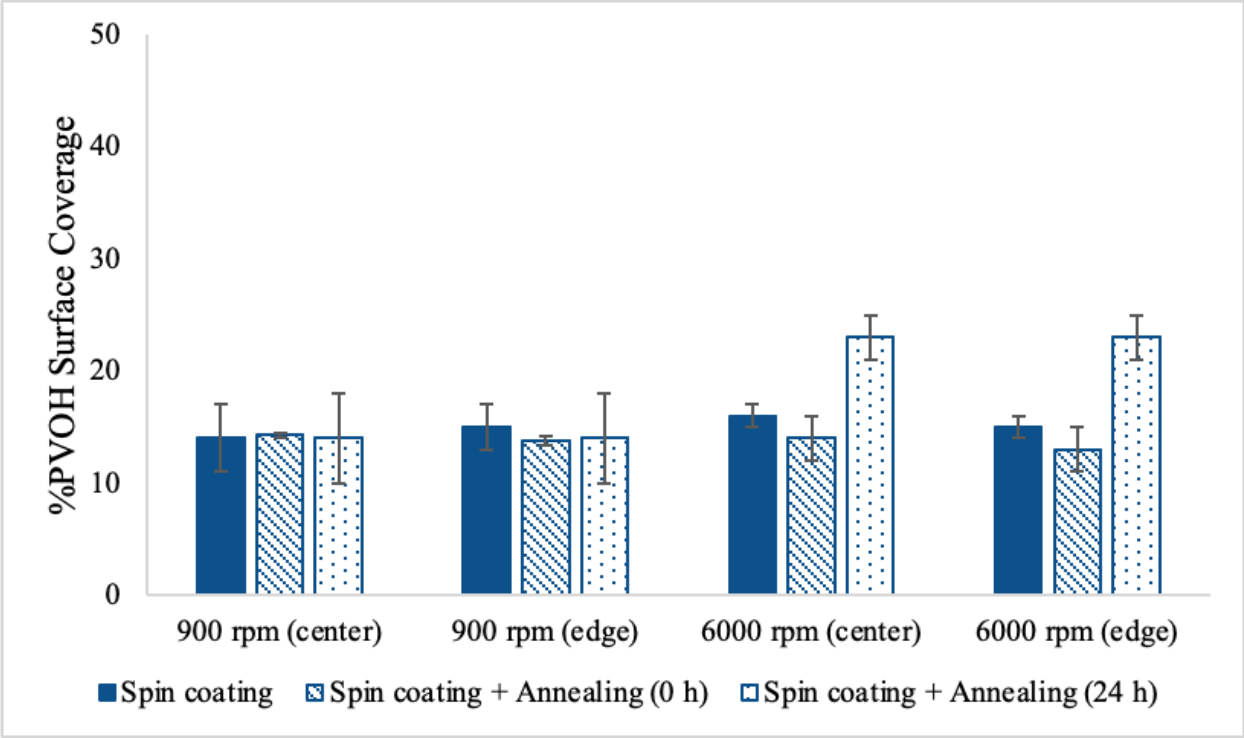

Figure 40. % PVOH$^{99\%H,\ 0.1\ wt\%}$ surface coverage on PDMS^{9k} after spin coating and water annealing after 0 or 24 h.

The D values of the PVOH$^{88\%H,\ 0.1\ wt\%}$-PDMS^{9k} films (Figure 41) were greater than the D values of the PVOH$^{99\%H,\ 0.1\ wt\%}$-PDMS^{9k} films (Figure 42) as a result of the greater complexity and smaller pattern scale. The D values of the PVOH$^{88\%H,\ 0.1\ wt\%}$-PDMS^{9k} films were fairly consistent across the different spin rates and the locations on the samples. The only D value that noticeably differed was for the spin-coated edge of the 6000 rpm sample, which was lower due to the greater centripetal force at the highest spin rate at the edge of the sample. The D values of the PVOH$^{99\%H,\ 0.1\ wt\%}$-PDMS^{9k} films varied more than the PVOH$^{88\%H,\ 0.1\ wt\%}$-PDMS^{9k} films. Again, the delayed-annealed PVOH$^{99\%H,\ 0.1\ wt\%}$-PDMS^{9k} films prepared at 6000 rpm had greater D values than the other films as a result of the combined effects of kinetic entrapment and delayed-annealing.

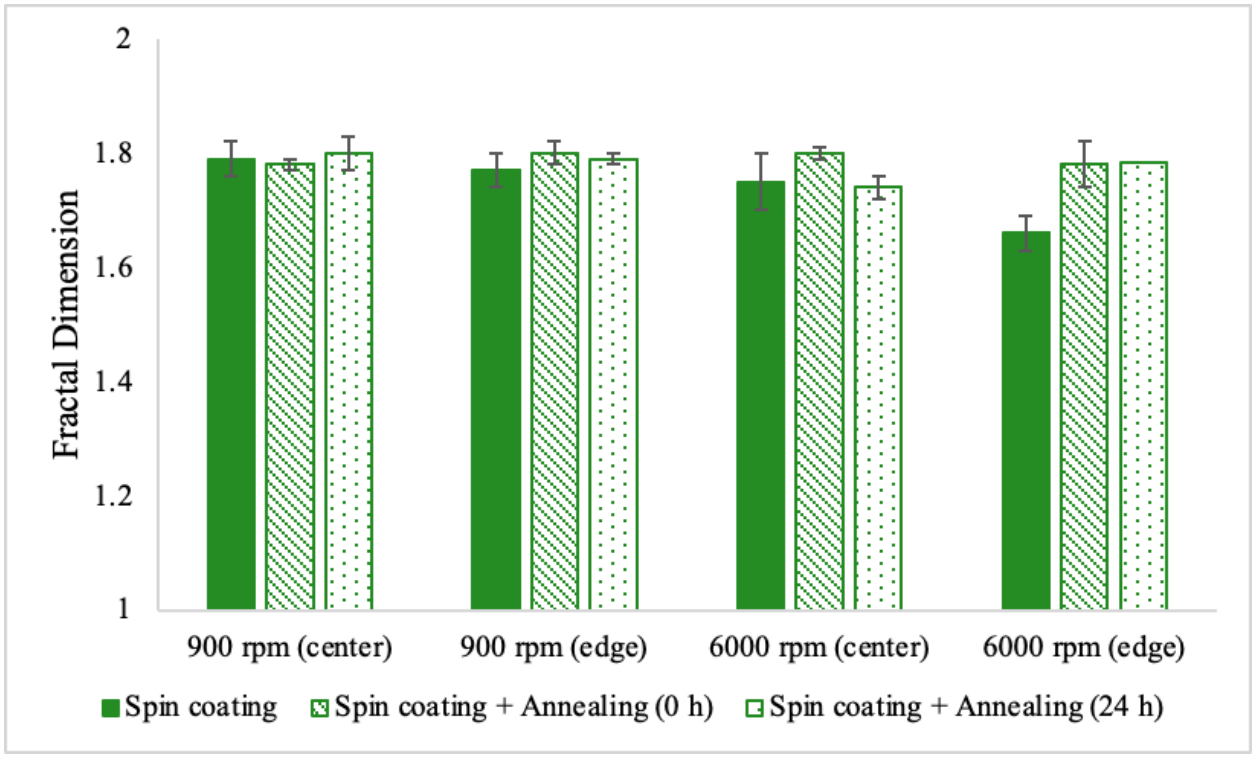

Figure 41. Fractal dimension D of PVOH$^{88\%H,\ 0.1\ wt\%}$-PDMS^{9k} films after spin coating and water annealing after 0 or 24 h.

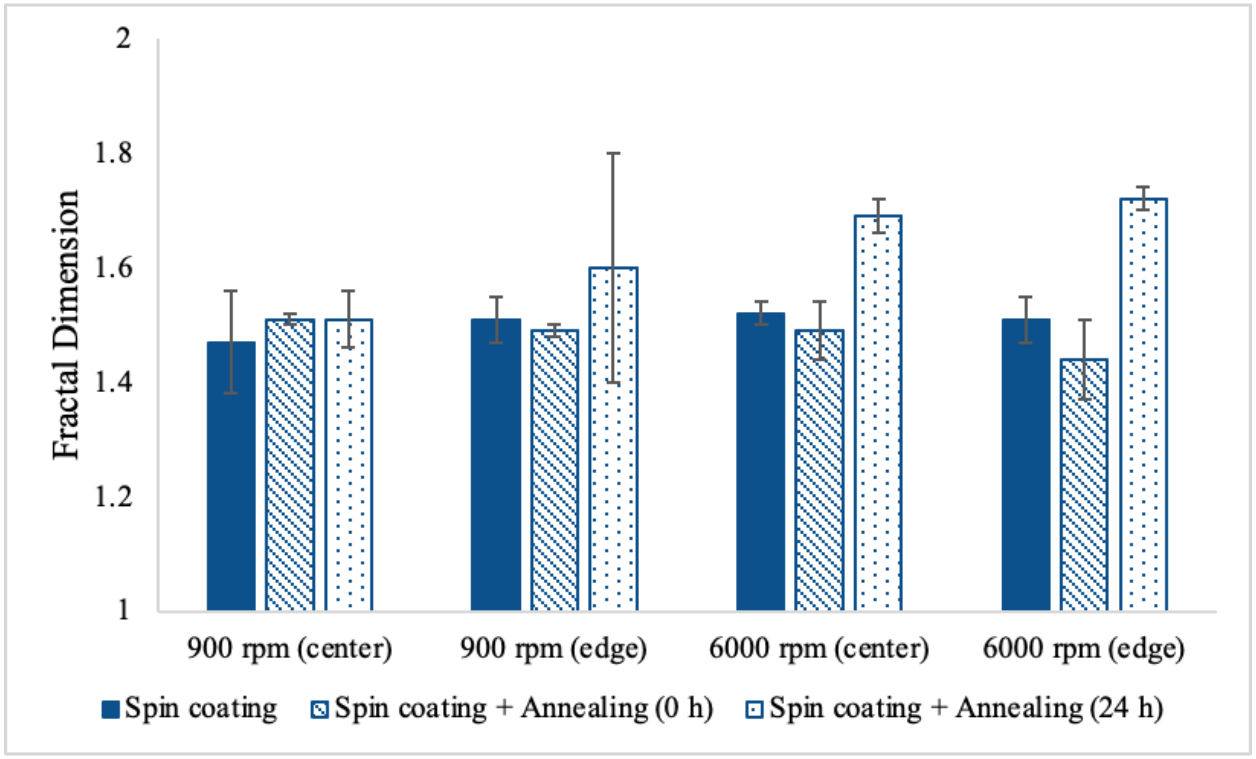

Figure 42. Fractal dimension D of PVOH$^{99\%H,\ 0.1\ wt\%}$-PDMS^{9k} films after spin coating and water annealing after 0 or 24 h.

The L values of the PVOH$^{88\%H,\ 0.1\ wt\%}$-PDMS^{9k} films (Figure 43) were less than the L values of the PVOH$^{99\%H,\ 0.1\ wt\%}$-PDMS^{9k} films (Figure 44) as a result of the greater heterogeneity of the PVOH$^{99\%H,\ 0.1\ wt\%}$-PDMS^{9k} films. This lacunarity largely arises from the tendency of PVOH$^{99\%H}$ to aggregate and crystallize. While there were fewer obvious trends in L values, the delayed-annealed PVOH$^{99\%H,\ 0.1\ wt\%}$-PDMS^{9k} films prepared at 6000 rpm had the lowest L values due to the numerous smaller fractals covering the surface and reducing the lacunarity of the films.

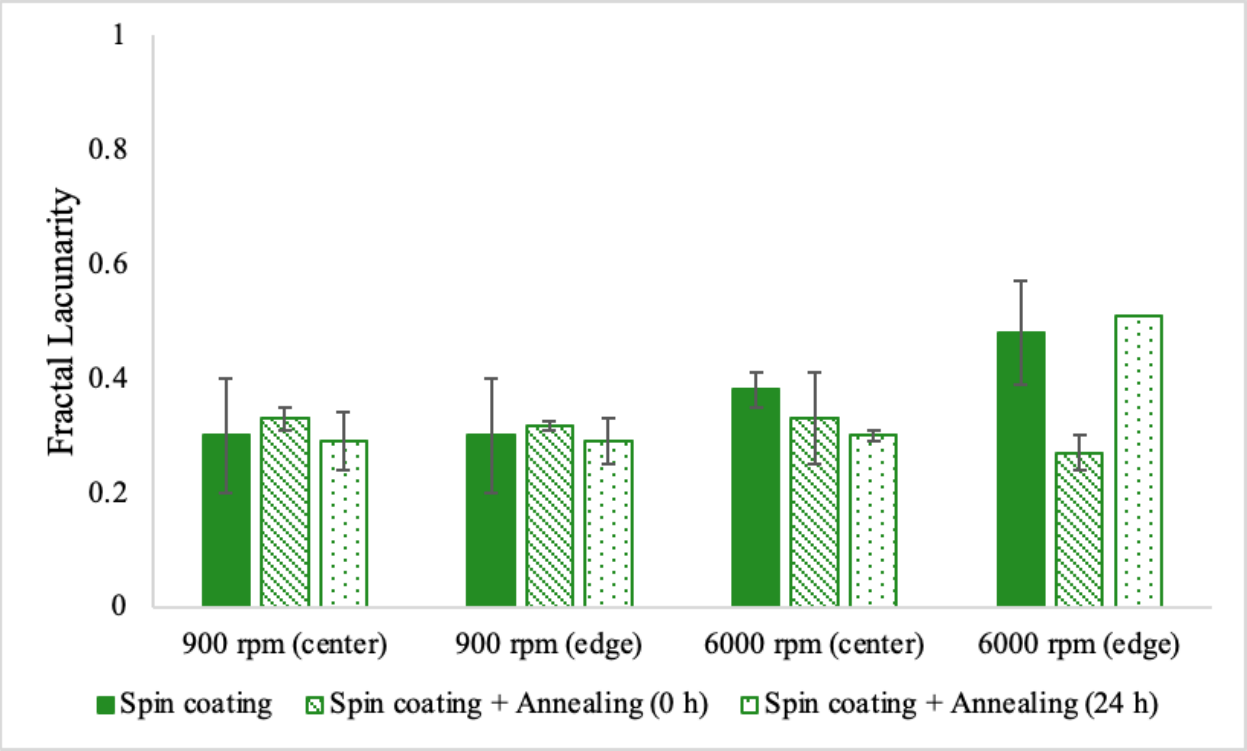

Figure 43. Fractal lacunarity L of PVOH$^{88\%H,\ 0.1\ wt\%}$-PDMS^{9k} films after spin coating and water annealing after 0 or 24 h.

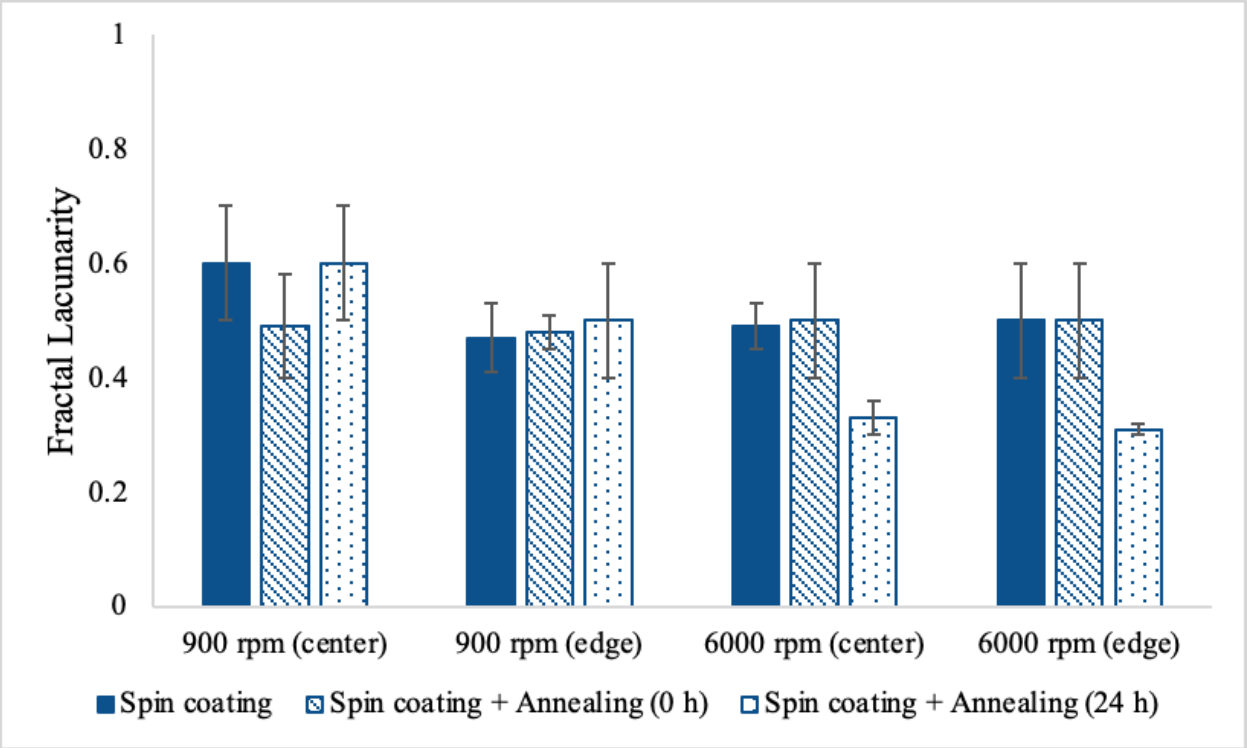

Figure 44. Fractal lacunarity L of PVOH$^{99\%H,\ 0.1\ wt\%}$-PDMS^{9k} films after spin coating and water annealing after 0 or 24 h.

3.7.2 PDMS^{49k} Substrate

The % PVOH$^{88\%H,\ 0.1\ wt\%}$ surface coverage on PDMS^{49k} after spin coating, immediately-annealing, and delayed-annealing were within standard deviation for the different spin rates, the locations on the samples, and the treatments (Figure 45). The % PVOH$^{99\%H,\ 0.1\ wt\%}$ surface coverage on PDMS^{49k} after spin coating, immediately-annealing, and delayed-annealing were also generally within standard deviation for the different spin rates, the locations on the samples, and the treatments (Figure 46). The % surface coverage values of the PVOH$^{88\%H,\ 0.1\ wt\%}$-PDMS^{49k} and PVOH$^{99\%H,\ 0.1\ wt\%}$-PDMS^{49k} films were more similar than the PVOH$^{88\%H,\ 0.1\ wt\%}$-PDMS^{9k} and PVOH$^{99\%H,\ 0.1\ wt\%}$-PDMS^{9k} films (Figures 39 and 40), most likely due to the higher substrate mobility allowing for greater film rearrangement.

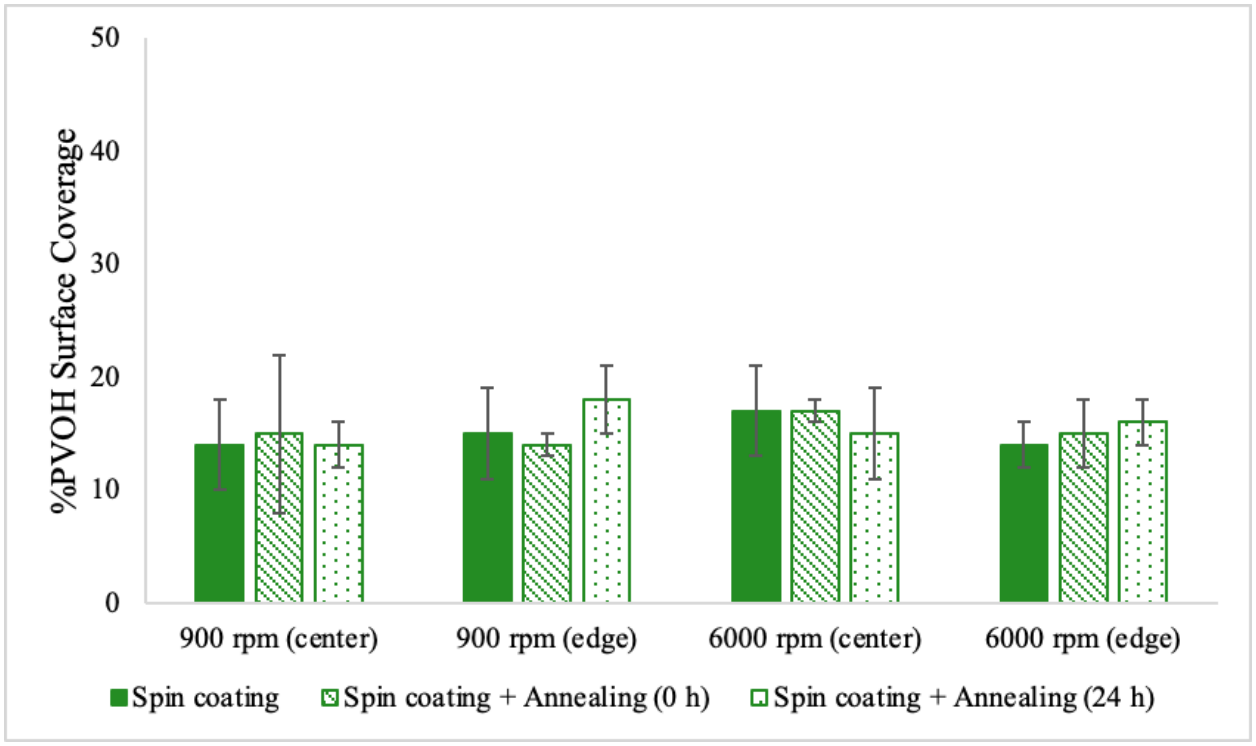

Figure 45. % PVOH$^{88\%H,\ 0.1\ wt\%}$ surface coverage on PDMS^{49k} after spin coating and water annealing after 0 or 24 h.

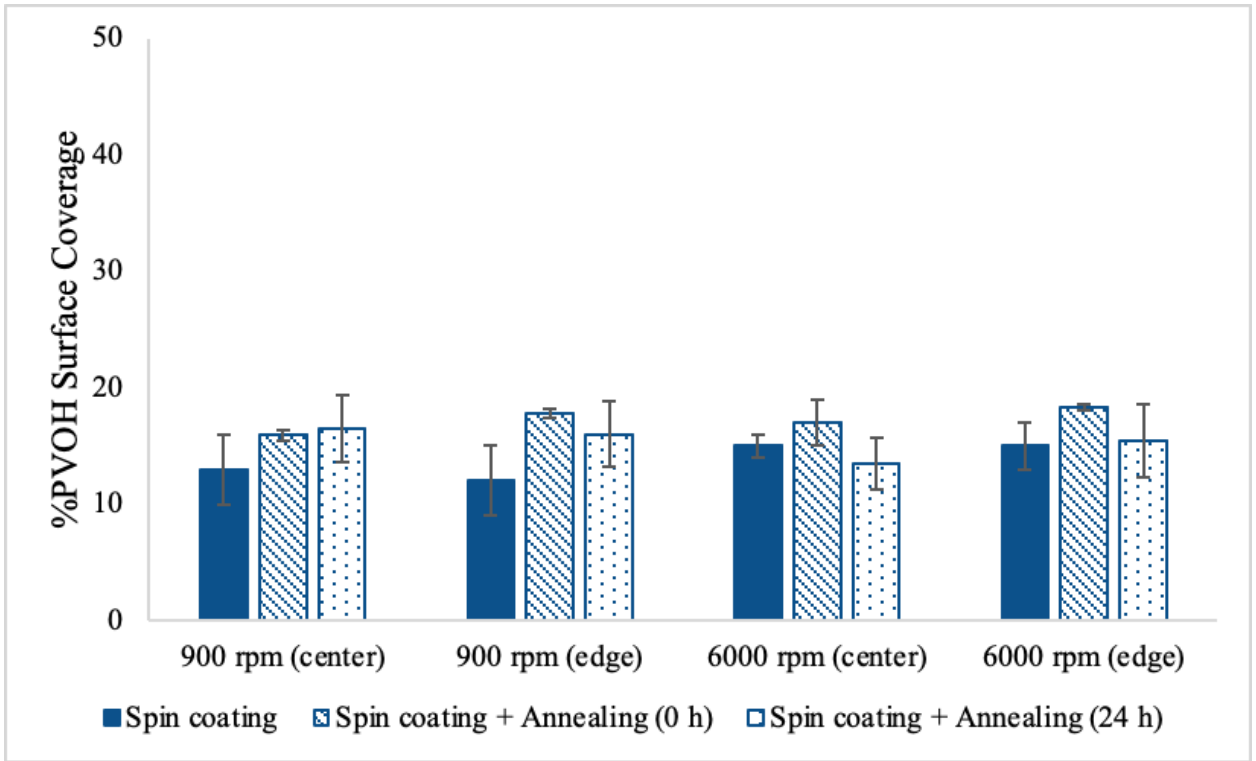

Figure 46. % PVOH$^{99\%H,\ 0.1\ wt\%}$ surface coverage on PDMS^{49k} after spin coating and water annealing after 0 or 24 h.

Similar to the results on PDMS^{9k}, the D values of the PVOH$^{88\%H,\ 0.1\ wt\%}$-PDMS^{49k} films (Figure 47) were greater than the D values of the PVOH$^{99\%H,\ 0.1\ wt\%}$-PDMS^{49k} films (Figure 48). The D values of the PVOH$^{88\%H,\ 0.1\ wt\%}$-PDMS^{49k} films were approximately equal to the D values of the PVOH$^{88\%H,\ 0.1\ wt\%}$-PDMS^{9k} films (Figure 41). However, the D values of the PVOH$^{99\%H,\ 0.1\ wt\%}$-PDMS^{49k} films differed in trend compared to the PVOH$^{99\%H,\ 0.1\ wt\%}$-PDMS^{9k} films (Figure 42), where the PVOH$^{99\%H,\ 0.1\ wt\%}$-PDMS^{49k} films with the largest D values were the immediate-adsorbed films rather than the delayed-annealed films. However, these data are not the most reliable since the immediately-annealed and the delayed-annealed films came from different experiments and the substrates were likely different thicknesses, resulting in different sizes of fractals.

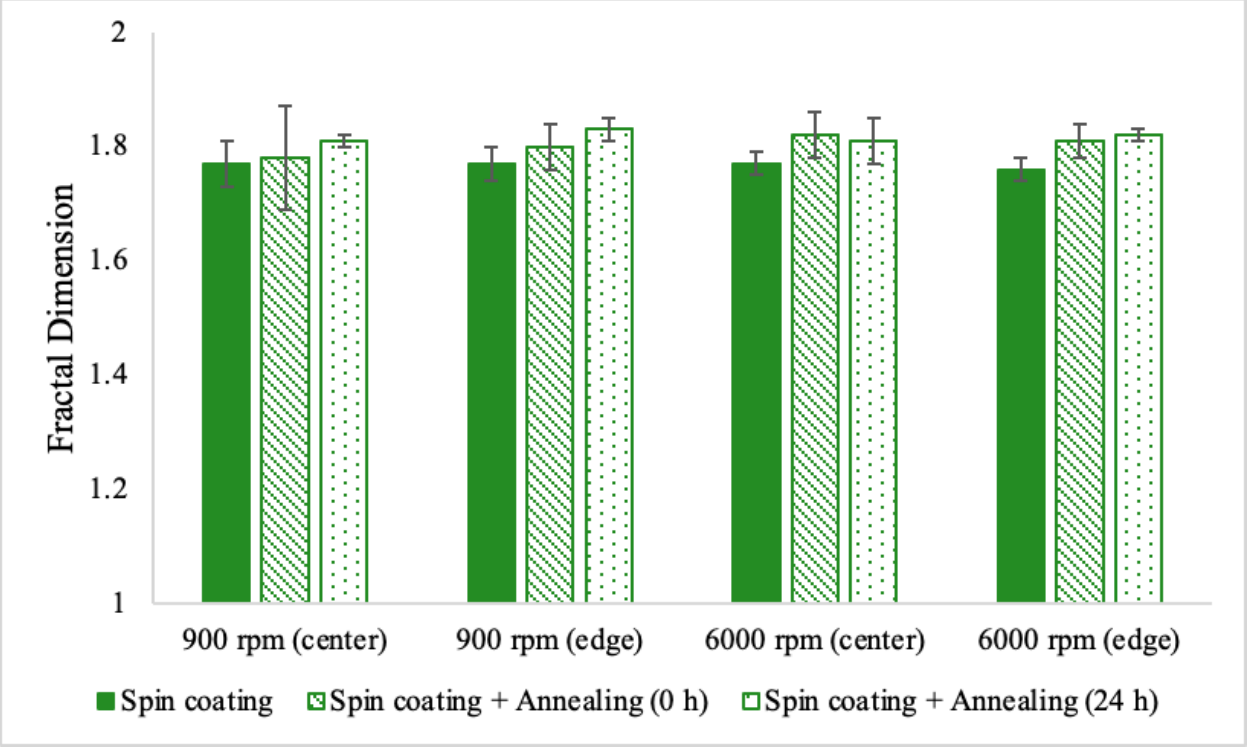

Figure 47. Fractal dimension D of PVOH$^{88\%H,\ 0.1\ wt\%}$-PDMS^{49k} films after spin coating and water annealing after 0 or 24 h.

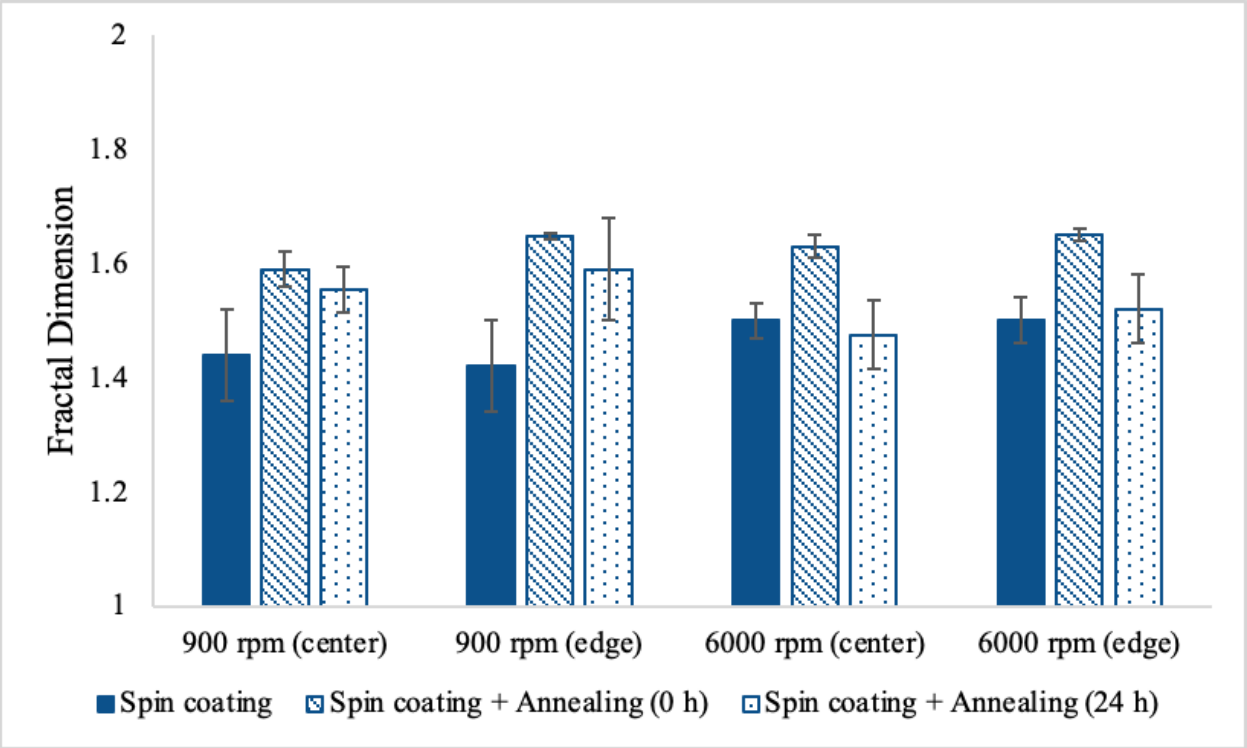

Figure 48. Fractal dimension D of $PVOH^{99\%H,\ 0.1\ wt\%}$-$PDMS^{49k}$ films after spin coating and water annealing after 0 or 24 h.

Similar to the results on $PDMS^{9k}$, the L values of the $PVOH^{88\%H,\ 0.1\ wt\%}$-$PDMS^{49k}$ films (Figure 49) were less than the L values of the $PVOH^{99\%H,\ 0.1\ wt\%}$-$PDMS^{49k}$ films (Figure 50) as a result of the increased heterogeneity of the $PVOH^{99\%H,\ 0.1\ wt\%}$-$PDMS^{49k}$ films. The L values of the $PVOH^{88\%H,\ 0.1\ wt\%}$-$PDMS^{49k}$ films were within standard deviation across the different spin rates, the locations on the samples, and the conditions. If all of the $PVOH^{99\%H,\ 0.1\ wt\%}$-$PDMS^{49k}$ films had been prepared on substrates of approximately equal thickness, then the feature sizes and substrate mobility would be more consistent across the different batches, and the $PVOH^{99\%H,\ 0.1\ wt\%}$-$PDMS^{49k}$ films would also be expected to possess approximately equal L values.

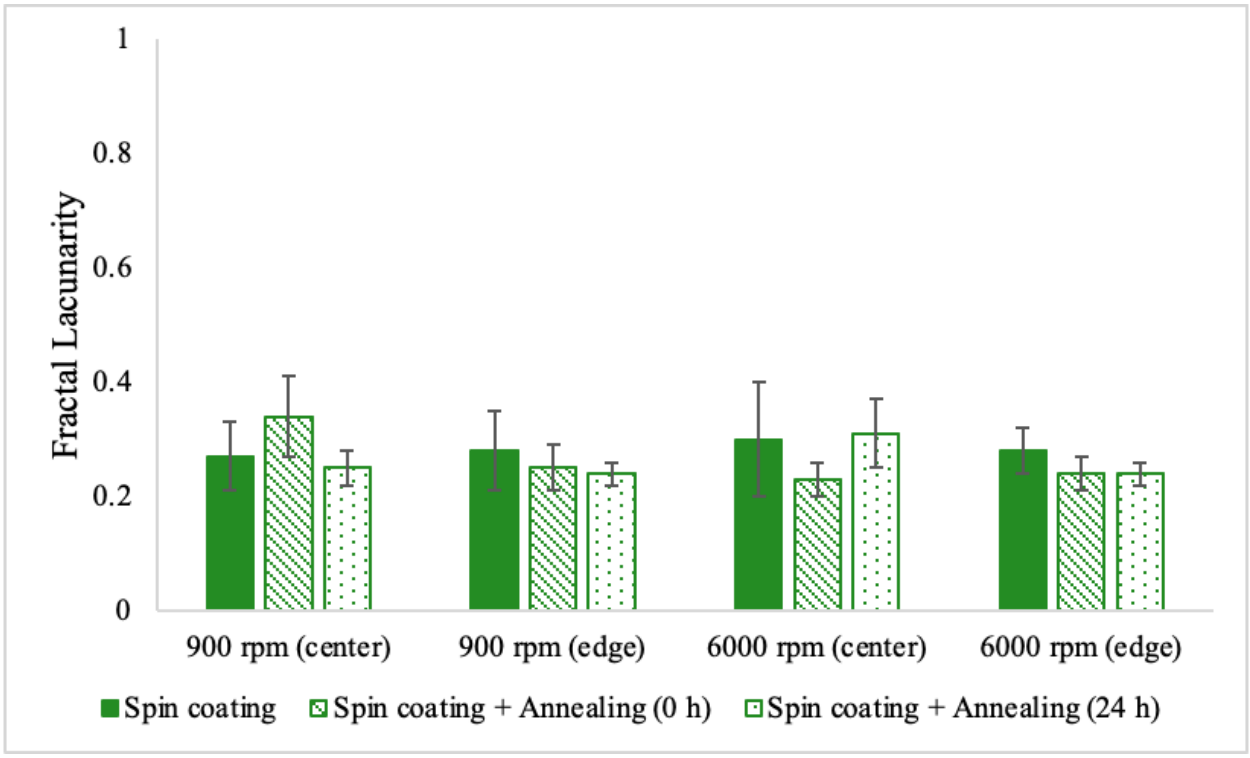

Figure 49. Fractal lacunarity L of PVOH$^{88\%H,\ 0.1\ wt\%}$-PDMS^{49k} films after spin coating and water annealing after 0 or 24 h.

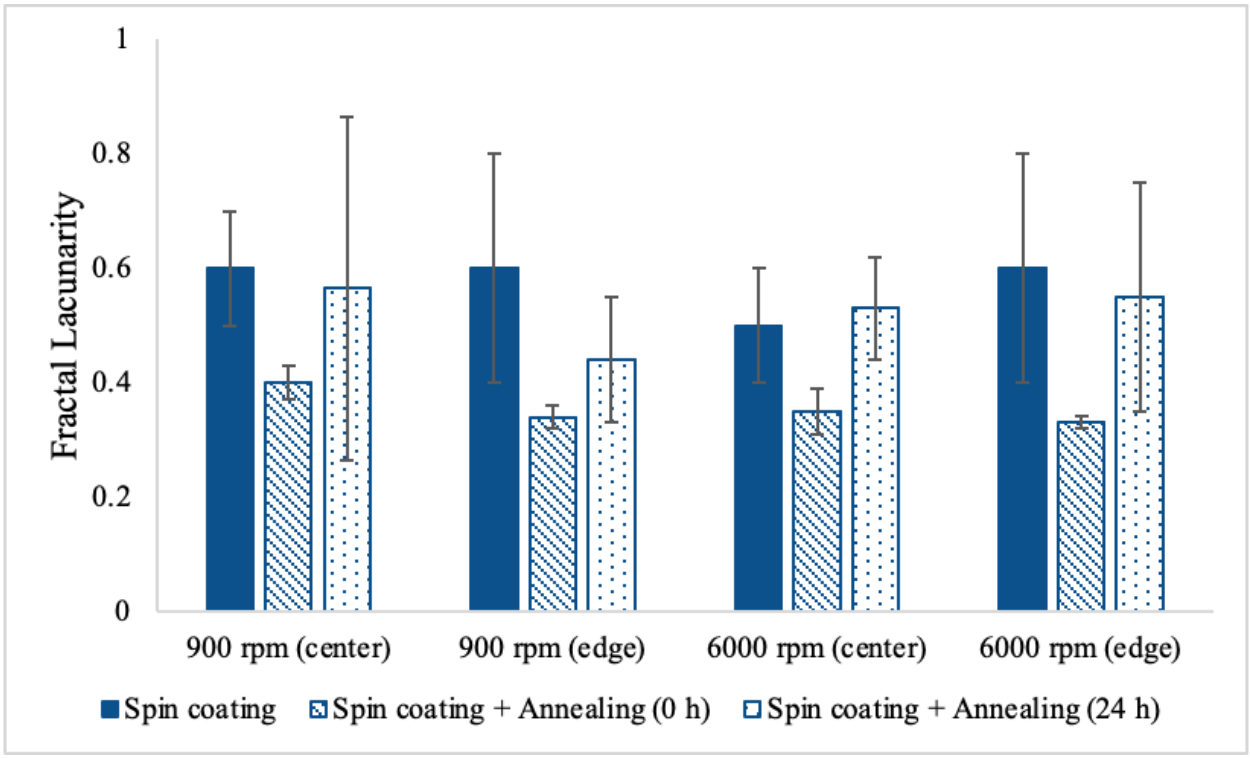

Figure 50. Fractal lacunarity L of PVOH$^{99\%H,\ 0.1\ wt\%}$-PDMS^{49k} films after spin coating and water annealing after 0 or 24 h.

IV. CONCLUSIONS AND FUTURE WORK

We fabricated PVOH thin films on PDMS substrates via static adsorption and adsorptive spin coating, and determined the stability of the films to water. The thickness, wettability, and morphology of the thin films were primarily studied as functions of PDMS molecular weight, PVOH degree of hydrolysis, and time elapsed between film fabrication and water annealing.

Substrates. The PDMS substrates employed in this study displayed behavior associated with low molecular weight (LMW), intermediate molecular weight (MMW), and high molecular weight (HMW) PDMS. While substrate hydrophobicity generally increased with PDMS molecular weight (MW), the key differentiating variable between the MMW and HMW substrates was substrate mobility rather than hydrophobicity.

Static adsorption. Film thickness and morphology depended strongly on PDMS MW and PVOH % hydrolysis, but were independent of adsorption time and PVOH concentration. These results contradict previous studies and demonstrate that alternative factors, namely substrate mobility and polymer crystallinity, can play principal roles in polymer adsorption.

Water annealing following static adsorption. Film rearrangement due to water annealing was dependent on PDMS MW, PVOH % hydrolysis, and time between static adsorption and annealing. Significant microscopic morphological changes were not necessarily accompanied by significant nanoscopic changes. We found evidence of a loosely-bound h_1 PVOH layer on $PDMS^{9k}$ substrates only. The $PVOH^{99\%H}$-$PDMS^{9k}$ film thickness and morphology were dependent on time before water annealing, while the $PVOH^{88\%H}$-$PDMS^{9k}$ films were

independent of time before water annealing. This signals a difference between the two systems' loosely-bound h_1 layers.

Spin coating. The spin-coated $PVOH^{0.1\ wt\%}$ thicknesses and contact angles were independent of spin rate and PVOH % hydrolysis on $PDMS^{9k}$ and $PDMS^{49k}$; both systems are unstable, and the films are extremely dewetted. The presence of a loosely-bound h_1 layer depends on substrate mobility and PVOH % hydrolysis. The PVOH morphologies were more consistent on $PDMS^{49k}$ than $PDMS^{9k}$ since $PDMS^{49k}$ lacks a loosely-bound h_1 layer.

Water annealing following spin coating. Consistent with static adsorption and water annealing experiments, water annealing after spin coating resulted in film loss (loosely-bound h_1) and changes in morphology, depending on the PDMS substrate, PVOH % hydrolysis, and time before annealing.

These results provide more insight into the multilayered structure of PVOH-PDMS thin films, as well as the stability of these structures. This study aids our journey toward understanding PVOH film dynamics in different conditions and employing these and other hydrophilic, semicrystalline polymer thin films more precisely.

Future research. It is still being determined whether the PVOH morphologies observed on $PDMS^{9k}$ and $PDMS^{49k}$ after water annealing are the most thermodynamically stable. Water annealing over various time frames and with additional heat energy could give more information about the progression of film rearrangement and provide a better understanding of the structure of these films. Additionally, since adsorbed PVOH-$PDMS^{2k}$ and PVOH-$PDMS^{9k}$ films follow similar thickness trends, it is possible that PVOH-$PDMS^{2k}$ films also possess loosely-bound h_1 layers. Using less forceful rinsing methods on the PVOH-$PDMS^{2k}$ films or providing additional

heat energy during water annealing could reveal potential loosely-bound h_1 layers in PVOH-PDMS^{2k} films.

APPENDIX

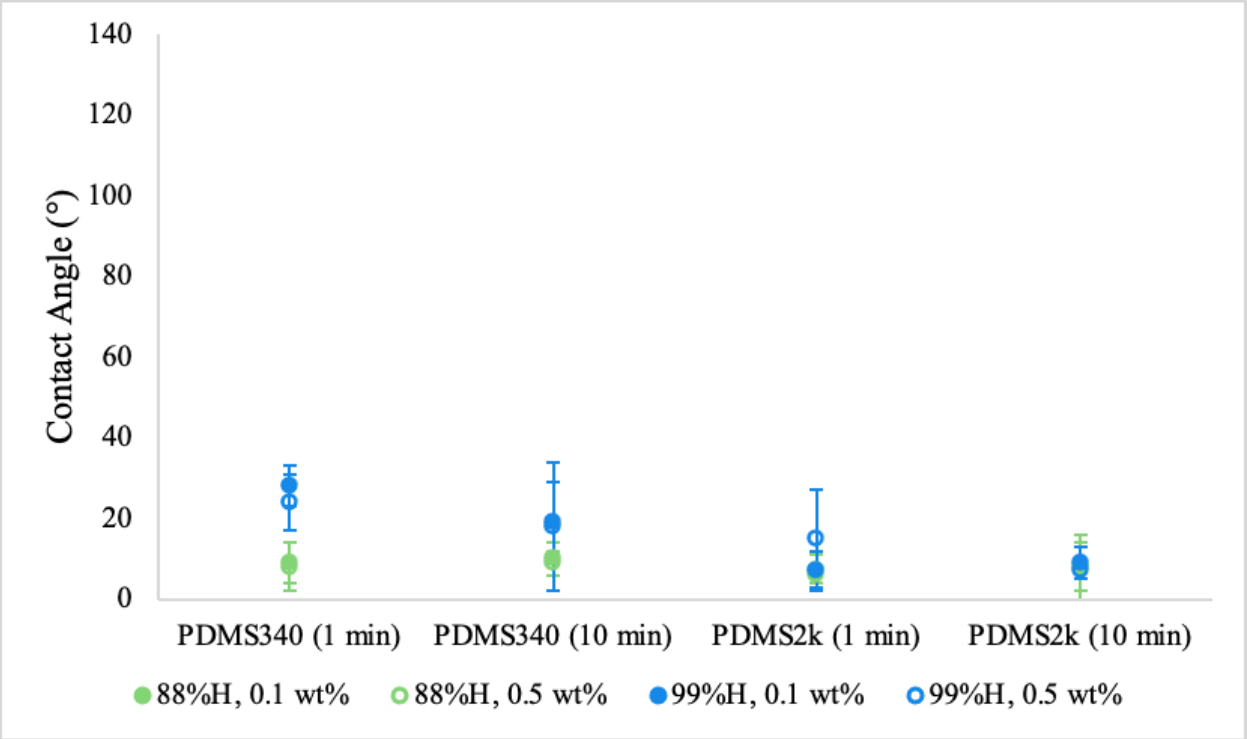

Figure 51. Receding contact angles of PVOH-PDMS films after static adsorption for 1 or 10 min.

Table 16a. Additional optical images of PVOH$^{88\%H,\ 0.1\ wt\%}$-PDMS^{9k} films prepared by spin coating (500× magnification).

Spin rate (rpm)	1400	2200	3500	4800
Center	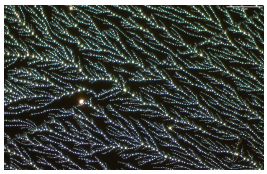		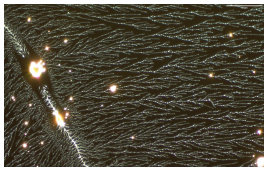	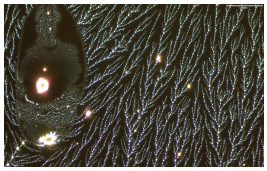
Edge				

Table 16b. Additional optical images of PVOH$^{99\%H,\ 0.1\ wt\%}$-PDMS^{9k} films prepared by spin coating (500× magnification).

Spin rate (rpm)	1400	2200	3500	4800
Center	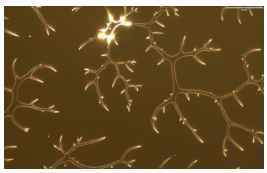	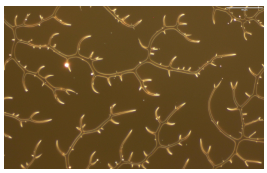	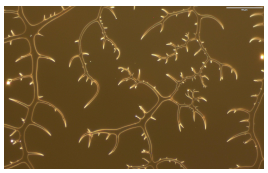	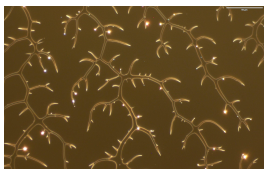
Edge	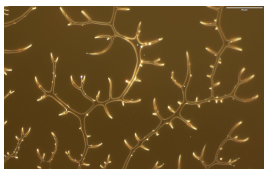	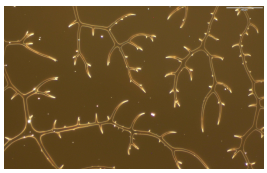	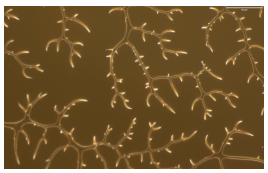	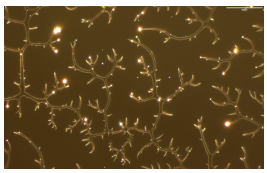

Table 17a. Additional optical images of PVOH$^{88\%H,\ 0.1\ wt\%}$-PDMS^{49k} films prepared by spin coating (500× magnification).

Spin rate (rpm)	1400	2200	3500	4800
Center	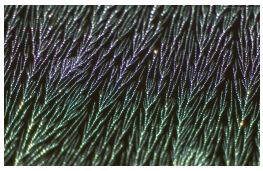	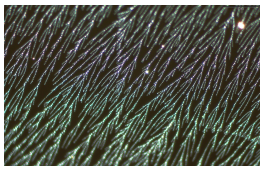	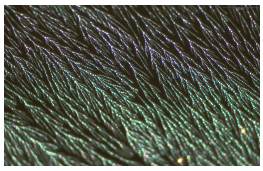	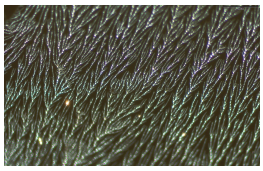
Edge	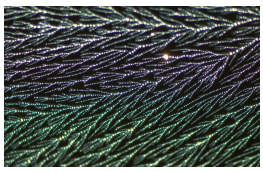	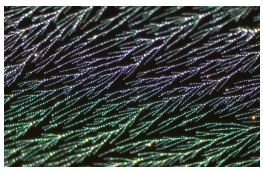	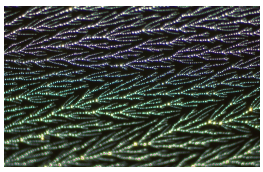	

Table 17b. Additional optical images of PVOH$^{99\%H,\ 0.1\ wt\%}$-PDMS^{49k} films prepared by spin coating (500× magnification).

Spin rate (rpm)	1400	2200	3500	4800
Center	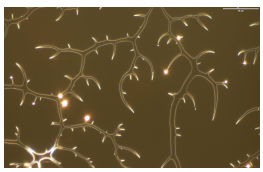	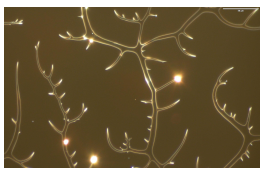	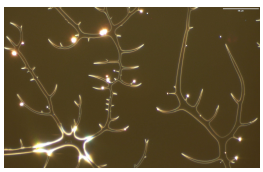	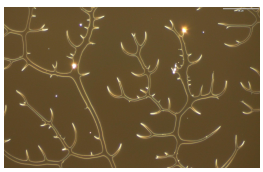
Edge	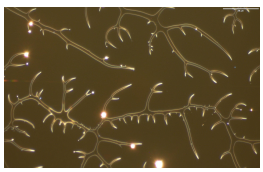	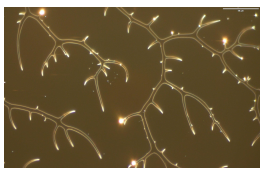	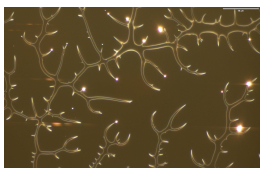	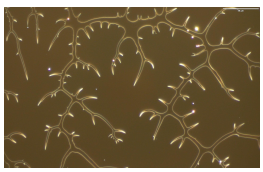

Table 18a. Additional global optical images of PVOH$^{88\%H,\ 0.1\ wt\%}$-PDMS^{49k} films prepared by spin coating.

1400 rpm	2200 rpm	3500 rpm	4800 rpm
	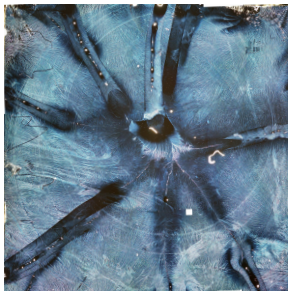		 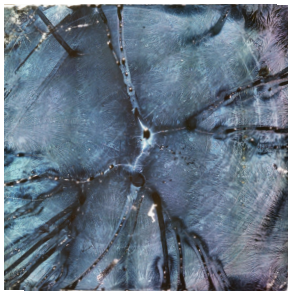

Table 18b. Additional global optical images of PVOH$^{99\%H,\ 0.1\ wt\%}$-PDMS^{49k} films prepared by spin coating.

1400 rpm	2200 rpm	3500 rpm	4800 rpm
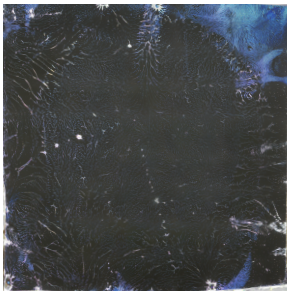 	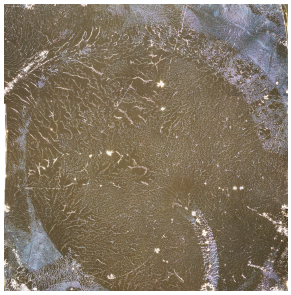	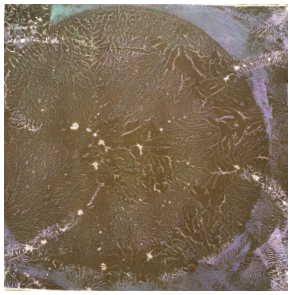	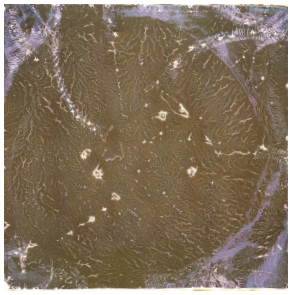

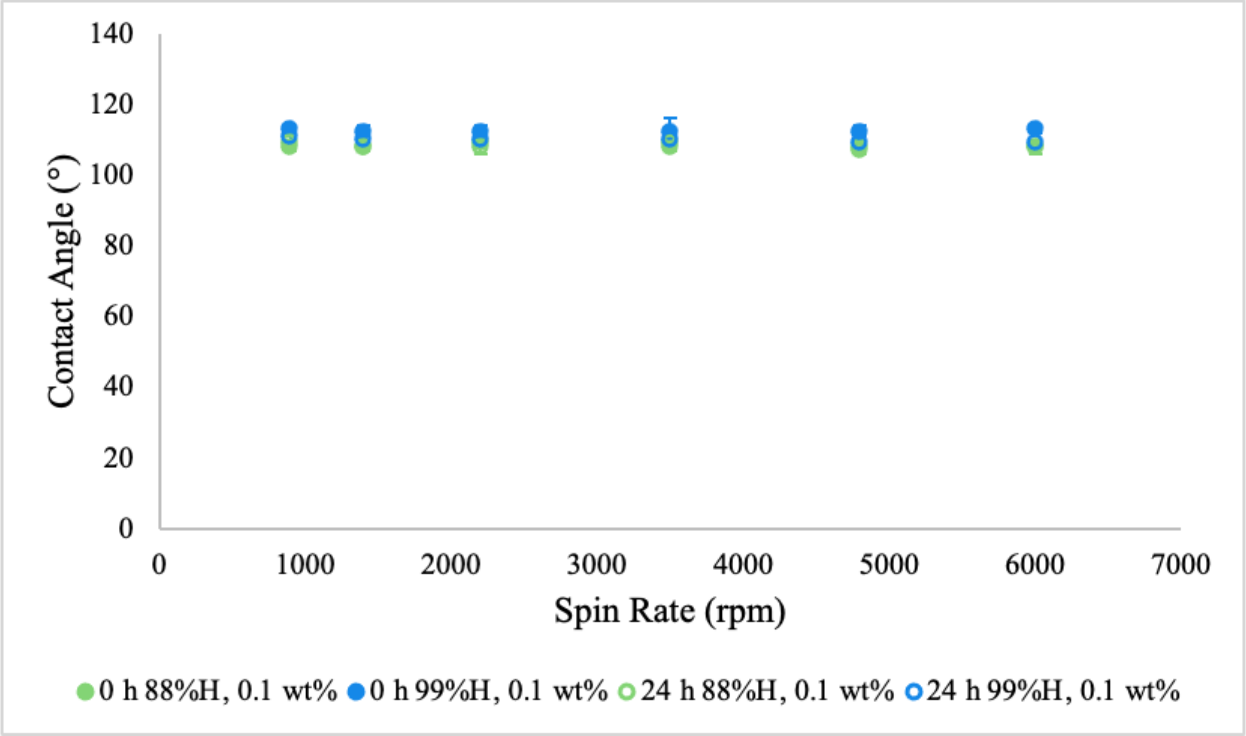

Figure 52. Advancing contact angles of PVOH-PDMS^{9k} films after spin coating and water annealing after 0 or 24 h.

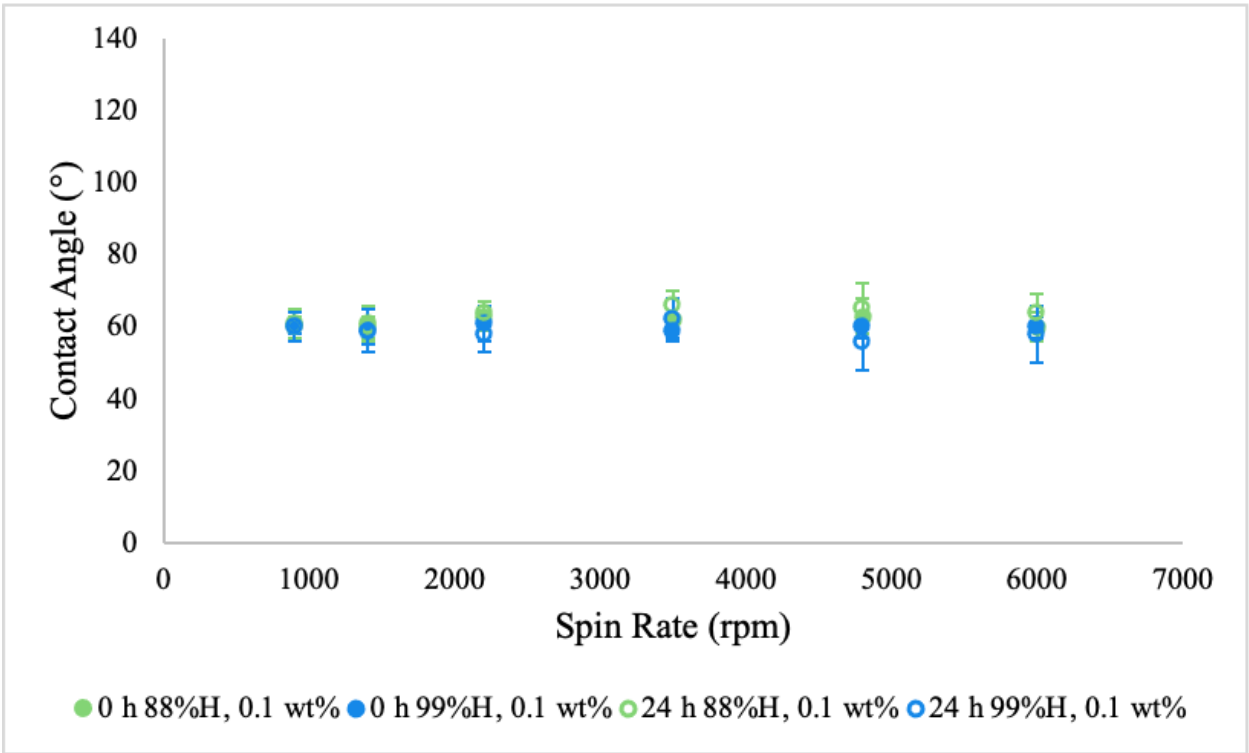

Figure 53. Receding contact angles of PVOH-PDMS^{9k} films after spin coating and water annealing after 0 or 24 h.

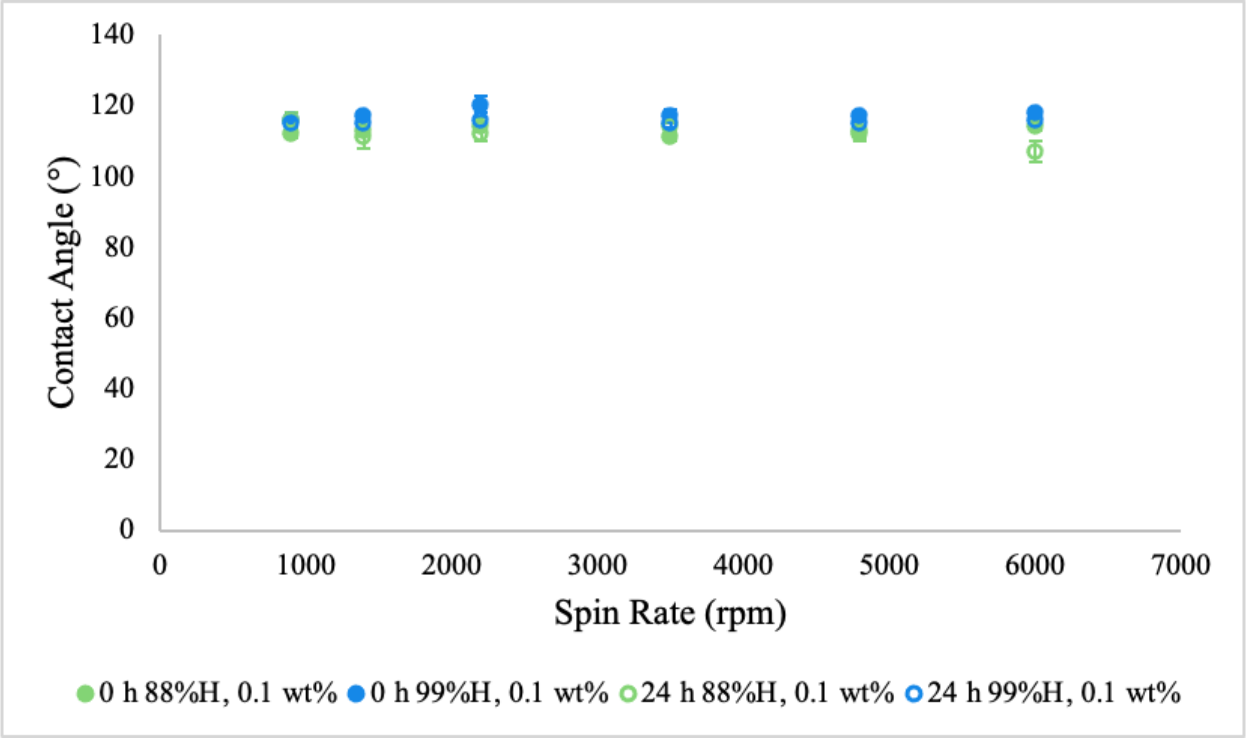

Figure 54. Advancing contact angles of PVOH-PDMS^{49k} films after spin coating and water annealing after 0 or 24 h.

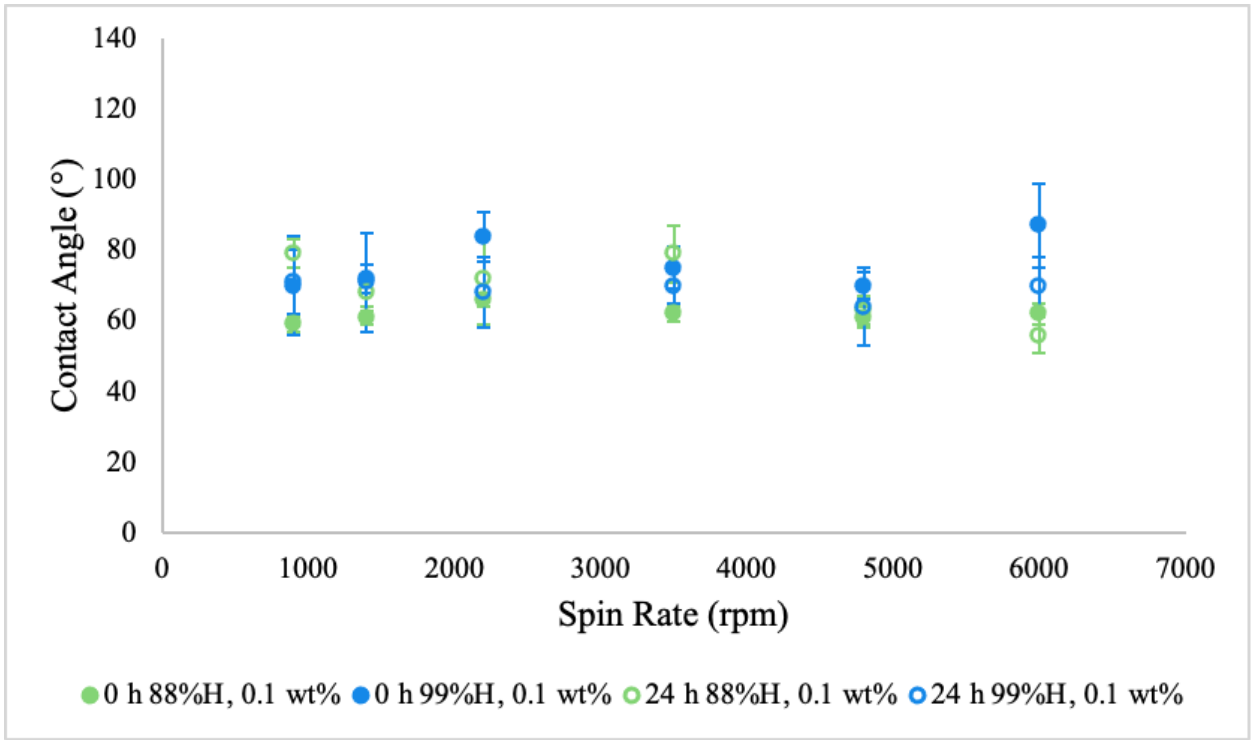

Figure 55. Receding contact angles of PVOH-PDMS^{49k} films after spin coating and water annealing after 0 or 24 h.

REFERENCES CITED

1. Mukherjee, R.; Das, S.; Das, A.; Sharma, S. K.; Raychaudhuri, A. K.; Sharma, A. Stability and Dewetting of Metal Nanoparticle Filled Thin Polymer Films: Control of Instability Length Scale and Dynamics. *ACS Nano* **2010**, *4 (7)*, 3709–3724.

2. Reiter, G. Dewetting of thin polymer films. *Phy. Rev. Lett.* **1992**, *68 (1)*, 75-78.

3. Bischoff, J.; Scherer, D.; Herminghaus, S.; Leiderer, P. *Phys. Rev. Lett.* **1996**, *77 (8)*, 1536.

4. Xie, R.; Karim, A.; Douglas, J. F.; Han C. C.; Weiss, R. A. Spinodal Dewetting of Thin Polymer Films. *Phys. Rev Lett.* **1998**, *81 (6)*, 1251-1254.

5. Jacobs, K.; Herminghaus, S.; Mecke, K. R. Thin Liquid Polymer Films Rupture via Defects. *Langmuir* **1998**, *14 (4)*, 965–969.

6. Hall D. B.; Hooker, J. C.; Torkelson, J. M. Ultrathin polymer films near the glass transition: Effect on the distribution of α-relaxation times as measured by second harmonic generation. *Macromolecules* **1997**, *30 (3)*, 667-669.

7. Keddie, J. L.; Jones, R. A. L.; Cory, R. A. Size-Dependent Depression of the Glass Transition Temperature in Polymer Films. *Europhys. Lett.* **1994**, *27 (1)*, 59-64.

8. Soles, C. L.; Douglas, J. F.; Wu, W. L.; Dimeo, R. M. Incoherent Neutron Scattering and the Dynamics of Confined Polycarbonate Films. *Phys. Rev. Lett.* **2002**, *88 (3)*, 037401.

9. Inuoue, R.; Kanaya, T.; Nishida, K.; Tsukushi, I.; Shibata, K. Inelastic Neutron Scattering Study of Low Energy Excitations in Polymer Thin Films. *Phys. Rev. Lett.* **2005**, *95*, 056102.

10. Krebs, F. C.; Gevorgyan, S. A.; Alstrup, J. A Roll-to-Roll Process to Flexible Polymer Solar Cells: Model Studies, Manufacture and Operational Stability Studies. *J. Mater. Chem.* **2009**, *19 (30)*, 5442−5451.

11. Lipomi, D. J.; Tee, B. C. K.; Vosgueritchian, M.; Bao, Z. Stretchable Organic Solar Cells. *Adv. Mater.* **2011**, *23 (15)*, 1771−1775.

12. Yang, Z.; Deng, J.; Sun, X.; Li, H.; Peng, H. Stretchable, Wearable Dye-Sensitized Solar Cells. *Adv. Mater.* **2014**, *26 (17)*, 2643−2647.

13. Salvatore, G. A.; Münzenrieder, N.; Kinkeldei, T.; Petti, L.; Zysset, C.; Strebel, I.; Büthe, L.; Tröster, G. Wafer-Scale Design of Lightweight and Transparent Electronics That Wraps around Hairs. *Nat. Commun.* **2014**, *5*, 2982.

14. Chen, C. S.; Mrksich, M.; Huang, S.; Whitesides, G. M.; Ingber, D. E. Geometric control of cell life and death. *Science* **1997**, *276 (5317)*, 1425-1428.

15. Zhou, H. X.; Rivas, G. N.; Minton, A. P. Macromolecular crowding and confinement: biochemical, biophysical, and potential physiological consequences. *Annu. Rev. Biophys.* **2008**, *37*, 375–397.

16. *Stem Cells and Regenerative Medicine: From Molecular Embryology to Tissue Engineering*; Appasani, K. and Appasani, R. K., Eds.; Humana Press, 2010**.**

17. An, L.; Li, W.; Nie, Y.; Xie, B.; Li, Z.; Zhang, J.; Yang, B. Patterned magnetic rings fabricated by dewetting of polymer-coated magnetite nanoparticles solution. *J. Colloid Interface Sci*. **2005**, *288 (2)*, 503-507.

18. Boltau, M.; Walheim, S.; Mlynek, J.; Krausch, G.; Steiner, U. Surface-induced structure formation of polymer blends on patterned substrates. *Nature* **1998**, *391*, 877-879.

19. Heier, J.; Kramer, E. J.; Walheim, S.; Krausch, G. Thin diblock copolymer films on chemically heterogeneous surfaces. *Macromolecules* **1997**, *30 (21)*, 6610-6614.

20. Seemann, R.; Herminghaus, S.; Jacobs, K. Dewetting Patterns and Molecular Forces: A Reconciliation. *Phys. Rev. Lett.* **2001**, *86*, 5534-5537.

21. Gentili, D.; Foschi, G.; Valle, F.; Cavallini, M.; Biscarini, F. Applications of dewetting in micro and nanotechnology. *Chem. Soc. Rev.* **2012**, *41 (12)*, 4430-4443.

22. de Gennes, P. G. Wetting: statics and dynamics. *Rev. Mod. Phys.* **1985**, *57 (3)*, 827–863.

23. Sharma, A. Relationship of thin film stability and morphology to macroscopic parameters of wetting in the apolar and polar systems. *Langmuir* **1993**, *9 (3)*, 861–869.

24. Reiter, G. Unstable thin polymer films: rupture and dewetting processes. *Langmuir* **1993**, *9 (5)*, 1344–1351.

25. de Gennes, P. G.; Brochard-Wyart, F.; Quere, D. *Capillarity and Wetting Phenomena: Drops, Bubbles, Pearls, Waves*; Springer, 2004.

26. Sharma, A. and Ruckenstein, E. Energetic criteria for the breakup of liquid films on nonwetting solid surfaces. *J. Colloid Interface Sci.* **1990**, *137 (2)*, 433–445.

27. Herminghaus, S.; Jacobs, K.; Mecke, K.; Bischof, J.; Fery, A.; Ibn-Elhaj, M.; Schlagowski, S. Spinodal dewetting in liquid crystal and liquid metal films. *Science* **1998**, *282 (5390)*, 916–919.

28. Brochard-Wyart, F.; di Meglio, J. M.; Quere, D.; de Gennes, P. G. Spreading of nonvolatile liquids in a continuum picture. *Langmuir*, **1991**, *7 (2)*, 335–338.

29. Young, T. An Essay on the Cohesion of Fluids. *Philos. Trans. Royal Soc.* **1805**, *95*, 65–87.

30. Wenzel, R. N. Surface Roughness and Contact Angle. *J. Phys. Chem.* **1949**, *53 (9)*, 1466–1467.

31. Cassie, A. B. D. Contact Angles. *Discuss. Faraday Soc.* **1948**, *3*, 11– 16.

32. Israelachvili, J. N. and Gee, M. L. Contact angles on chemically heterogeneous surfaces. *Langmuir* **1989**, *5 (1)*, 288– 289.

33. Zhang, B.; Wang, J.; Liu, Z.; Zhang, X. Beyond Cassie equation: Local structure of heterogeneous surfaces determines the contact angles of microdroplets. *Sci. Rep.* **2014**, *4*, 5822.

34. Dussan, E. B. On the Spreading of Liquids on Solid Surfaces: Static and Dynamic Contact Lines. *Annu. Rev. Fluid Mech.* **1979**, *11*, 371–400.

35. Stabel, A.; Heinz, R.; De Schryver, F. C.; Rabe, J. P. Ostwald Ripening of Two-Dimensional Crystals at the Solid-Liquid Interface. *J. Phys. Chem.* **1995**, *99 (2)*, 505–507.

36. Sharma, A. and Reiter, G. Instability of Thin Polymer Films on Coated Substrates: Rupture, Dewetting, and Drop Formation. *J. Colloid Interface Sci.* **1996**, *178 (2)*, 383-399.

37. Reiter, G.; Hamieh, M.; Damman, P.; Sclavons, S.; Gabriele, S.; Vilmin, T.; Raphael, E. Residual stresses in thin polymer films cause rupture and dominate early stages of dewetting. *Nat. Mater.* **2005**, *4 (10)*, 754-758.

38. Xue, L. and Han, Y. Pattern formation by dewetting of polymer thin film. *Prog. Polym. Sci.* **2011**, *36 (2)*, 269–293.

39. Ramanathan, M. and Darling, S. B. Mesoscale morphologies in polymer thin films. *Prog. Polym. Sci.* **2011**, *36 (6)*, 793-812.

40. Saffman, P. G. and Taylor, G. The penetration of a fluid into a porous medium or Hele-Shaw cell containing a more viscous liquid. *Proc. R. Soc. London* **1958**, *245 (1242)*, 312–329.

41. Zeng, H.; Zhao, B.; Israelachvili, J. N.; Tirrell, M. Liquid- to Solid-Like Failure Mechanism of Thin Polymer Films at Micro- and Nanoscales. *Macromolecules* **2010**, *43 (1)*, 538–542.

42. Leshchiner, A.; Thrasher, M.; Mineev-Weinstein, M. B.; Swinney, H. L. Harmonic moment dynamics in Laplacian growth. *Phys. Rev. E* **2010**, *81 (1)*, 2-10.

43. Stach, S. and Cybo, J. Multifractal description of fracture morphology: theoretical basis. *Mater. Charact.* **2003**, *51 (1)*, 79–86.

44. Smith, T. G.; Lange, G. D.; Marks, W. B. Fractal methods and results in cellular morphology - dimensions, lacunarity and multifractals. *J. Neurosci. Methods* **1996**, *69 (2)*, 123-136.

45. *Fractals in Biology and Medicine*; Losa, G. A., Merlini, D., Nonnenmacher, T. F., Weibel, E. R., Eds.; Birkhäuser, 2002.

46. *What is Lacunarity?* https://imagej.nih.gov/ij/plugins/fraclac/FLHelp/Lacunarity.htm#:~:text=FracLac%20delivers%20lacunarity%20based%20on,calculated%20using%20the%20pixel%20distribution (accessed 2023-07-01).

47. Sulpizi, M.; Gaigeot, M. P.; Sprik, M. The Silica-Water Interface: How the Silanols Determine the Surface Acidity and Modulate the Water Properties. *J. Chem. Theory Comput.* **2012**, *8 (3)*, 1037–1047.

48. Jiang, Y.; Minett, M.; Hazen, E.; Wang, W.; Alvarez, C.; Griffin, J.; Jiang, N.; Chen, W. New Insights into Spin Coating of Polymer Thin Films in Both Wetting and Nonwetting Regimes. *Langmuir* **2022**, *38 (41)*, 12702–12710.

49. Zheng, P. Preparation, Characterization, Surface Modification and Applications of Siloxane Polymers. Ph.D. Dissertation, University of Massachusetts Amherst, Amherst, MA, 2012.

50. Krumpfer, J. W. and McCarthy, T. J. Rediscovering Silicones: "Unreactive" Silicones React with Inorganic Surfaces. *Langmuir* **2011**, *27 (18)*, 11514-11519.

51. Kenney, J. F. and Willcockson, G. W. Structure–Property Relationships of Poly(vinyl Alcohol). III. Relationship between Stereoregularity, Crystallinity, and Water Resistance in Poly(vinyl Alcohol). *J. Polym. Sci. A-1 Polym. Chem.* **1966**, *4 (3)*, 679−698.

52. Coupe, B. and Chen, W. A New Approach to Surface Functionalization of Fluoropolymers. *Macromolecules* **2001**, *34 (6)*, 1533-1535.

53. Thiele, U.; Mertig, M.; Pompe, W. Dewetting of an Evaporating Thin Liquid Film: Heterogeneous Nucleation and Surface Instability. *Phys. Rev. Lett.* **1998**, *80 (13)*, 2869–2872.

54. Kozlov, M.; Quarmyne, M.; Chen, W.; McCarthy, T. J. Adsorption of Poly(vinyl alcohol) onto Hydrophobic Substrates. A General Approach for Hydrophilizing and Chemically Activating Surfaces. *Macromolecules* **2003**, *36 (16)*, 6054-6059.

55. Kozlov, M. and McCarthy, T. J. Adsorption of Poly(vinyl alcohol) From Water to a Hydrophobic Surface: Effects of Molecular Weight, Degree of Hydrolysis, Salt, and Temperature. *Langmuir* **2004**, *20 (21)*, 9170– 9176.

56. Barrett, D. A.; Hartshorne, M. S.; Hussain, M. A.; Shaw, P. N.; Davies, M. C. Resistance to Nonspecific Protein Adsorption by Poly(vinyl alcohol) Thin Films Adsorbed to a Poly(styrene) Support Matrix Studied Using Surface Plasmon Resonance. *Anal. Chem.* **2001**, *73 (21)*, 5232– 5239.

57. Serizawa, T.; Hashiguchi, S.; Akashi, M. Stepwise Assembly of Ultrathin Poly(vinyl alcohol) Films on a Gold Substrate by Repetitive Adsorption/Drying Processes. *Langmuir* **1999**, *15 (16)*, 5363– 5368.

58. De Witt, J. A. and van de Ven, T. G. M. Kinetics and Reversibility of the Adsorption of Poly(vinyl alcohol) onto Polystyrene Latex Particles. *Langmuir* **1992**, *8 (3)*, 788-793.

59. Santhiya, D.; Subramanian, S.; Natarajan, K. A.; Malghan, S. G. Surface Chemical Studies on the Competitive Adsorption of Poly(acrylic acid) and Poly(vinyl alcohol) onto Alumina. *J. Colloid Interface Sci.* **1999**, *216 (1)*, 143–153.

60. Sperling, L. H. *Introduction to Physical Polymer Science*, 4th ed.; John Wiley & Sons, Inc., 2006.

61. Bornside, D. E.; Macosko, C. W.; Scriven, L. E. On the Modeling of Spin Coating. *J. Imaging Technol.* **1987**, *13 (4)*, 122– 130.

62. Meyerhofer, D. Characteristics of Resist Films Produced by Spinning. *J. Appl. Phys.* **1978**, *49 (7)*, 3993– 3997.

63. Qi, Y.; Nguyen, H.; Lim, K. S. E.; Wang, W.; Chen, W. Adsorptive Spin Coating to Study Thin-Film Stability in Both Wetting and Nonwetting Regimes. *Langmuir* **2019**, *35 (21)*, 6922– 6928.

64. Bieniek, M. K.; Llopis-Hernandez, V.; Douglas, K.; Salmerón-Sánchez, M.; Lorenz, C. D. Minor Chemistry Changes Alter Surface Hydration to Control Fibronectin Adsorption and Assembly into Nanofibrils. *Adv. Theory Simul.* **2019**, *2 (12)*, 1900169.

65. Bathawab, F.; Bennett, M.; Cantini, M.; Reboud, J.; Dalby, M. J.; Salmerón-Sánchez, M. Lateral Chain Length in Polyalkyl Acrylates Determines the Mobility of Fibronectin at the Cell/Material Interface. *Langmuir* **2016**, *32 (3)*, 800–809.